



# ScuDo

Scuola di Dottorato ~ Doctoral School  
WHAT YOU ARE, TAKES YOU FAR



Doctoral Dissertation  
Doctoral Program in Mechanical Engineering (34<sup>th</sup> Cycle)

# Experimental and Numerical Investigation of Contact Stiffness in Blade Root Joints

**Hadi Dastani**

\* \* \* \* \*

## Supervisors

Prof. Daniele Botto

## Doctoral Examination Committee:

Prof. Muhammad UMER , Referee,  
Institute of Space Technology Islamabad

Prof. Francesco CAPUTO , Referee,  
University of Campania Luigi  
Vanvitelli

Politecnico di Torino  
June, 2022

The text of this thesis may be reproduced for non-commercial purposes, provided that credit is given to the original author.

I hereby declare that, the contents and organization of this dissertation constitute my own original work and does not compromise in any way the rights of third parties, including those relating to the security of personal data.

Hadi Dastani  
Turin, June , 2022

# Summary

Interfaces or “joints”, which are unavoidable in design and development of mechanical equipment, play a significant role in the behavior of the whole assembly. To some extent, the effect of the interfaces can be studied introducing the two contact parameters known as “contact stiffness” and “equivalent damping”.

The normal contact stiffness (acting along the interface normal) and the tangential contact stiffness (acting on the interface plane) behave nonlinearly and depend on the condition of the contact surfaces. Moreover, if the contact surfaces undergo a relative displacement the interface dissipates the energy of friction. This energy dissipation results in additional damping of the structure. From a mechanical point of view joints affect i) the static behavior of the assembly, ii) the dynamic behavior and iii) the local stress at the interfaces.

Joints affect the static behavior of the whole structure in terms of displacements and static strength. Furthermore, they change the dynamic behavior of the structure in terms of resonance frequency and peak amplitude. Uncertainties on the value of the contact parameters make the dynamic performance of the structure less predictable than desired.

This thesis focuses on the contact characteristics of the blade root joints subjected to the dry friction damping under periodic excitation. The numerical method and experimental procedure are combined to trace the contact behavior in the nonlinear vibration conditions. In the experimental procedure, a novel excitation method alongside the accurate measurements is used to determine the frequencies of the blade under different axial loads. In numerical simulations, the local behavior of contact areas is investigated using the reduction method as a reliable and fast solver. Subsequently, by using both experimental measurements and numerical outcomes in a developed code, the global stiffness matrix is calculated. This leads to finding the normal and tangential stiffness in the contact areas of a dovetail blade root joints. The results indicate that the proposed method can provide an accurate quantitative assessment for the investigation of the dynamic response of the joints by focusing on the contact areas.

# Acknowledgment

To begin, I would like to express my gratitude to my advisor Prof. Daniele Botto for his continue support to my PhD activity. His guidance helped me to overcome the obstacles that I found in my research path and his passion for his job is a source of inspiration for me. In these three years I learned a lot from him, both in professional and in human fields and I hope to put this into practice in my life.

Secondly, I wish to thank all the kind members of LAQ AerMech Laboratory for the pleasant working environment and the time spent together. The opportunity to work with them on an extremely interesting topics put a light in my future journey. In particular I am thankful to Prof. Christian Maria Firrone that have supported me in the PhD endeavors. Thanks to them, I have the foundations to face the world of work.

Naturally, a particular thank goes to my parents who gave me the opportunity to study and support with their valuable advice. Finally, a great thank goes to my lovely wife Naeme who lights up my days with her presence, and our little angel, Elena who always gives us strong motivation throughout life.

*I would like to  
dedicate this thesis to  
my dear family,  
my lovely wife,  
Naeme  
and my sweet  
daughter,  
Elena*

# Contents

1. Introduction.....	12
1.1 Introduction to Contact Mechanics.....	12
1.2 General background of blade contacts.....	13
1.3 Contact Models.....	16
1.3.1 Effective parameters.....	17
1.3.2 Elastic continuum theory.....	18
1.4 Numerical simulation methods.....	19
1.5 Experimental validations.....	19
1.5.1 Micro-scale measurements.....	19
1.5.2 Macro-scale measurements.....	20
1.6 Thesis objectives and outline.....	20
1.6.1 Thesis Structure.....	21
1.6.1.1 Dynamic tests.....	21
1.6.1.2 Numerical Simulations.....	21
1.6.1.3 Theoretical estimate of stiffness values $k_n$ , $k_t$ .....	22
2. Dynamic tests.....	23
2.1 Test rig.....	23
2.1.1 Support and traction structure of the sample.....	26
2.1.2 Dynamic excitation system.....	26
2.1.3 Input signal.....	26
2.1.4 Shaker.....	27
2.1.5 Laser pointer for vibration speed measurement.....	28
2.1.6 Traction Force Measurement System.....	28
2.2 Operating procedure.....	29
2.2.1 Free Vibration Response Test.....	29
3. Experimental Analysis.....	31

3.1	Signal Analysis.....	31
3.1.1	Extraction of the free decay $v(t)$ signal.....	31
3.2	Identification of modal parameters.....	32
3.2.1	FREEVIB method.....	33
3.3	Modelling of the code with 1 D.O.F model.....	36
3.3.1	Sliding contact pattern.....	37
3.3.2	Method of temporal integration.....	37
3.3.3	State Contact and the relevant contact force.....	38
3.4	Comparison between the theoretical modal parameters and FREEVIB method.....	39
3.5	Analysis of the measurements.....	42
3.5.1	First Flexural Mode.....	42
3.5.1.1	Effect of vibration amplitude on frequency and damping... ..	42
3.5.1.2	Effect of traction force on frequency and damping.....	44
3.5.2	Second Flexural Mode.....	46
3.5.2.1	Effect of vibration amplitude on frequency and damping... ..	47
3.5.2.2	Effect of traction force on frequency and damping.....	48
3.6	Estimation of errors.....	50
4.	Numerical Simulations.....	52
4.1.	The general procedure of simulation with Finite Elements.....	52
4.2.	Finite Element Model.....	53
4.3	Stiffening effect of the axial load.....	54
4.3.1	Stiffening effect on beam.....	56
4.3.2	Stiffening effect on Slots.....	57
4.4	CMS reduction of the model.....	57
4.4.1	Choice of Master Nodes.....	59
4.5	Resonance frequency dependence on the tensile load.....	60
5.	Contact Stiffness Model.....	64
5.1.	Definition of assembly matrices.....	64
5.1.1	Constraints on the supports.....	65
5.1.2	Connectivity matrix.....	67
5.1.3	Contact Element.....	68
5.1.4	Stiffness matrix in global coordinates.....	68
5.2	Search of the $k_n$ and $k_t$ .....	70
5.2.1	Nonlinearity behavior of the system.....	71

5.2.2	Determination of $(k_n, k_t)$ for each axial force.....	72
5.2.3	Error propagation of measurements.....	73
5.3	Estimation of error of $k_n, k_t$ and search for the solution with minimum error.....	74
5.4	Search results for $k_n, k_t$ .....	77
6.	Theoretical estimate of contact stiffness.....	80
6.1	Contact Model.....	81
6.2	2D pressure and shear traction distributions.....	83
6.3	Tangential stiffness.....	86
6.4	Normal Stiffness.....	87
6.5	Comparison of the Stiffness values obtained with the theoretical ones.....	88
7.	Conclusions.....	91
7.1	Possible further developments.....	92
	Appendix A.....	93
	Appendix B.....	95
	Appendix C.....	100
	Appendix D.....	102
	Appendix E.....	105
	Appendix F.....	108



# List of Tables

Table 2.1: Modification of Material Characteristics.....	30
Table 2.2: Comparison of Natural frequencies .....	30
Table 3.1: First Flexural Mode: Error estimate - contact Status: STICK.....	51
Table 3.2: Second Flexural Way: Error estimate - contact Status: STICK.....	51
Table 4.1: Checking the elastic supports.....	55
Table 4.2: Stiffening effect of axial force on the beam.....	56
Table 4.3: Frequency variations considering all nodes fixed in normal direction.	61
Table 4.4: Frequency variations considering all nodes of contact surfaces are fixed in both normal and tangential directions.....	62
Table 5.1: Error of the measured frequencies interpolated for the F.E. forces..	74
Table 5.2: Final results of the search for $k_n$ , $k_t$ .....	77

# List of Figures

1.1	Common types of friction joints.....	14
1.2	Possible energy balance between the energy introduced by aerodynamics.....	14
1.3	Dovetail joint under examination, boundary conditions.....	15
1.4	Example of a hysteresis loop of the tangential contact force.....	16
1.5	$k_{eq}$ and $c_{eq}$ of a 1 D.O.F. system, SHBM method.....	17
1.6	Lumped Parameter Contact Models.....	17
1.7	Flowchart of the thesis.....	22
2.1	The blade with dovetail shape at the end subjected to contact areas.....	24
2.2	Test bench configuration.....	25
2.3	Diagram of the Test Bench.....	25
2.4	Test machine including the supports and traction structure.....	26
2.5	Input signal for the shaker.....	27
2.6	Shaker detail of its tip.....	27
2.7	A laser pointer and speed measurement points.....	28
2.8	Strain measurement system.....	29
2.9	Dovetail dummy blade on free-free conditions, accelerator attached.....	29
2.10	Natural frequencies in three modes.....	30
3.1	Example of $v(t)$ signal obtained from the test bench.....	32
3.2	Example of a signal restricted to the free decay range.....	32
3.3	Example of the envelope, natural frequency, and damping.....	35
3.4	Example of nonlinear dependence $f_n(A)$ and $\eta(A)$ obtained with the FREEVIB method.....	35
3.5	Model 1 D.O.F. with sliding contact for FREEVIB validation.....	37
3.6	Predictor-Corrector scheme.....	39
3.7	1 D.O.F. Model, Direct integration.....	40
3.8	Application of the FREEVIB method to the 1 DOF model.....	41
3.9	Equivalent stiffness and damping provided by the SHBM.....	41
3.10	Measurement point for First Flexural Mode.....	42
3.11	First Flexural Mode: Damping as a function of amplitude.....	43
3.12	Frequency as a function of Amplitude Effect of traction force on frequency and damping for first flexural mode.....	44
3.13:	Effect of the tensile force on $f_n$ and $\eta$ under adhesion conditions.....	45
3.14:	Natural frequency as a function of vibration amplitude and traction.....	45
3.15:	Damping as a function of the vibration amplitude and traction.....	46
3.16:	Second Flexural Mode measurement point.....	46
3.17:	Second Flexural: Frequency = $f_n(\text{Amplitude})$ , damping = $\eta(\text{Amplitude})$ for different values of effective ARMS current sent to the shaker.....	48
3.18:	Effect of the tensile force on $f_n$ and $\eta$ under adhesion conditions.....	49
3.19:	Frequency as a function of the amplitude of vibration and traction.....	49
3.20:	Damping as a function of vibration amplitude and traction.....	50
4.1:	Dovetail joint under examination.....	52
4.2:	F.E. model of the blade simulacrum and slots.....	53
4.3:	Nodes at the contact interface.....	53
4.4:	Load system for static analysis.....	54

4.5: Constraints by elastic supports on specific nodes for static analysis.....	55
4.6: Stiffening effect of axial force on the beam.....	56
4.7: Load and constraints on slots to investigate the stiffening effect.....	57
4.8: Negligible stiffening effect on slots.....	57
4.9: Master nodes for the reduced model.....	59
4.10: All nodes fixed in normal direction.....	61
4.11: All nodes of contact surfaces are fixed in both normal and tangential directions.....	62
4.12: Resonance frequency dependence on tensile load, first bending mode.....	63
4.13: Resonance frequency dependence on tensile load, second bending mode.....	63
5.1: Assembly of the super element mass matrices.....	65
5.2: Assembly of the super element stiffness matrices.....	65
5.3: Target nodes at the base of the supports.....	66
5.4: Global mass matrix after adding the constraints.....	67
5.5: Global stiffness matrix after adding the constraints.....	67
5.6: Linear contact element.....	68
5.7: Rotation of the coordinates of the contact elements.....	69
5.8: Assembly of the contact elements.....	69
5.9: Selection of frequencies in complete adhesion status of the contacts.....	70
5.10: Selection of $f_{stick}$ , frequencies for $F_{ax} > 12kN$ .....	71
5.11: Example of nonlinear dependence of the frequency on $k_n$ , $k_t$ .....	72
5.12: Example of solution space (red circles) - ( $F_{ax} = 12kN$ ).....	74
5.13: Solution ( $k_n$ , $k_t$ ) with minimum error ( $F_{ax}=12kN$ ).....	76
5.14: Percentage errors of $k_n$ and $k_t$ .....	77
5.15: Normal stiffness variations considering the estimated errors.....	78
5.16: Tangential stiffness variations considering the estimated errors.....	78
5.17: Results of the frequency comparison for the first bending mode in stick contact status.....	79
5.18: Results of the frequency comparison for the first bending mode in stick contact status.....	79
6.1: Model of the indenter on the flat half-space.....	80
6.2. On the left real dovetail geometry, on the right load applied at 2D problem.....	81
6.3. Normal pressure distribution on 3D half plane.....	82
6.4. Pressure distribution, for different ratio between tangential force and normal force.....	84
6.5. Shear distribution for different ratio between tangential force and normal force.....	85
6.6: Contact geometry.....	86
6.7: Tangential Stiffness variations considering the Normal Force.....	87
6.8: Normal Stiffness variations considering the Normal Force.....	88
6.9: Normal Stiffness variation in two states $T=0$ and $T=\mu N$ .....	89
6.10: Tangential Stiffness variation in two states $T=0$ and $T=\mu N$ .....	89
6.11: Theoretical vs numerical-experimental comparison.....	90
6.12: Comparison of theoretical vs numerical-experimental $k_t$ .....	90

# Chapter 1

## Introduction

### 1.1 Introduction to Contact Mechanics

Contact problems are central to Solid Mechanics because contact is the principal method of applying loads to a deformable body and the resulting stress concentration is often the most critical point in the body. Contact at the blade-to-disk interface is a typical problem that can be studied using contact mechanics principles.

Contact is characterized by unilateral inequalities, describing the physical impossibility of tensile load tractions and material interpenetration. Furthermore, inequalities and non-linearity are introduced when friction laws are taken into account. Historically the work of Hertz might be thought of as the birth of the study of elastic contact and it still provides a better benchmark for different numerical methods.

In general two different kinds of contact can result, depending on the geometry of contacting bodies. First, when two convex bodies are pressed together contact is initially made at a point (or line in the case of plane problems), and as the applied load is increased the contact path grows. Such contacts are said incomplete, for example, the contact of a sphere on a plane. They have the characteristic that the contact pressure falls to zero continuously at the edge of the contact. A further division of classification of incomplete contacts is possible: if the contact size is small in comparison with the deformed part of the body (and providing at the other

extreme that the contact is not too sharp) the bodies being loaded may be represented by half planes or spaces. This means that the formulation of the elasticity problems may be appropriate to a semi-infinite body, which greatly simplifies the calculation. Problems, where the size of the contact patch is small in comparison with the bodies' surface radius of curvature, and which therefore permit the half-plane approximation to be used, are said to be non-conformal.

The second kind of contact occurs when the size of the contact is independent of the contact force. In this case, the contact pressure distribution is singular at the edge of the contact. Such contacts are said completely.

## **1.2 General background of blade contacts**

The mechanical design of the bladed rotors in aeronautical turbines needs particular attention to verifying the structural integrity for High Cycle Fatigue conditions. For this purpose, the components' behavior prediction due to vibration is an important step. This objective is achieved through numerical simulations, which require dynamic models as accurate as possible.

As the bladed rotors are made up of many components, they typically have a high-density modal which means many resonant frequencies close to each other. Furthermore, the variability of the operating conditions of aircraft engines implies a broad spectrum of excitation dynamics due to aerodynamic forces. Such aspects make a dynamic behavior infeasible in which all possible resonance conditions are avoided. For this reason, it is necessary to control the vibration amplitude through the present damping in the system. The primary damping sources can be summarized as the material's damping, aerodynamic damping, and friction in the contact interfaces. The latter provides the main contribution of energy dissipation. As it is accessible to realize, it is the most frequent passive damping method of vibration amplitudes in aeronautical turbines.

Usually, the dynamic of the bladed disk is considered linear, so the structure interaction is directly linked to the natural frequencies and normal mode shapes of the system. However, structural designers of aircraft engines have introduced nonlinearities in the bladed disk structure in terms of joints that act also as damping systems to reduce peak stress values during the vibratory phenomenon caused by the external excitation forces. These damping systems are usually jointed geometrically optimized to produce friction forces to dissipate energy increasing the strength and life of the blade against High Cycle Fatigue failure.

The major sources of friction damping (Figure 1.1) in the bladed disk turbine are attributable to the contact between adjacent blades connected by interference at the tip (shrouds - Figure 1.1a), mid-span airfoil (snubber – Figure 1.1b), under platform dampers (Figure 1.1c) and the bladed disk interfaces (blade root joint - Figure 1.1d). The last joint is practically always included in the bladed disk design while the other types of joint may not be present.

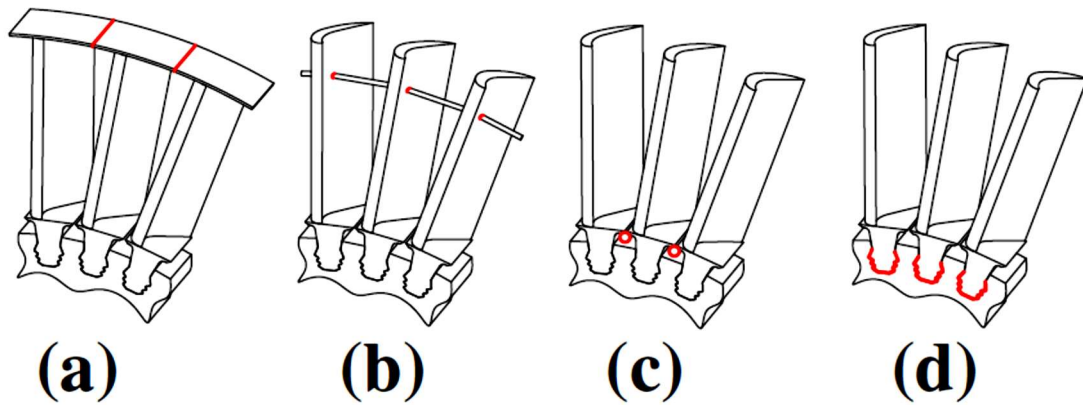


Figure 1.1: Common types of friction joints: (a) shrouds, (b) snubber, (c) under platform damper and (d) root joints

As these friction contacts limit the vibrations due to the excitation forces, they can be used to suppress the unstable flutter vibrations to produce a periodic motion called Limit Cycle Oscillations (LCO). In this condition, the amplitude and the frequency of the LCO are determined by the equilibrium between the energy introduced in the system by the flow (blue dashed curve) and the energy dissipated by the friction contacts (red solid curve) as shown in Figure 1.2.

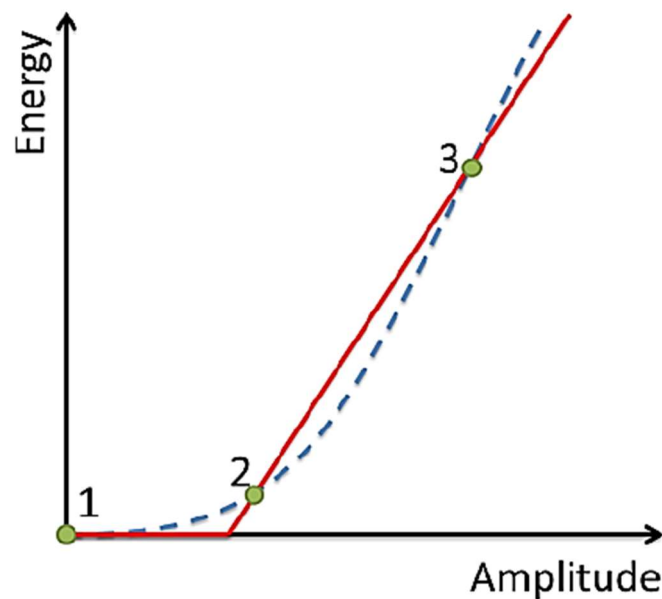


Figure 1.2: Possible energy balance between the energy introduced by aerodynamics (blue dashed curve) and dissipative energy by friction (red solid curve)

The balance between the aerodynamic and dissipated energies provides in general three solutions: the solution 1 is the trivial solution where there is no exchange of energy because there is no vibration; besides, this is an unstable solution because any small perturbation of the system moves the system away from 1 and towards solution 2. Solution 2 is the stable solution of the system and it will be called the LCO solution; in fact, any perturbation from 2 limited between solution

1 and solution 3 does not change the final equilibrium '2'. Solution 3 is unstable and represents the stable limit of the system because any perturbations bigger than this limit produce ineffective damped and uncontrolled self-excited vibrations.

An intrinsic problem with the Figure 1.1d type of damping lies in the nonlinear nature of the contact behavior, which makes numerical simulations complex and computationally expensive. The force exchanged in the interfaces cannot be linearly approximated since they are dependent on displacement, which is affected by the state of contact: complete adhesion, micro-slip, macro-slip, or separation. The contact condition also depends on materials, roughness and geometry of the contact, preload forces normal to surfaces, and vibration amplitudes. In the case of disc-blade joints, the boundary conditions are defined by the subjected centrifugal force and vibration amplitude caused by aerodynamic forces, as shown in Figure 1.3.

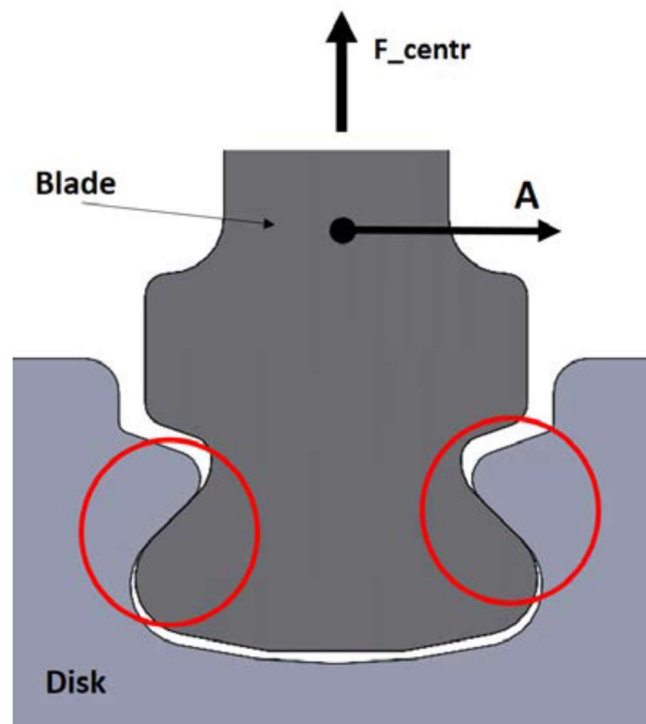


Figure 1.3: Dovetail joint under examination, boundary conditions

Commercial finite element codes allow the simulation of such nonlinearity only through the direct temporal integration of the equations of motion. This method takes time and very high computing costs. Therefore, a solution adopted by the industry is the use of linear dynamic models, with the complete and constant adhesion of the contact interfaces. In such models, damping is relative viscous of the order of  $\zeta = 2 \cdot 10^{-3}$  [1] to consider the material, aerodynamic and friction damping. This method implies errors in estimating stresses due to vibrations that are not always acceptable. The nonlinearity of contacts introduces variations in resonance frequencies and vibration amplitudes that are not negligible. Therefore, intense research was carried out to develop contact models and efficient solution methods for nonlinear equations of motion.

### 1.3 Contact Models

The contact models entail generating a model that predicts the contact behavior as a function of some input parameters. Here, a summary of different contact states is described as an introduction to the research.

The contacts have 3 possible states: micro-sliding (or “micro-slip”), macro-sliding (or "gross-slip") and separation (or "lift-off"). Complete adhesion of the contact is an extreme case of the micro-slip condition. In detail, the micro-slip is defined as the partial sliding of the regions at the edge of the contact. As normal preload decreases or the amplitude of tangential vibration increases, the sliding propagates within the contact region until the total sliding of the entire interface occurs, which means gross-slip. Fully stuck is also a very important state which can be included in the contact models, however in this study, the model focus on the other states to investigate the stiffness.

During vibrations, the saturation effect of the tangential force due to sliding, which refers to Coulomb's law  $T \leq \mu N_0$ , causes the states alternation of micro-slip and gross-slip.  $T$  represents shear force,  $\mu$  is the friction coefficient and  $N_0$  is the contact pressure between surfaces. The law states that for two dry solid surfaces sliding against one another, the magnitude of the kinetic friction exerted through the surface is independent of the magnitude of the velocity (i.e., the speed) of the slipping of the surfaces against each other. It forms a hysteresis loop between the tangential contact force and relative displacement of interface surfaces. An example of a hysteresis loop of the tangential contact force ( $T$ ) is shown in Figure 1.3 in which  $k_t$  is the tangential stiffness,  $x_0$  is the relative displacement of interface surfaces and  $x_{cr}$  is relative displacement when sliding occurs.

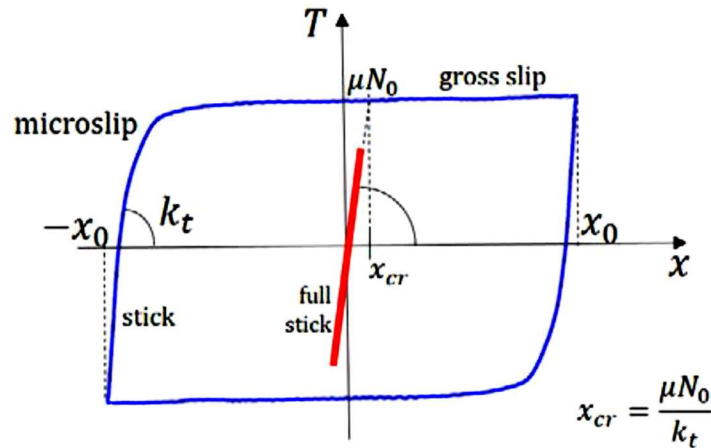


Figure 1.3: Example of a hysteresis loop of the tangential contact force

From the hysteresis cycle, an equivalent stiffness and damping can be extracted. The stiffness  $k_{eq}$  is interpreted as the overall slope of the cycle. At the same time, the damping  $c_{eq}$  is associated with the energy dissipated by the non-conservative friction force, which concerns the area of the cycle. These are shown in Figure 1.4. These parameters depend on the vibration amplitude  $A$ , preload  $N_0$ , material, and contact geometry.



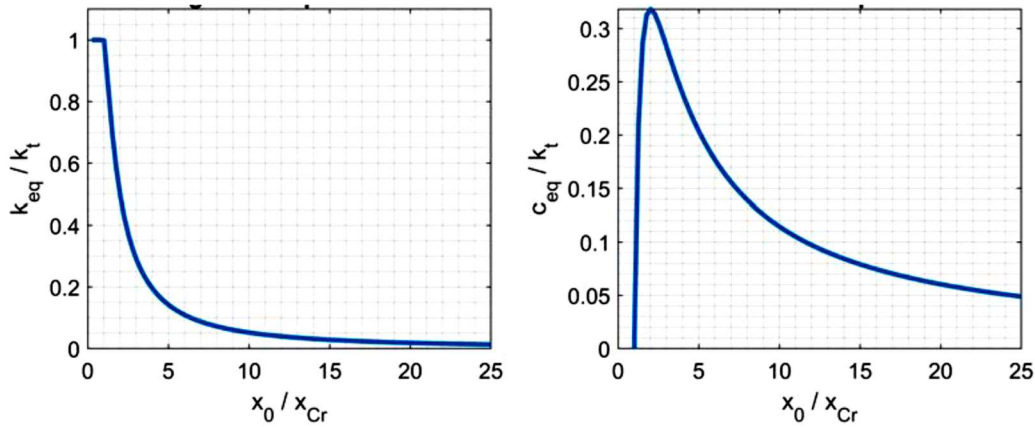


Figure 1.4:  $k_{eq}$  and  $c_{eq}$  of a 1 D.O.F. system, SHBM method [2]

### 1.3.1 Effective parameters

Many lumped-parameter models have been developed for point-to-point contacts in finite element simulation codes [2-7].

Griffin [2] proposed a 1D tangential relative displacement model and preload normal constant  $N_0$ , as shown in Figure 1.5.  $T$  is the tangential force,  $\mu$  refers to friction coefficient and  $w$  is the displacement.

$$T = \begin{cases} k_t(x - w) & \text{stick: } |T| < \mu N_0, \dot{w} = 0 \\ \mu N_0 \text{sgn}(\dot{w}) & \text{slip: } |T| = \mu N_0, \dot{w} \neq 0 \end{cases}$$

Yang et al. [3] have extended the 1D model to the case of normal variable preload. Schwingshackl and Petrov [4] later adopted a model to develop the elements contact. Stanbridge and Ewins [5] and Menq and Yang [6] defined a model with normal preload constant and relative two-dimensional tangential displacement. Yang and Menq [7] studied the 2D model with normal variable preload.

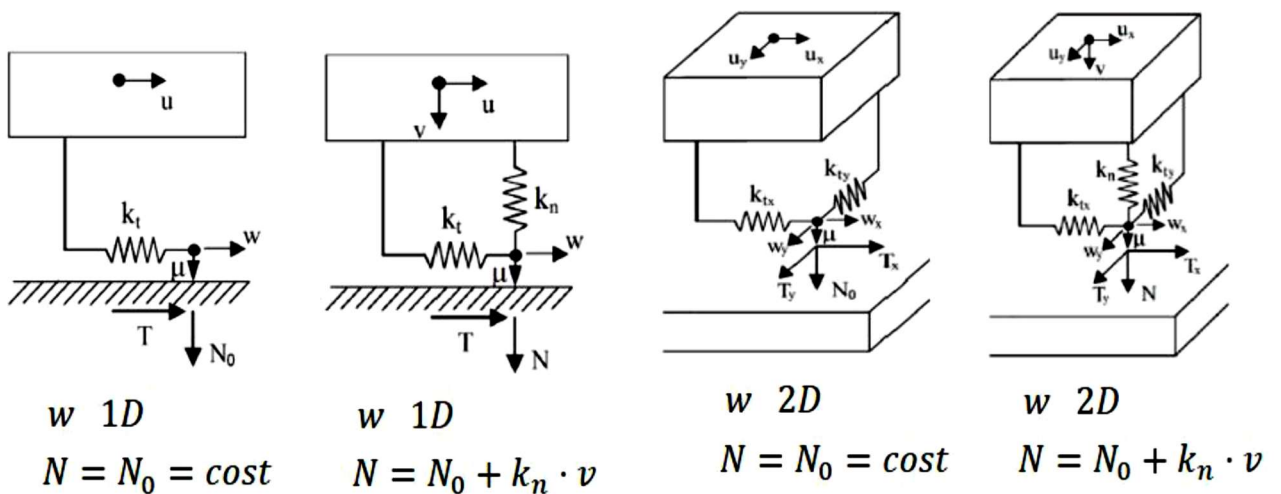


Figure 1.5: Lumped Parameter Contact Models [7]

Three parameters must be defined to use these models: friction coefficient  $\mu$ , normal stiffness  $k_n$ , and tangential stiffness  $k_t$ . Many experimental activities have

been carried out for the characterization of these parameters. However, the infeasibility of a complete experimental description due to the extreme variability in materials, operating conditions (such as loads and temperatures), and contact geometries have conducted research towards developing analytical models for the definition of such parameters.

### 1.3.2 Elastic continuum theory

The developed analytical models are based on continuous mechanics principles of contact. Sliding contacts between spherical surfaces were studied by Mindlin et al. in [8], where analytical expressions of the hysteresis cycle for this type of contact have been found. The sliding contacts between compliant surfaces were examined by Lavella et al. [9] by using a test bench. He developed the hysteresis cycles, the friction coefficient and the tangential stiffness of contact by varying normal load and excitation frequency. In terms of vibrations of bladed discs, Mindlin's theory has been applied in [10], [11] to predict the behavior of platform dampers with spherical contacts. Shtayerman [12] analyzed two-dimensional contact between conformal surfaces - typical of disc-blade joints – and obtained the contact behavior results in a flat indenter with rounded edges, pressed onto a flat half-space as shown in Figure 1.6.

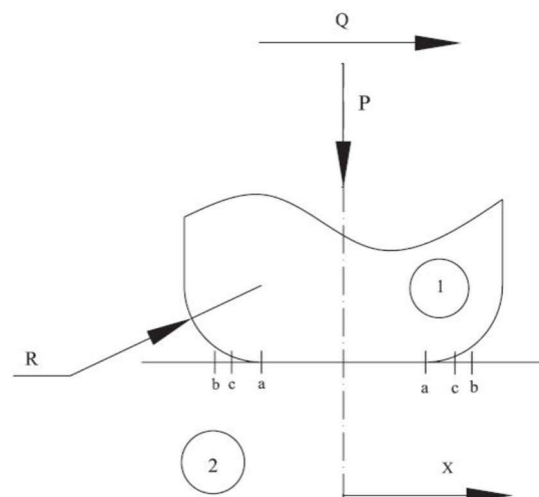


Figure 1.6: Model of the flat indenter pressed on the flat half-space [13]

Ciavarella [14] used these results to extend the discussion of two-dimensional contact behavior. In [1], Allara applied the theory of three-dimensional Boussinesq-Cerruti of pressure and shear distributions to obtain the displacements of this model. He proposed a method for defining the hysteresis loop for this type of contact and explained a numerical-analytical procedure for calculating contact parameters.

## 1.4 Numerical simulation methods

The contact models mentioned above are used in computational codes specially developed to solve nonlinear equations of motion with more efficient time integration methods in commercial software.

To compute the forced response in the frequency domain, a widely adopted technique is Harmonic Balance Method (HBM) proposed by Cardona et al. [15] and applied in [15]-[21]. It is one of the most popular methods to find periodic steady-state responses of nonlinear differential equations. The standard HBM as a popular method, approximates the periodic solution in the frequency domain. Local nonlinearities cannot be evaluated directly in the frequency domain. The standard HBM performs an inverse Fourier transformation and then calculates the nonlinear force in the time domain and the Fourier coefficients of the nonlinear force. Zucca et al. [19, 20] have subsequently demonstrated the simultaneous calculation of static components is possible dynamic of contact forces. To calculate the non-periodic responses, such as free decay and transients in general, Gastaldi [22] proposed temporal integration techniques. In this research, nonlinearities of contact are obtained through the temporal sequence of linear systems, i.e., by approximating the nonlinear system of equations with a piecewise linear system.

## 1.5 Experimental validations

The need to validate such solution methods, contact models, and theoretical estimates of parameters pushed the research towards two experimental procedures. In dynamic micro-scale tests, the local behavior of contacts is studied by measuring forces and displacements. Therefore, the contact parameters, including stiffness  $k_{eq}$  and damping  $c_{eq}$  equivalent, can be obtained from the hysteresis cycle.

In the dynamic macro-scale tests, the global behavior of the bodies is analyzed. It is done by measuring forced response in the frequency domain or free decay in the time domain as the boundary conditions vary compared with those obtained from numerical simulations.

### 1.5.1 Micro-scale measurements

Mindlin et al. [23] first analyzed sliding contacts between spherical surfaces and measured convex surfaces' hysteresis loops. Johnson [24] measured the hysteresis static and dynamic of steel balls pressed on flat surfaces. Goodman and Brown [25] examined steel spheres oscillating between two parallel planes in compression. Filippi et al. have measured the friction coefficient, hysteresis cycles, the tangential contact stiffness at room temperature [26], and high temperature for spherical surfaces in contact with flat surfaces [27]. The sliding contacts between compliant surfaces were examined by Botto et al. [9]. They created a test bench capable of ensuring flat contact despite the wear of surfaces and measured the hysteresis cycles, friction coefficient, and the tangential stiffness of contact for various normal load and excitation frequencies. Ewins et al. in [16] and [21] measured the friction coefficient and tangential stiffness for a plane contact for different materials and load conditions.

## 1.5.2 Macro-scale measurements

Goodman and Klumpp conducted the first experimental analyses of contacts sliding effect on global dynamic behavior in turbine rotors [28]. They measured the hysteresis cycles for disc-blade joints subjected to a uniform compression load. In this study, the importance of friction damping and its dependence on normal load has been well demonstrated.

In [1], Allara has designed a test bench to study the behavior of disc blade joints dovetail as the centrifugal load, and the vibration amplitude vary. In such work, a beam with dovetail joints was fixed. It was subjected to traction and vibration with electromagnetic exciters while the response measured during the free decay of oscillations. The obtained signals were analyzed with suitable methods to derive the frequency and damping of the nonlinear system as a function of load and vibration amplitude.

The same test bench of [1] was used in [13] to measure the forced response in the frequency domain. It was necessary to validate the codes based on the Harmonic Balance Method.

Dynamic tests similar to those presented in [1] were carried out in [29]. In [30] the behavior of a cantilever beam fixed at one end with a disc-blade joint. Screws provide a preload normal to contact. The system is placed on an oscillating platform.

Various joint geometries are tested. In [31] the same method is applied to palettes to study the distribution of tension and notch effect in the blade attachments. In [32], the global dynamic behavior of a vane is measured at the same time in contact with under-platform dampers and the local behavior of contacts to relate the performance curves of these dampers (macro-scale) with the contact characteristics  $k_{eq}$ ,  $c_{eq}$  (micro-scale).

## 1.6 Thesis objectives and outline

The work presented in this thesis has been developed in an industrial context that is represented by GE Avio Aero. In particular, it aimed at developing a method for the calculation of the non-linear aeroelastic behavior of a bladed disk in the presence of friction contacts at a blade root joint.

The present work belongs to the macro-scale category of experimental validations through measurements of dynamic responses of a dovetail type of blade root joints. As referred in previous studies, the importance of friction damping and its dependence on normal load has been demonstrated, however the effect of amplitude and validation of numerical method didn't considered [30]. Furthermore the novelty of the present works is developing a contact model which is confirmed by both experimental and numerical methods. To put in a nutshell, the main objectives of this thesis are described below:

1. Deepen understanding of the dynamic performance of a specific type of joint by measuring the frequency and damping of a blade simulacrum as a function of centrifugal force and vibration amplitude  $f_n = f_n (F_{centr}, A)$   $\eta = \eta (F_{centr}, A)$ ;
2. Provide a database of measurements during free decay oscillations to validate new methods of nonlinear temporal integration such as those proposed in [22];

3. Obtain normal and tangential contact stiffness from macroscopic measurements, which can be used in contact models of numerical simulations and validate the theoretical estimates of these parameters proposed in [13]

### 1.6.1 Thesis Structure

In this section, a general view of the thesis structure is presented to introduce the contents of the current research activity.

In Figure 1.7 the flowchart of the thesis is shown. It presents how the combination of dynamic tests which is the experimental section and numerical simulation leads to develop a contact model to identify the stiffness value in contact region. Then, the theoretical evaluation is also considered and the results are presented.

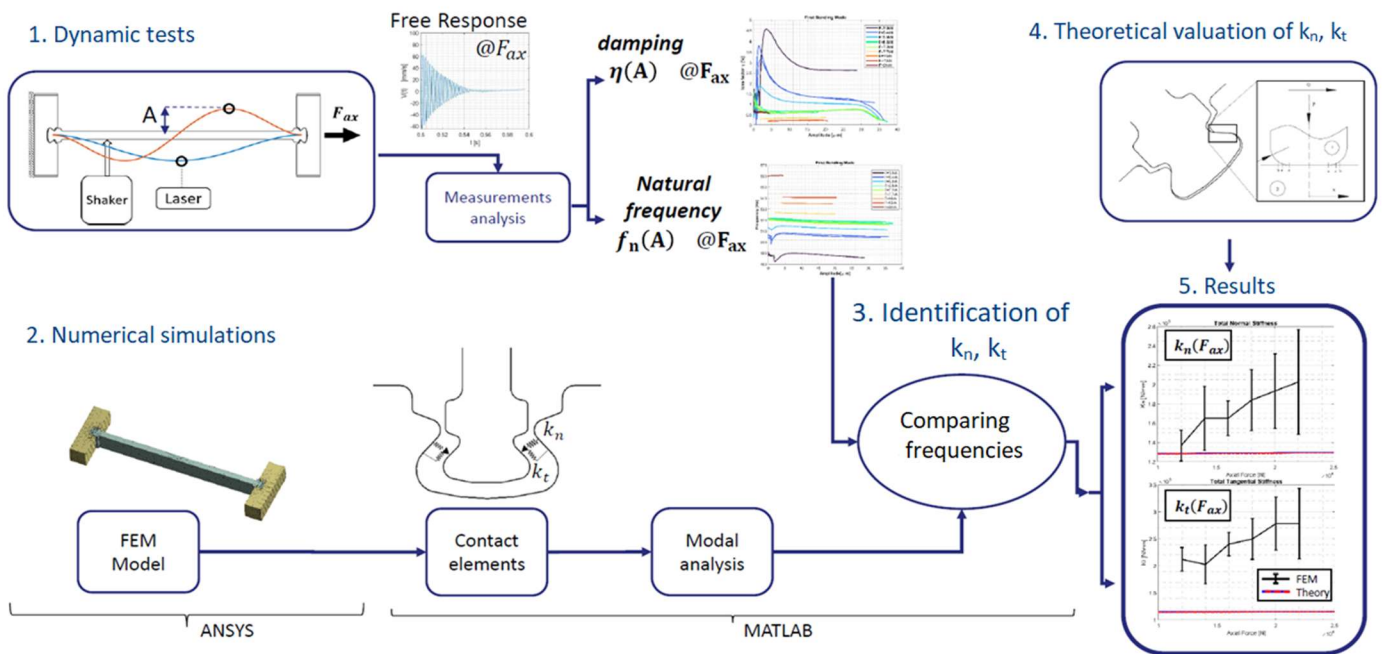


Figure 1.7: Flowchart of the thesis

#### 1.6.1.1 Dynamic tests

As the measurements on an actual bladed disk have many difficulties, Allara developed a simplified dynamic system to simulate the centrifugal force on the blade [1]. The test bench to carry out the experimental procedure in this research has been described in detail in his research work [1]. It includes a beam fixed at the ends with dovetail joints and subjected to traction force. Furthermore, an electro-mechanical exciter (shaker) is used to apply vibration on the blade and measure the velocities of some points using a laser device.

Two types of measurements were made to examine the first and second mode shapes of the blade. Each measurement provided the response of the blade during the free decay

oscillations. An oscillatory excitation with a frequency close to the natural frequencies of the blade has been applied. This response was obtained by measuring the speed  $v(t)$  of the antinode of the model in question. Each measurement was carried out for a given tensile force value. The free-response measurements were processed with the FREEVIB method proposed by Feldman in [33-34] to analyze nonlinear systems. The natural frequency and the damping (loss factor  $\eta$ ) in the function of vibration amplitude  $A$  have been measured.

### 1.6.1.2 Numerical Simulations

The following procedure was followed to find the stiffness values:

1. The model of blade and beam supports (slots) were discretized using the finite element method in ANSYS®, paying particular attention to the coincidence of nodes in the contact interfaces.
2. Nonlinear static analyzes were carried out in ANSYS® on the blade for different axial forces to obtain the stiffening effect of this force on the stiffness matrix of the simulacrum.
3. Model degrees of freedom were reduced in ANSYS® with component mode synthesis technique, presented by Craig-Bampton [35]. Then the mass and stiffness matrices of the reduced model were imported in the MATLAB®. The master nodes used for the reduction are related to contacts and further nodes necessary for displaying the modes.
4. The reduced models of beam and supports were assembled in MATLAB® by introducing linear contact elements, i.e., that do not implement sliding state or contact separation. The parameters of these elements are the stiffness values which is the object of the present research.
5. A MATLAB® code has been developed to search for stiffness values for each tensile force. Such code compares the frequencies of the first and second flexural modes of the Finite Element Method (FEM) model with the corresponding frequencies obtained from the analysis of measurements. This comparison is made in the range of axial forces of traction and amplitudes of vibration in which complete adhesion of the contacts was found (no micro slip), which implies the system's linearity.

### 1.6.1.3 Theoretical estimate of stiffness values $k_n$ , $k_t$

The contact stiffness  $k_n$ ,  $k_t$  were calculated using the theoretical model of indenter rounded edges pressed onto a flat surface, proposed in [13]. Then theoretical values were compared with those obtained from the numerical-experimental procedure.

In following chapters, the above mentioned are described in detail. In chapter 2, the experimental procedure and dynamic tests are discussed. It includes how the test rig works, excitation method using shaker, required measurements and operation procedure. In chapter 3, the experimental analysis is described which includes signal analysis using Freevib method, analysis of the measurements and estimation error. Numerical simulation is explained in chapter 4. Contact stiffness model which is developed using the combination of experimental and numerical investigation is described in chapter 5. Theoretical estimate of contact stiffness is described in chapter 6 and in chapter 7 described the conclusion.

# Chapter 2

## Dynamic tests

In this chapter the dynamic tests procedure is described in detail. The blade with dovetail joints and testing machine is introduced, then the dynamic excitation system and operation procedure is described.

### 2.1 Test rig

In order to study the dynamic behavior of the blade root joints, it is necessary to investigate the response by considering the variation of the centrifugal force and vibration amplitude. Due to the difficulties to measure the real bladed disk response, where spin is necessary to pull the blades, a simplified dynamic system was designed. The test bench has already been designed and used by Allara to investigate the damping effects of blade root joints [1]. The objectives of the system are:

- to vibrate a dynamic system similar to a blade that is fixed to its disk using dovetail joints with the same geometry as the actual joints;
- to recreate at the joint interfaces the same stress and strain fields that would be found on the real joint of a rotating bladed disk;
- to investigate the dynamic behavior under different vibration amplitudes and different pulling loads at the joint, with loads equal to the centrifugal forces that would be pulling the blade for different rotational speeds of the disks;
- to avoid the introduction of any other source of damping other than material damping, viscous damping due to the atmosphere, and the damping due to the joint under investigation.

In [1], the idea of simulating a centrifugal force on a pallet through a loading system is excluded, as it may introduce additional damping. The solution implemented in this study is to analyze the dynamic behavior of a beam supported by dovetail shape joints at both ends and pulled at one end, as shown in Figure 2.1. Furthermore, a novel excitation method using a shaker is introduced in this research study.

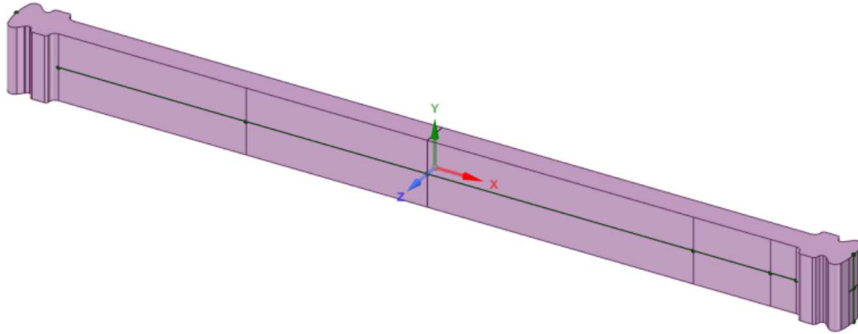


Figure 2.1: The blade with dovetail shape at the end subjected to contact areas

The main differences between the dynamic behavior of an actual blade and the body under examination are as below:

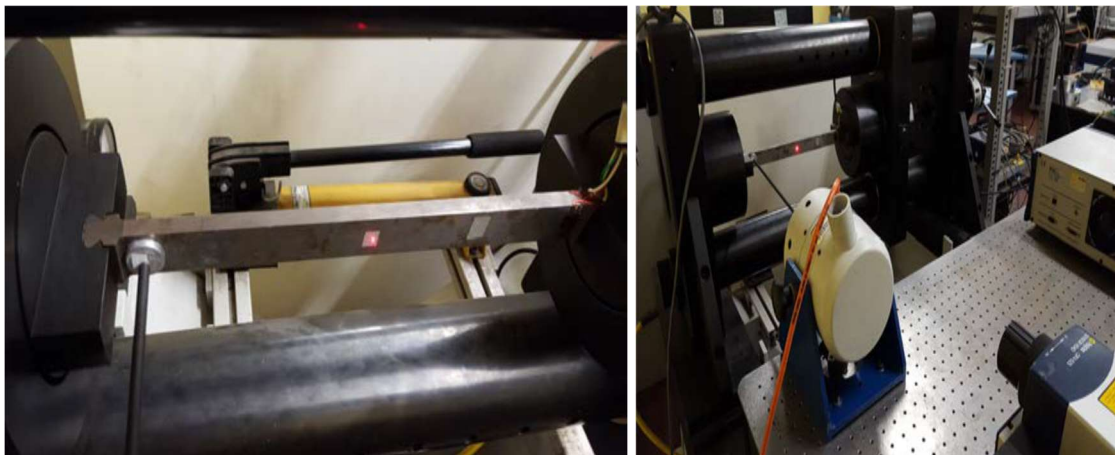
- a real blade has one joint and its modal shapes are approximately like those of a cantilever beam, while the simplified system under test here is similar to a fixed-fixed beam.
- the cross-section of the body is rectangular (26mm×10mm) and constant along the entire axis of the beam, unlike an actual blade
- the centrifugal force on the actual blade is maximum at the root and decreases towards the tip while the body under examination has constant normal stress along the longitudinal axis. However, as the energy dissipated by joints depends on the force on the cross-section in the vicinity of the joint itself, the beam of this test bench dissipates the same energy as the same force acting on the blade attachment

The test bench consists of five subsystems, as shown in Figure 2.2, including:

1. The support and traction system of the beam designed in [1], as Figures 2.2a, 2.2b. This system has two crosspieces, one of which is fixed - solid to support (dovetail type). The other is mobile, solid to keep the other end of the beam. The latter crossbar is connected to a hydraulic actuator that allows traction of the beam.
2. Dynamic excitation system, consisting of a signal generator, a signal amplifier, and electrodynamic exciter (shaker), as shown in Figure 2.2b.
3. The vibration speed measurement system consists of a laser interferometer and its control tool, as shown in Figure 2.2b.
4. Traction force measurement system, consisting of two independent subsystems to double-check the measurements. The first subsystem includes a pressure gauge that provides pressure inside the hydraulic actuator. The second subsystem consists of strain gauges placed on the beam and their data acquisition system, indicated with H.B.M. in the diagram of Figure 2.3.



5. Data collection and acquisition system, consisting of BNC cables, to carry the signals speed and deformation analogs from the BNC connection block and the data acquisition located inside the NI PXIe 1073 Chassis.



(a) Beam and supports

(b) Shaker, Laser, Support structure

Figure 2.2: Test bench configuration

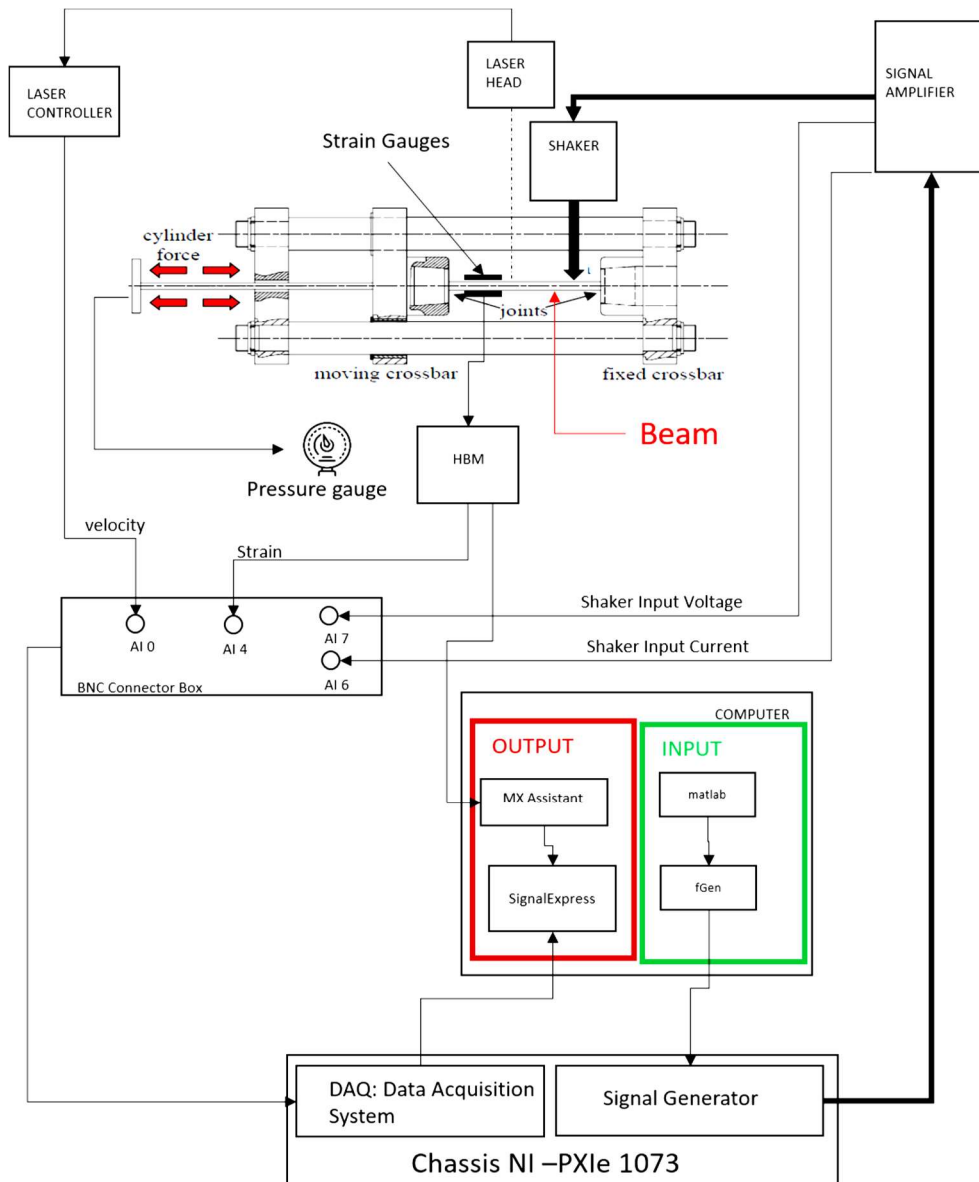


Figure 2.3: Diagram of the Test Bench

### 2.1.1 Support and traction structure of the sample

The operating scheme of the support structure, designed in [1], is similar to the machine for the tensile testing of specimens. The beam (Figure. 2.4 (a)) has dovetail-type ends which simulate bladed disk turbine rotors attachments.

Supports are integral with the crosspieces (b) and (c). The crosspiece (c) is fixed, while (b) is movable along the longitudinal axis of the beam. This last crosspiece is connected to a hydraulic actuator (e) and a manual screw actuator operated by the lever (d). The hydraulic actuator (e) provides the traction load, and a valve (h) allows the retention of this load for the whole duration of the test. The pressure is managed by the hand pump (f) and can be viewed in the pressure gauge (g). At the end of the test, it is necessary to open the valve (h) to cancel the difference pressure inside the actuator (e).

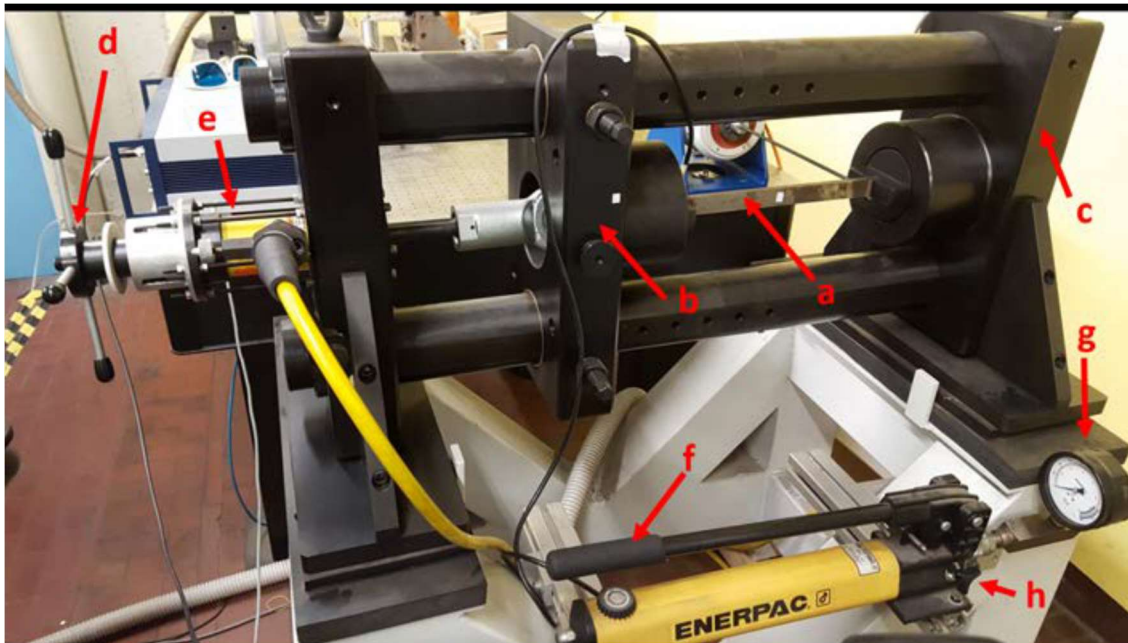


Figure 2.4: Test machine including the supports and traction structure

### 2.1.2 Dynamic excitation system

The dynamic excitation on the blade is achieved through the TIRA electrodynamic shaker S514. It is controlled in current through the TIRA BAA amplifier 500, which amplifies the signal coming from the NI-PXI 5412 signal generator, managed by a developed "fGen" software, which allows the import of a generic input signal in text format.

### 2.1.3 Input signal

In the present work, the free decay response of the beam associated with specific modes is investigated. For this purpose, the input Sin signal shown in Figure 2.5 is created using a MATLAB® code.

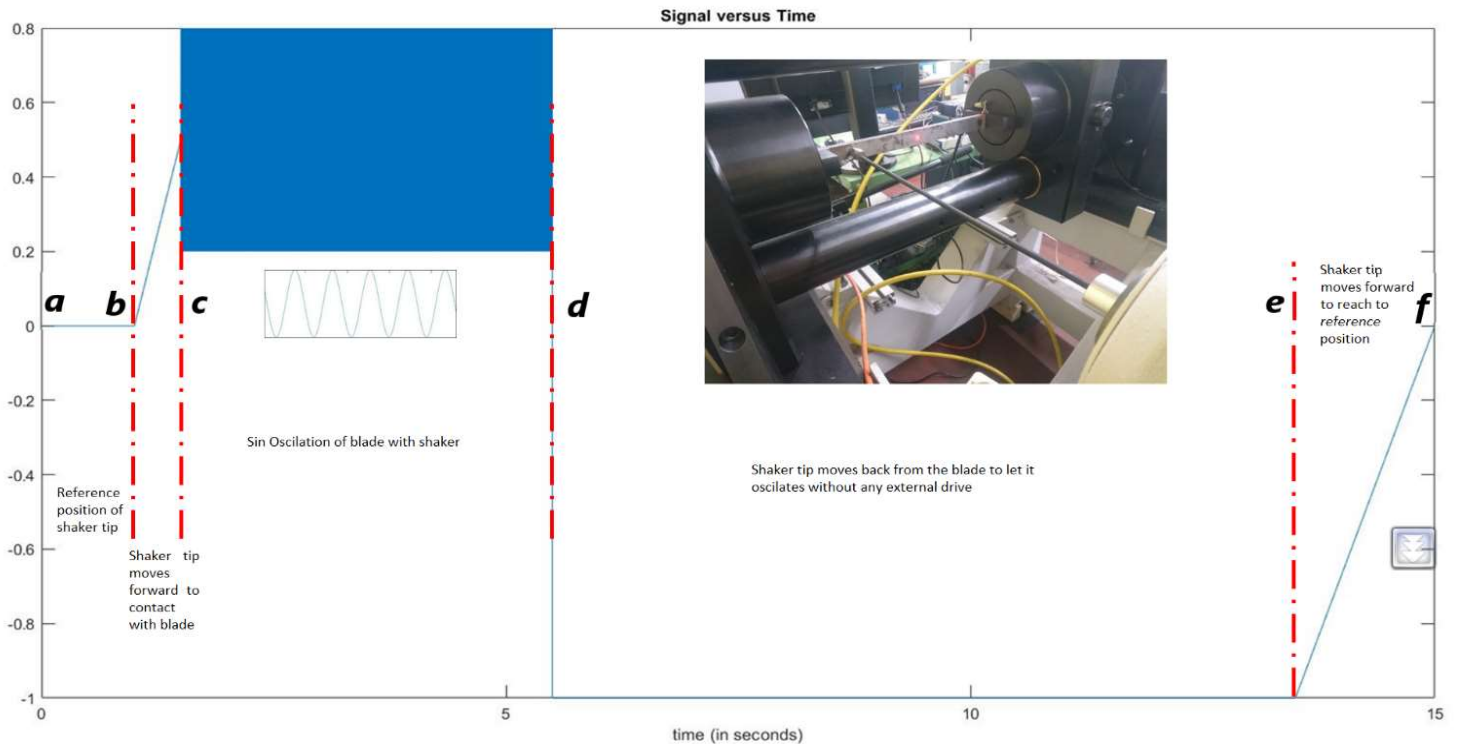


Figure 2.5: Input signal for the shaker

The input signal in Figure 2.5 refers to the shaker tip position at every moment. To investigate the free-response, the blade should be excited with frequencies close to the modal ones (c-d), then detach the shaker tip instantly from the oscillatory blade (d). It is necessary to provide an initial static preload (a-b) greater than the vibration amplitude to avoid detachment of the tip during the excitation,

The response measurement of the beam during the free decay vibrations was carried out in the time interval in which the stinger was detached entirely from the beam. In the final step (e-f), the tip of the shaker is returned to the initial position.

### 2.1.4 Shaker

The shaker has been rigidly fixed by screws to a technical bench. The tip of the shaker was placed on aluminum support integral with the beam, on which it was made a non-passing conical notch for housing the tip, necessary to avoid the tangential sliding during the excitation phase of the blade simulacrum. It is shown in Figure 2.6.

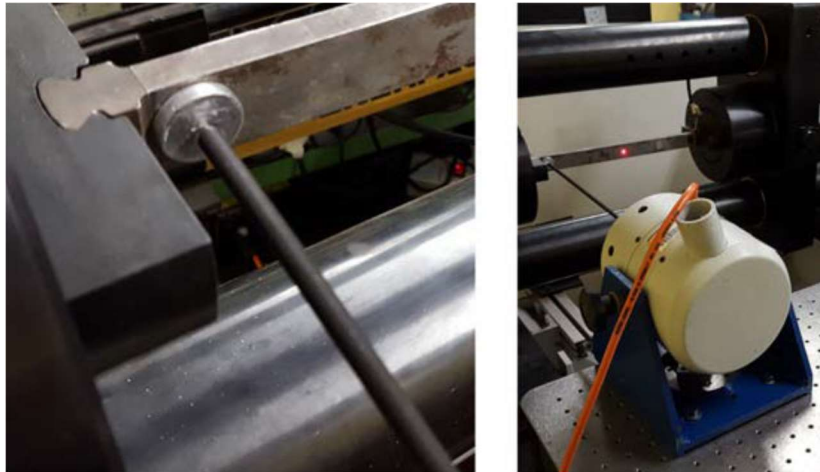


Figure 2.6: Shaker detail of its tip

### 2.1.5 Laser pointer for vibration speed measurement

As shown in Figure 2.7, the Polytec OFV-525 laser interferometer was used to measure the vibration speed of specific points on the beam. In detail, the laser is set to the points that are expected to have the first and second bending modes.

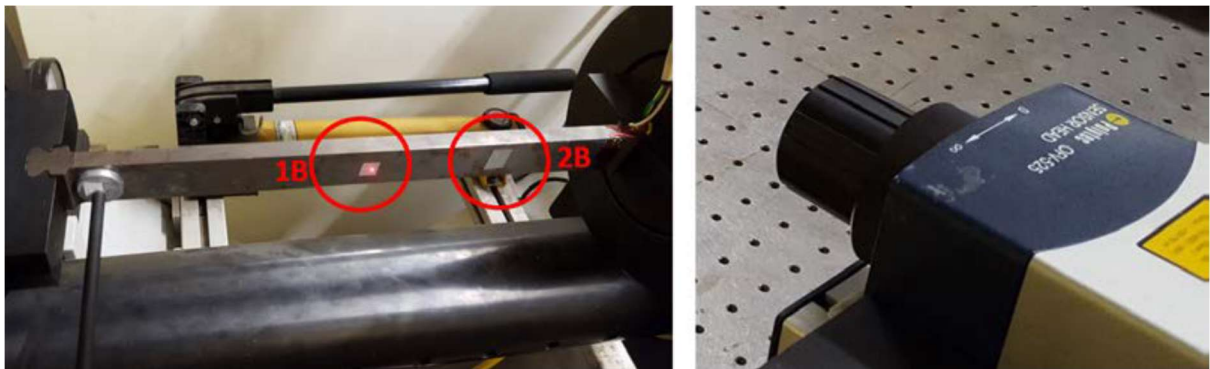


Figure 2.7: A laser pointer and speed measurement points

### 2.1.6 Traction Force Measurement System

The traction force was measured by two independent subsystems as described below.

#### Pressure gauge

The first subsystem consists of the Enerpac GP-10S pressure gauge, visible in Figure 2.4(g). It provides the pressure difference inside the hydraulic actuator. Using the effective piston area from the technical specifications, the pulling force is calculated as below:

$$F = A_{cyl} \cdot P \quad \text{where } A_{cyl} = 17.9 \text{mm}^2$$

The instrument's accuracy is equal to  $\delta p p = 1\%$  at full scale 700 bar pressure.

#### Strain gauges

The second subsystem consists of Wheatstone bridge strain gauges according to the Figure 2.8(a) for measuring the axial deformation of the beam.

$$F = A \cdot \sigma = A \cdot E\varepsilon$$
$$A = 26\text{mm} \times 10\text{mm}$$
$$E = 210\text{GPa (SAE1040 steel)}$$

The adopted instrumentation is shown in Figure 2.8(b) as below.

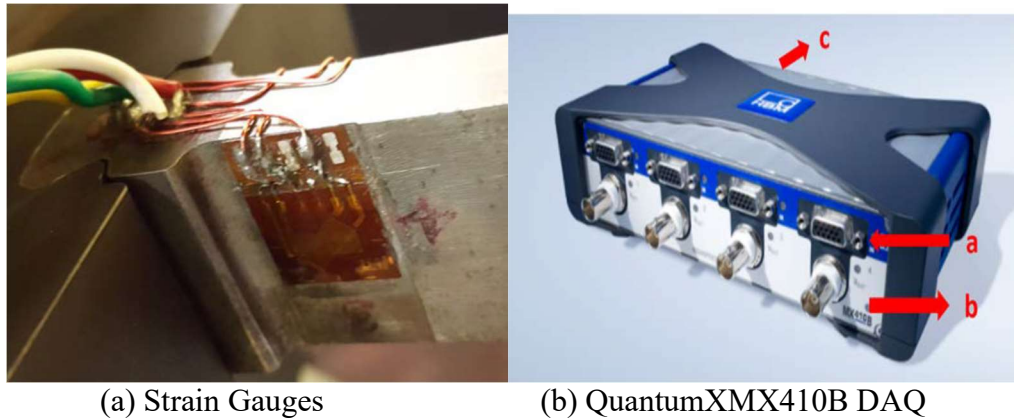


Figure 2.8: Strain measurement system

## 2.2 Operating procedure

Two groups of measurements, including first and second bending modes, were made. Each measurement provided the free response of the blade with a frequency close to that of the modal form under analysis. Furthermore, the measurements were carried out for a given tensile force value, used as a parameter of the present experiment.

### 2.2.1 Free Vibration Response Test

In the other part of the experimental activities the natural frequency measurement was investigated to adjust the numerical and experimental parameters and investigations close to each other as much as possible.

Many techniques can be used to identify and/or confirm a high vibration level caused by a resonance frequency. Impact test: one of the most commonly used methods for measuring a system's natural frequency is to strike it with a mass and measure the response. This method is effective because the impact inputs a small amount of force in the equipment over a large frequency range.

To this purpose, the free-free condition for the dovetail dummy blade including an attached accelerometer was considered. The selected point should be far from the nodes of different mode shapes. This is shown in Figure 2.9



Figure 2.9: Dovetail dummy blade on free-free conditions, accelerator attached

The modulus of elasticity and the density according to the real weight and volume of blade should be also modified. Table 2.1 shows the modified values that are considered for further numerical investigations.

Table 2.1: Modification of Material Characteristics

Material Characteristics	Primary consideration	Modified values for Numerical analysis
Modulus of Elasticity(N/m <sup>2</sup> )	200e9	200.3 e9
Density(kg/m <sup>2</sup> )	7850	7592

The numerical method was also used to obtain the natural frequencies in free-free conditions. The mode shapes are shown in Figure 2.10.

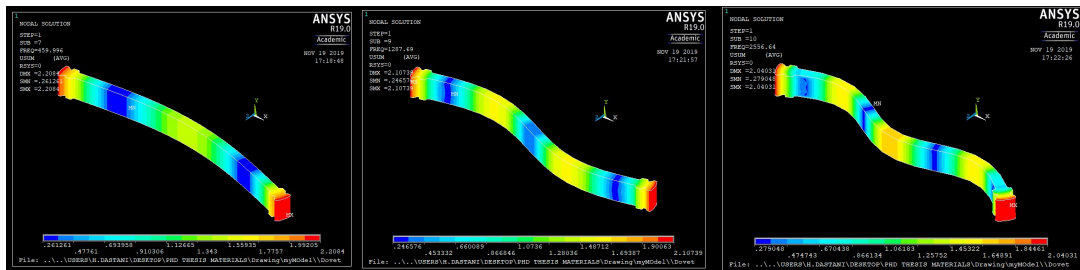


Figure 2.10: Natural frequencies in three modes

Natural frequencies obtained from both numerical and experimental procedures are shown in table 2.2.

Table 2.2: Comparison of Natural frequencies

Natural frequencies Dovetail, Free/free conditions				
Experimental		460	1286	2539
Numerical	Coarse mesh	459.9	1287.7	2556.6
	Refine mesh	459.3	1281.8	2527

# Chapter 3

## Experimental Analysis

In this chapter the experimental analysis is described using the experimental measurements. In the first step signal analysis procedure is introduced, then the modal parameters are identified. Then analysis of the measurements is described for the first and second bending modes.

Identification of damping of nonlinear structures with small damping is rather difficult, both for experimental techniques and identification methods. All practical engineering structures most likely have non-linear behavior to some extent, which is caused by one or several factors.

The first step of dynamic experimental analysis was to utilize simple procedure to establish if the tested system was linear or not and if the degree of linearity depended on two parameters: excitation level and centrifugal force, as expected. In these preliminary tests only a qualitatively estimation of nonlinear damping is possible. Methods employed are based on the fact that many of the properties which hold for linear system or structures break down for nonlinear.

### 3.1 Signal Analysis

The speed signal  $v(t)$  for different values of the axial loads has been measured for the first and second flexural modes during the experimental procedure. Using these data, the dependency of natural frequency and damping to the axial load and vibration amplitude can be investigated, i.e.,  $f_n = f_n(A, F_{ax})$   $\eta = \eta(A, F_{ax})$

### 3.1.1 Extraction of the free decay $v(t)$ signal

The first step is selecting the proper range of data which obtained during the experiment. As mentioned, the excitation procedure includes different stages. It is necessary to focus on the start point of detachment of the shaker tip from the vibration blade for free decay vibration. An example of a velocity signal obtained from the test bench is shown in Figure 3.1.

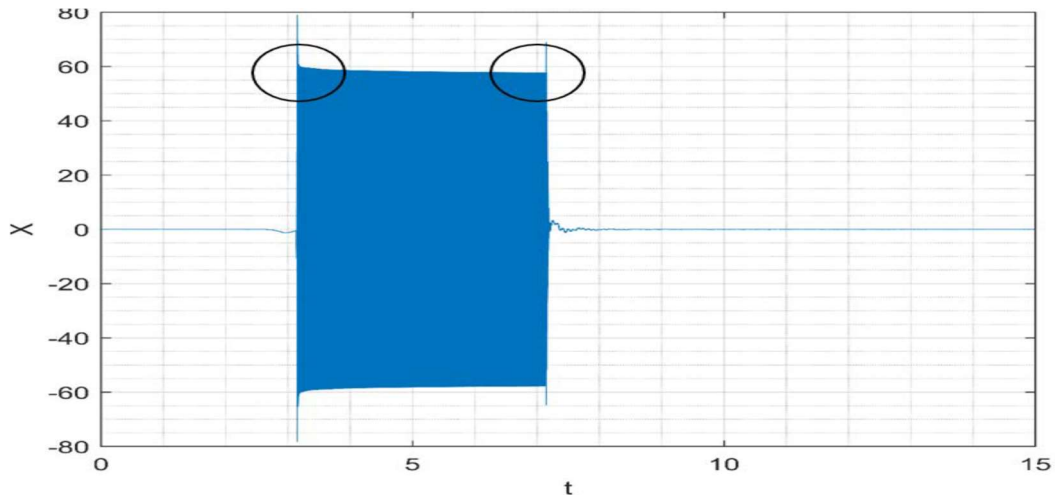


Figure 3.1: Example of  $v(t)$  signal obtained from the test bench

Therefore, to get the proper range for further analysis, the recorded data in the time frame after the instant detachment of the shaker tip to 1/1000 of the initial envelope's width is selected. An example of such selection criteria is shown in Figure 3.2.

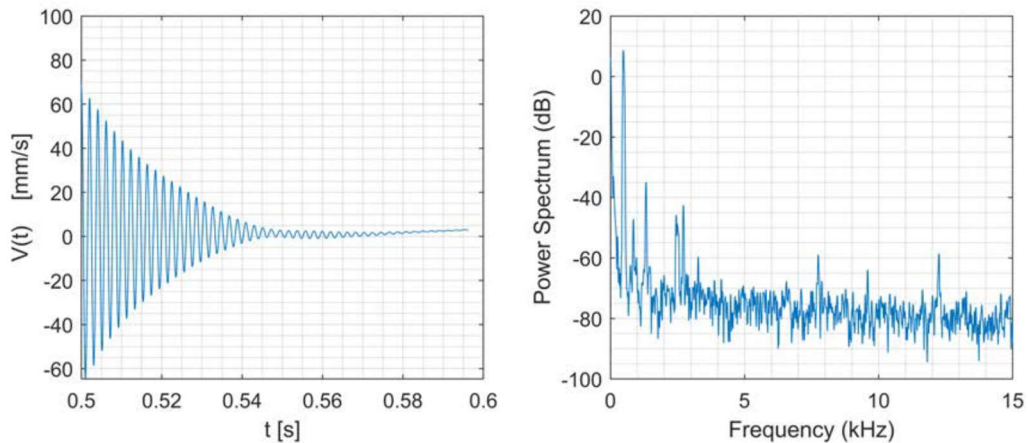


Figure 3.2: Example of a signal restricted to the free decay range

## 3.2 Identification of modal parameters

This section used the theory of analytical signals and the Hilbert transform to identify the nonlinear dependence of the natural frequency,  $f_n$ , and damping,  $\eta$ , on the vibration amplitude. The method that was followed is the "FREEVIB" proposed by Feldman in [3] for nonlinear systems [3] and applied to linear systems in [4]. This method effectively identifies nonlinearities in the stiffness and damping characteristics of a vibration system.



The method is based on input and output time-domain measurements, and their Hilbert transforms. It defines the instantaneous modal parameters of a system under a slow or a very fast swept frequency test. The Hilbert Transform approach is suitable for any vibration system and does not require prior knowledge of the signal or of the system parameters. Such nonparametric identification will determine the amplitude and frequency dependencies and the initial nonlinear restoring and damping forces. This method was also used in the research work of Allara, Filippi, and Gola [1].

### 3.2.1 FREEVIB method

According to analytical signal theory a real signal  $y(t)$  can be represented as:

$$Y(t) = y(t) + i\tilde{y}(t) = A(t) \cdot e^{-i\varphi(t)} \quad \text{with} \quad A^2 = y^2 + \tilde{y}^2 \quad \tan\phi = \frac{\tilde{y}}{y} \quad (3.1)$$

where  $\tilde{y}(t)$  is the Hilbert transform of the original signal:

$$\tilde{y}(t) = H[y(t)] = \frac{1}{\pi t} \times y(t) = \frac{1}{\pi} \int_{-\infty}^{+\infty} \frac{y(\tau)}{t-\tau} d\tau \quad (3.2)$$

and  $A(t)$ ,  $\varphi(t)$  are respectively instantaneous Amplitude (or "Envelope") and instantaneous Phase, functions at real time values. The main sources of damping of the blade simulacrum are structural damping and friction damping in the dovetail joint. Both types of damping can be assumed independent of frequency, as stated in [1] for friction damping and in [5] for structural damping. The hysteretic damping model presented by Kelvin [5], was then used to represent the damping:

$$m\ddot{y} = -d \cdot H[y(t)] + k \cdot y(t) = 0 \quad (3.3)$$

Multiplying (3.3) by  $i$  and applying the Hilbert transform  $H[.] = \tilde{\cdot}$  to both sides:

$$\{i \cdot m\ddot{\tilde{y}} + i \cdot d \cdot y + i \cdot k \cdot \tilde{y} = 0 \quad (3.4)$$

By using the transform properties:

$$H[H[y]] = -yH\left[\frac{dy}{dt}\right] = \frac{dH[y]}{dt} \quad (3.5)$$

Then, by adding the two equations, we obtain:

$$m(\ddot{y} + i\ddot{\tilde{y}}) + id(y + i\tilde{y}) + k(y + i\tilde{y}) = 0 \quad (3.6)$$

Or

$$m\ddot{Y} + idY + kY = 0$$

Defining

$$\omega_n^2 = \frac{k}{m} \quad \eta = \frac{d}{k} \text{ Loss Factor}$$

the equation becomes:

$$\ddot{Y} + \omega_n^2(1 + i\eta)Y = 0 \quad (3.7)$$

Once the model is defined, the analytical signal is derived as described in [3]:

$$\begin{aligned}
 Y &= y(t) + i\tilde{y}(t) = A(t) \cdot e^{i\varphi(t)} \\
 \dot{Y} &= \frac{d(A(t) \cdot e^{i\varphi(t)})}{dt} = \dot{A} e^{i\varphi} + iA\dot{\varphi} e^{i\varphi} = Y\left[\frac{\dot{A}}{A} + i\dot{\varphi}\right] \\
 \ddot{Y} &= Y\left[\frac{\ddot{A}}{A} - \omega^2 + i2\omega\frac{\dot{A}}{A} + i\dot{\omega}\right]
 \end{aligned} \tag{3.8}$$

Substituting  $\frac{\ddot{Y}}{Y}$  in the equation (3.8) of the model and dividing by Y:

$$\frac{\ddot{A}}{A} - \omega^2 + i2\omega\frac{\dot{A}}{A} + i\dot{\omega} + \omega_n^2(1 + i\eta) = 0 \tag{3.9}$$

Thus, two equations are obtained, one for the real part and the other for the imaginary part, as below:

$$\begin{cases} \frac{\ddot{A}}{A} - \omega^2 + \omega_n^2 = 0 \\ 2\omega\frac{\dot{A}}{A} + \dot{\omega} + \omega_n^2\eta = 0 \end{cases} \tag{3.10}$$

So the frequency and damping can be obtained as below:

$$\begin{cases} \omega_n^2 = \omega^2 - \frac{\ddot{A}}{A} \\ \eta = -\frac{1}{\omega_n^2} (2\omega\frac{\dot{A}}{A} + \dot{\omega}) \end{cases} \tag{3.11}$$

All the parameters on the second side of the above equation are the values related to the signal that depends on time. The vibration amplitude of the free decay is also a one-to-one function of time  $A = A(t)$ . So, the nonlinear relationship of modal parameters, which depends on time, can be graphically determined. An example is shown in Figure 3.3 and Figure 3.4.

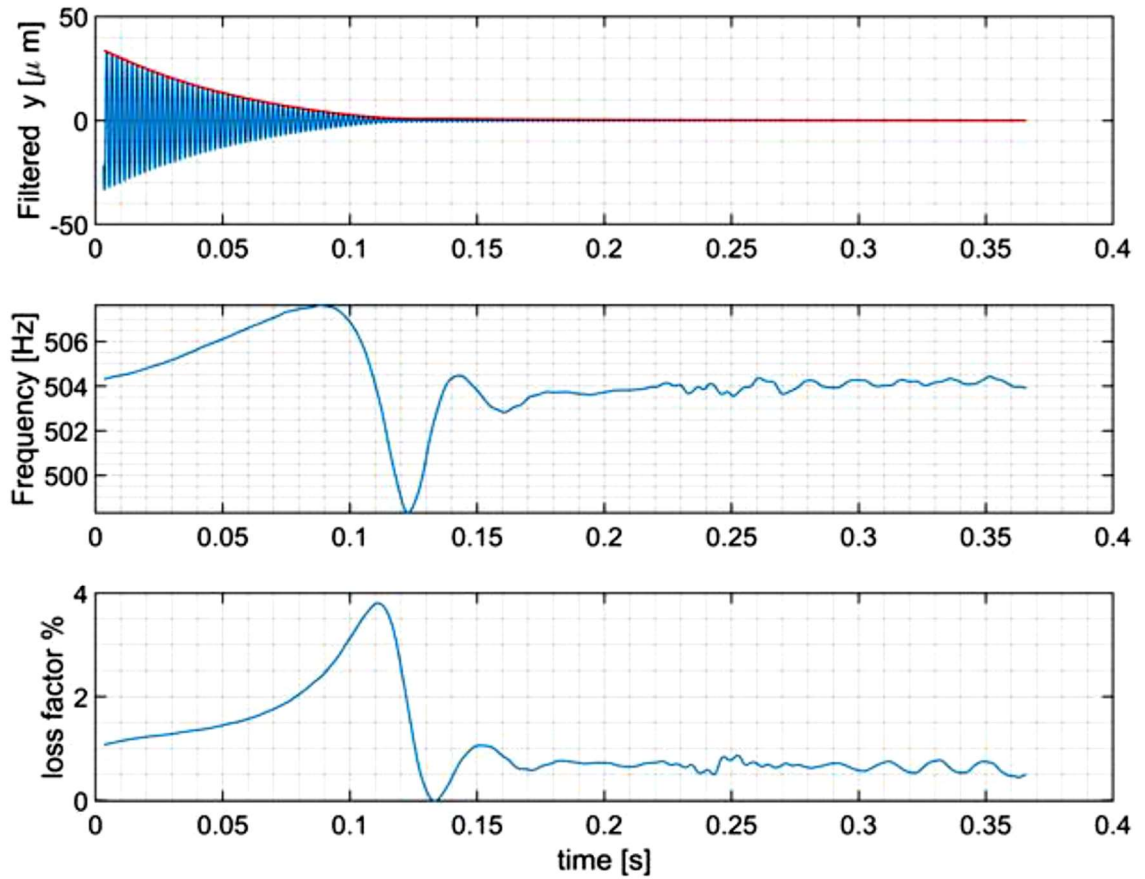


Figure 3.3: Example of the envelope, natural frequency, and damping in case of P=30bar

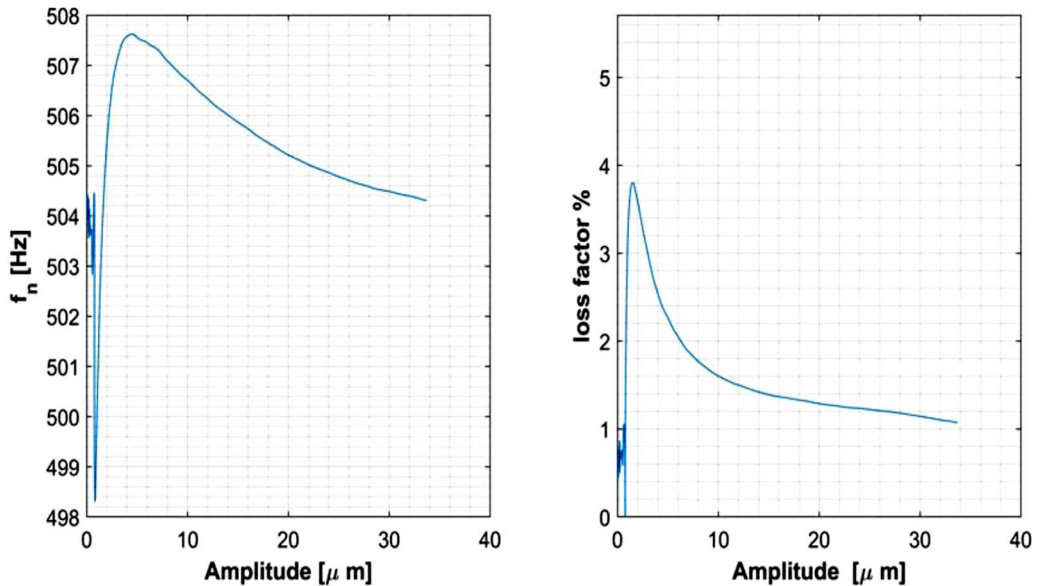


Figure 3.4: Example of nonlinear dependence  $f_n(A)$  and  $\eta(A)$  obtained with the FREEVIB method

To obtain the second side quantities of the equation (3.11) which the parameters depends modal, the expressions can be written as a function of

$$y, \dot{y}, \ddot{y} \quad \tilde{y}, \dot{\tilde{y}}, \ddot{\tilde{y}}$$

from the equations (3.10)

$$\dot{Y} = \dot{y} + i\dot{\tilde{y}} = Y \left[ \frac{\dot{A}}{A} + i\omega \right] = (y + i\tilde{y}) \left[ \frac{\dot{A}}{A} + i\omega \right] = \left( \frac{\dot{A}}{A} y - \omega \tilde{y} \right) + \left( \frac{\dot{A}}{A} \tilde{y} + \omega y \right)$$

From which

$$\begin{cases} \dot{y} = (-\tilde{y})\omega + (y)\frac{\dot{A}}{A} \\ \dot{\tilde{y}} = (+y)\omega + (\tilde{y})\frac{\dot{A}}{A} \end{cases} \Rightarrow \boxed{\begin{cases} \omega(t) = \frac{1}{A^2} (+y\dot{\tilde{y}} - \dot{y}\tilde{y}) \\ \frac{\dot{A}}{A}(t) = \frac{1}{A^2} (+y\dot{y} + \tilde{y}\dot{\tilde{y}}) \end{cases}} \quad (3.12)$$

and similarly by the third equation (3.10)

$$\begin{aligned} \ddot{Y} = \ddot{y} + i\ddot{\tilde{y}} &= Y \left[ \frac{\ddot{A}}{A} - \omega^2 + i2\omega\frac{\dot{A}}{A} + i\dot{\omega} \right] = (y + i\tilde{y}) \left[ \frac{\ddot{A}}{A} - \omega^2 + i2\omega\frac{\dot{A}}{A} + i\dot{\omega} \right] = \\ &= \left[ y \left( \frac{\ddot{A}}{A} - \omega^2 \right) - \tilde{y} \left( 2\omega\frac{\dot{A}}{A} + \dot{\omega} \right) \right] + i \left[ \tilde{y} \left( \frac{\ddot{A}}{A} - \omega^2 \right) + y \left( 2\omega\frac{\dot{A}}{A} + \dot{\omega} \right) \right] \end{aligned}$$

From which

$$\begin{cases} \ddot{y} = \left( -y\omega^2 - \tilde{y}2\omega\frac{\dot{A}}{A} \right) + (y)\frac{\ddot{A}}{A} + (-\tilde{y})\dot{\omega} \\ \ddot{\tilde{y}} = \left( -\tilde{y}\omega^2 + y2\omega\frac{\dot{A}}{A} \right) + (\tilde{y})\frac{\ddot{A}}{A} + (+y)\dot{\omega} \end{cases} \Rightarrow \boxed{\begin{cases} \dot{\omega}(t) = \frac{y\ddot{\tilde{y}} - \tilde{y}\ddot{y}}{A^2} - 2\omega\frac{\dot{A}}{A} \\ \frac{\ddot{A}}{A}(t) = \frac{y\ddot{y} + \tilde{y}\ddot{\tilde{y}}}{A^2} + \omega^2 \end{cases}} \quad (3.13)$$

In the case in question, the speed  $v(t) = \dot{y}$  is known, while the displacement  $y$  and the acceleration  $\ddot{y}$  are obtained by integration and numerical differentiation. The signals  $\tilde{y}$ ,  $\dot{\tilde{y}}$ ,  $\ddot{\tilde{y}}$  are obtained by applying the Hilbert numerical transform to  $y$ ,  $\dot{y}$ ,  $\ddot{y}$ , respectively.

The codes that used to apply the Hilbert transform, differentiate, and integrate the signals provided in [2,3] by Feldman himself, author of the FREEVIB method. In detail, the differentiation and Hilbert transformation are implemented via Parks-McClellan filters applied within a zero-phase filtering procedure. The integration is implemented with the trapezoids method, and any constant component is subtracted from the result, extracted with a medium filter.

### 3.3 Modelling of the code with 1 D.O.F. model

The nonlinearity behavior of this research case is due to the friction in contacts between the blade root and the support slots. For this reason, as shown in Figure 3.5, a simple model with one degree of freedom has been chosen with the same type of nonlinearity to validate the code that implements the FREEVIB method.

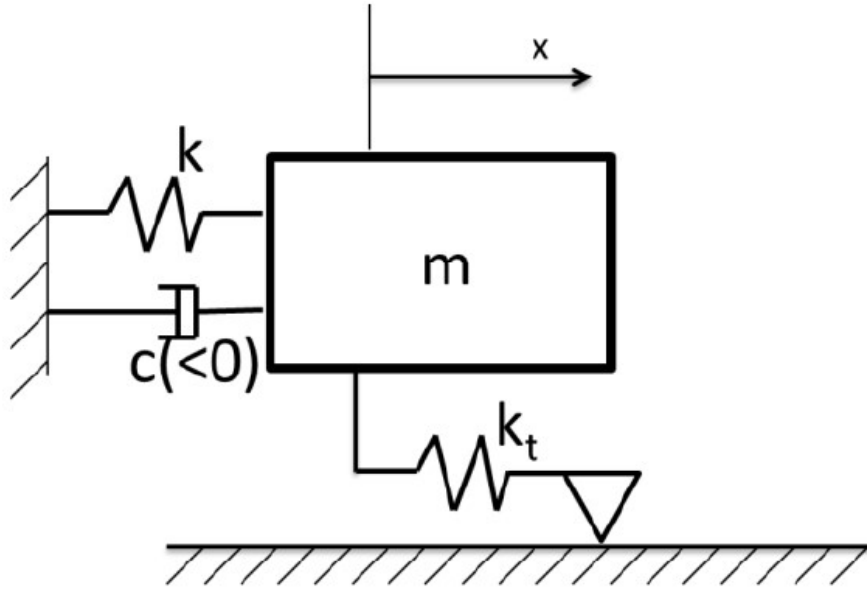


Figure 3.5: Model 1 D.O.F. with sliding contact for FREEVIB validation

### 3.3.1 Sliding contact pattern

The "spring-slider" contact model developed and applied by many authors [21], [22], [23], [24]. Its simplest formulation includes a constant normal preload force  $N_0$ , a tangential stiffness  $k_t$ , and a coefficient of friction  $\mu$ , as shown in Figure 3.5.

The displacement of the single degree of freedom is indicated by  $x$  and the relative sliding by  $w$ . The tangential force at the contact  $T$  varies according to the state of the contact (adhesion or sliding):

$$T(t) = \begin{cases} k_t \cdot (x(t) - w(t)) & \text{Stick} \\ \mu \cdot N_0 \cdot \text{sign}(\dot{w}) & \text{Slip} \end{cases} \quad (3.14)$$

where the contact states are defined as:

$$\begin{cases} \dot{w} = 0 & \text{Stick} \\ \dot{x} = \dot{w} \neq 0 & \text{Slip} \end{cases}$$

The following criteria dictate the transition from one contact state to another, which is analyzed in detail in [21]:

The transition occurs from stick to slip when  $|T| = \mu \cdot N_0$  and from slip to stick when  $\dot{w} = 0$

### 3.3.2 Method of temporal integration

In the Newmark method, for the time integration of the equilibrium equations of the system:

$$M\ddot{q}_{n+1} + C\dot{q}_{n+1} + Kq_{n+1} + F_c(q_{n+1}, \dot{q}_{n+1}) = F_e \quad (3.15)$$

This method adopted, in which it is assumed:

$$\begin{cases} \dot{q}_{n+1} = \dot{q}_n + \Delta t \ddot{q}_\gamma & \text{with } \ddot{q}_\gamma = (1 - \gamma)\ddot{q}_n + \gamma\ddot{q}_{n+1} & 0 \leq \gamma \leq 1 \\ q_{n+1} = \dot{q}_{n+1} + \Delta t \Delta t \dot{q}_n + \frac{\Delta t^2}{2} \ddot{q}_\beta & \text{with } \ddot{q}_\beta = (1 - 2\beta)\ddot{q}_n + 2\beta\ddot{q}_{n+1} & 0 \leq 2\beta \leq 1 \end{cases}$$

$$\begin{cases} \ddot{\mathbf{q}}_{n+1} = f(\mathbf{q}_{n+1}) = \frac{1}{2\beta} \left[ \frac{\mathbf{q}_{n+1} - \mathbf{q}_n - \Delta t \dot{\mathbf{q}}_n}{\Delta t^2/2} - (1 - 2\beta)\ddot{\mathbf{q}}_n \right] \\ \dot{\mathbf{q}}_{n+1} = g(\mathbf{q}_{n+1}) = \dot{\mathbf{q}}_n + (1 - \gamma)\Delta t \ddot{\mathbf{q}}_n + \gamma\Delta t \cdot f(\mathbf{q}_{n+1}) \end{cases}$$

For each  $n^{\text{th}}$  time step of amplitude  $\Delta t$ , the following system of equations in the unknown  $\mathbf{q}_{n+1}$  is obtained:

$$Mf(\mathbf{q}_{n+1}) + Cg(\mathbf{q}_{n+1}) + K\mathbf{q}_{n+1} + F_c(\mathbf{q}_{n+1}, g(\mathbf{q}_{n+1})) = F_e \quad (3.16)$$

For the parameters  $\gamma$ ,  $\beta$  the values were chosen:  $\gamma = 1/2$  and  $\beta = 1/4$ , which guarantee unconditional stability of the method and the lack of numerical damping, as stated in [27] and [28]. The range of  $\Delta t$  was chosen in such a way to ensure convergence of the method  $\omega\Delta t < 2$  as referred to in [27],

$$\Delta t = 0.02 \frac{2}{\max\{\omega_{n\text{stick}}\}}$$

The system of equations must be solved iteratively at each integration step due to the nonlinearity introduced by the contact force  $F_c$ . This force is managed with the method set out below.

### 3.3.3 State Contact and the relevant contact force

The state of the contact at each time step and the consequent tangential force is determined using the Forecast-Correction method used in [23], [24], [28] as shown in Figure 3.6:

1. PREDICTOR STEP: it is assumed that at the  $(n + 1)$ th step, the contact is in stick:

$$\begin{aligned} Hp: \quad \dot{w} = 0 &\Rightarrow w_{n+1}^p = w_n \\ T^p &= k_t \cdot (x_{n+1} - w_{n+1}^p) \end{aligned} \quad (3.17)$$

The solution using the Newmark method is  $x_{n+1}^p = q_{n+1}^p$ .

2. CORRECTOR STEP: the validity of the assumption on the status of the contact is verified:

If  
 $|T^p| < \mu N_0$  then, contact in stick,  $x_{n+1} = x_{n+1}^p$

Else

$$\text{Contact in slip} \begin{cases} T_{n+1} = \mu N_0 \cdot \text{sign}(T^p) \\ w_{n+1} = x_n - \frac{T_{n+1}}{k_t} \end{cases}$$

$x_{n+1}$  recalculated with Newmark with true  $T_{n+1}$

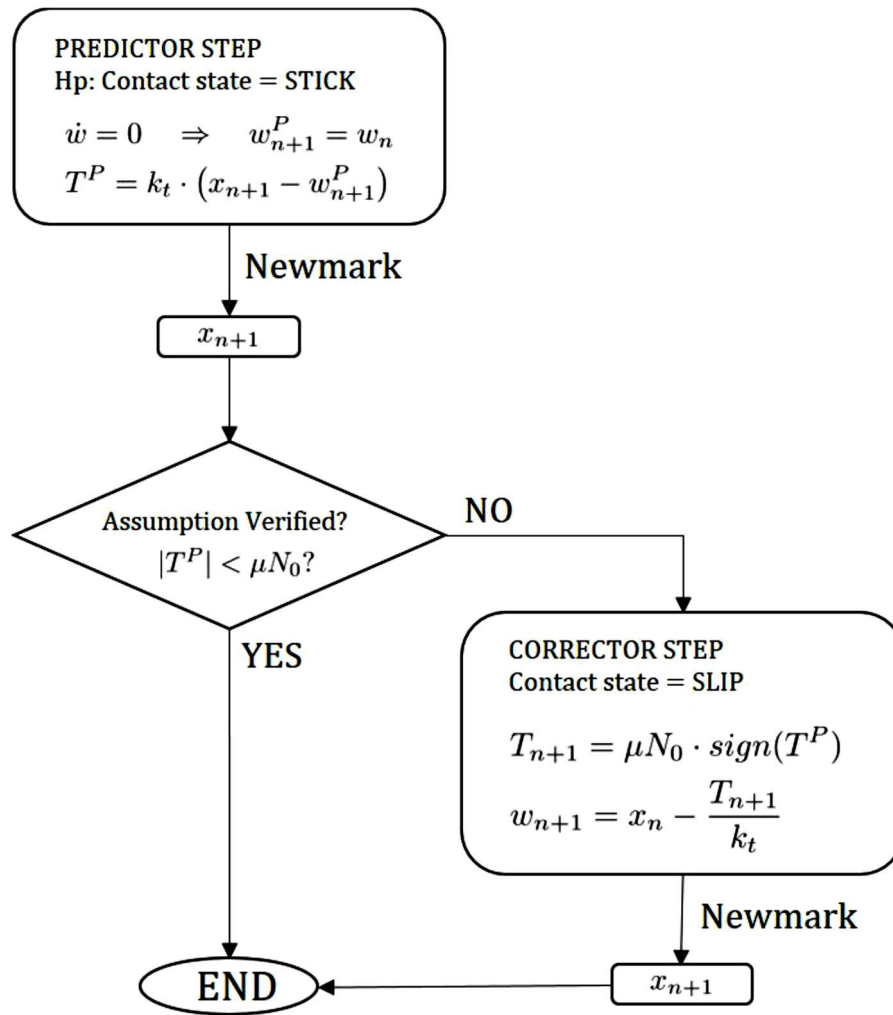


Figure 3.6. Predictor-Corrector scheme

### 3.4 Comparison between the theoretical modal parameters and FREEVIB method

The developed FREEVIB version in this work can only be applied to frequency-independent dampings, such as structural and friction damping systems. The one-degree-of-freedom model used for code validation should therefore have structural (and non-viscous) damping in addition to sliding contact. However, the temporal integration of systems containing the structural damping of the Kelvin model requires particular methods to obtain a stable solution, such as the integration back in time for the modal coordinates associated with unstable poles, presented in [5]. Structural and viscous damping has the following equivalence for linear systems:

$$\eta = 2\zeta \frac{\omega}{\omega_n} \quad (3.18)$$

which in the case of free decay, where  $\omega = \omega_n$  for the linear case, becomes:

$$\eta = 2\zeta$$

In this work, a model with a D.O.F. is adopted with viscous damping to check the frequency and damping values in a complete adhesion contact state.

Subsequently, a model without damping is adopted to verify the nonlinear damping trend and frequency as a function of vibration amplitude. The results will be compared

with the theoretical trends obtained with the Single Harmonic Balancing Method (SHBM)[29].

To verify the values during the complete adhesion state, the parameters for the 1 D.O.F. was chosen arbitrarily. Then damping  $\eta$ , natural frequency  $f_n$  during the complete adhesion of the contact (linear system), and the amplitude of critical oscillation  $X_{Cr}$  beyond which sliding is possible have been calculated [29].

$$\begin{aligned}
 k_t &= 4 \cdot 10^6 \text{ N/m} \\
 \mu &= 0.08 \\
 N_0 &= 5000 \text{ N} \\
 M &= 0.700 \text{ kg} \\
 K &= 4.2 \cdot 10^6 \text{ N/m} \\
 \zeta &= 2.5 \cdot 10^{-3} \\
 C &= \zeta \cdot 2\sqrt{M(K + k_t)} \\
 X(t=0) &= 100 \cdot X_{Cr}
 \end{aligned}
 \Rightarrow
 \begin{aligned}
 \eta &= 2\zeta = 0.5 \cdot 10^{-2} \\
 f_n &= 544.73 \text{ Hz} \\
 X_{Cr} &= \frac{\mu N_0}{k_t} = 100 \mu\text{m} \\
 F_{C_{max}} &= \mu N_0 = 400 \text{ N}
 \end{aligned}$$

The frequency and damping and also the contact state for this example is shown in Figure 3.7.

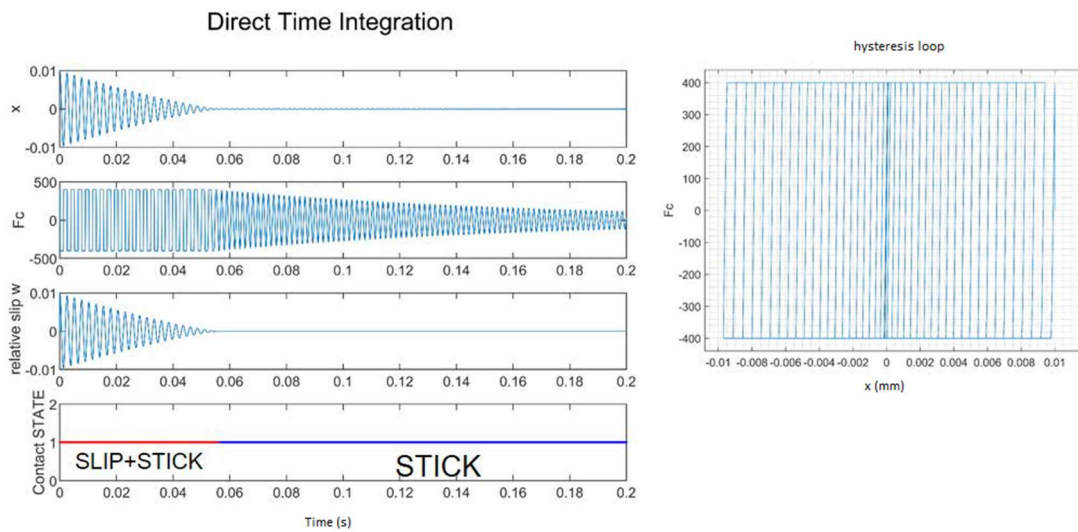


Figure 3.7: 1 D.O.F. Model, Direct integration

In Figure 3.8, the result of FREEVIB application to the model with a degree of freedom is shown. The frequency obtained under adhesion conditions corresponds to theoretical ( $f_n=544.73[\text{Hz}]$ ) with an error of 0.03% and the damping ( $\eta=5 \cdot 10^{-3}$ ) with an error of 0.11%. The critical vibration amplitude ( $X_{Cr}=\mu N_0/k_t=100\mu\text{m}$ ) has the largest error by 6.3%.



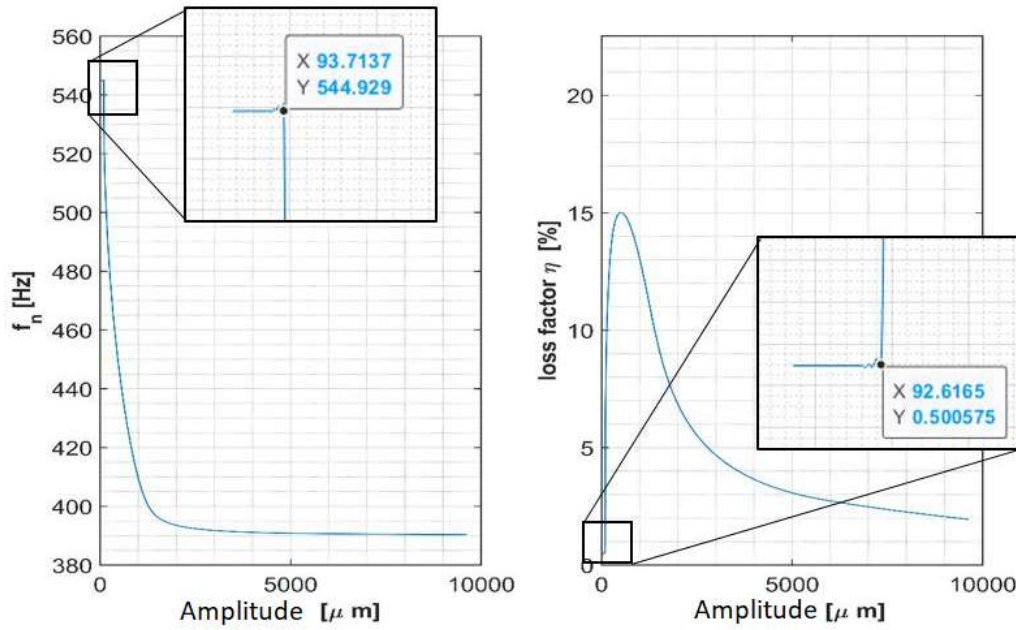


Figure 3.8: Application of the FREEVIB method to the 1 DOF model

The nonlinearity corresponds to the theoretical prediction which presented by the Single Harmonic Balance Method [29]. Then the sliding contact can be represented with an equivalent stiffness and equivalent damping as below:

$$\frac{k_{eq}}{k_t} = \frac{1}{\pi} \left( \theta_B - \frac{1}{2} \sin(2\theta_B) \right) \quad \frac{c_{eq}}{k_t} = \frac{4}{\pi} \frac{1}{\left( \frac{x_0}{x_{Cr}} \right)} \left( 1 - \frac{1}{\left( \frac{x_0}{x_{Cr}} \right)} \right) \quad 3.19$$

Where

$$\theta_B = \arccos \left( 1 - \frac{2}{\left( \frac{x_0}{x_{Cr}} \right)} \right) \quad x_{Cr} = \frac{\mu N_0}{k_T} \quad x_0 \text{ is the amplitude of oscillation}$$

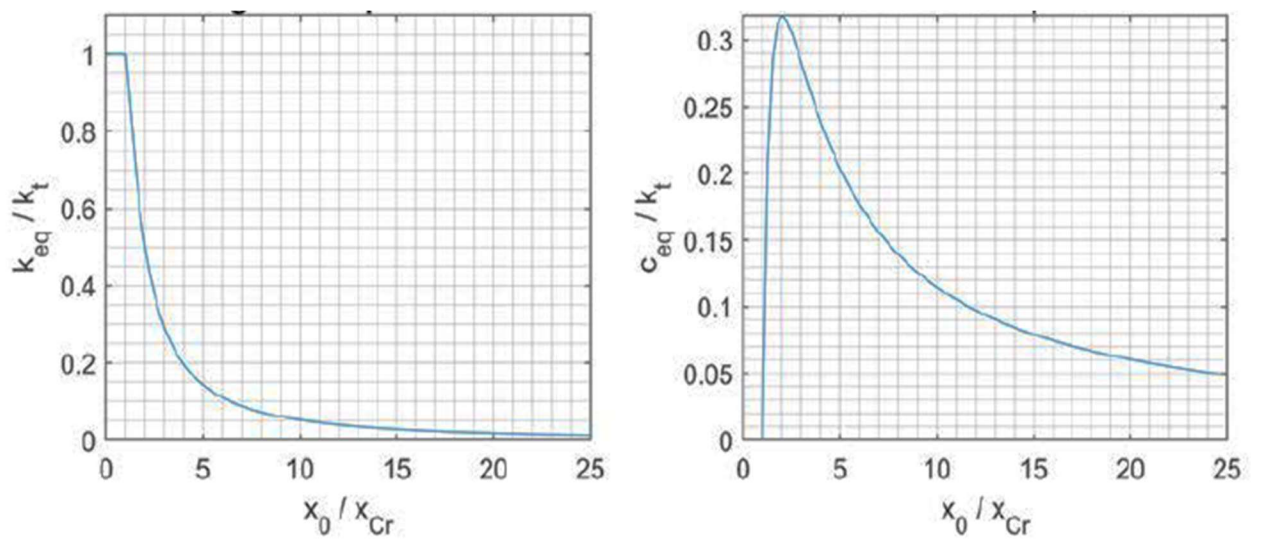


Figure 3.9: Equivalent stiffness and damping provided by the SHBM

## 3.5 Analysis of the measurements

In this section, analysis of the measurements obtained during the experimental procedure is investigated. It includes the first flexural mode, the second flexural mode, the effect of vibration amplitude, and the axial load on frequency and damping. It leads to the proper selection of the target to investigate the contact stiffness in a diverse range of axial loads.

### 3.5.1 First Flexural Mode

To investigate the effect of vibration amplitude and traction force on frequency and damping in the first flexural mode, the measurement point is shown in Figure 3.10. It is supposed to be in the beam's middle point to be matched with the relevant mode shape.

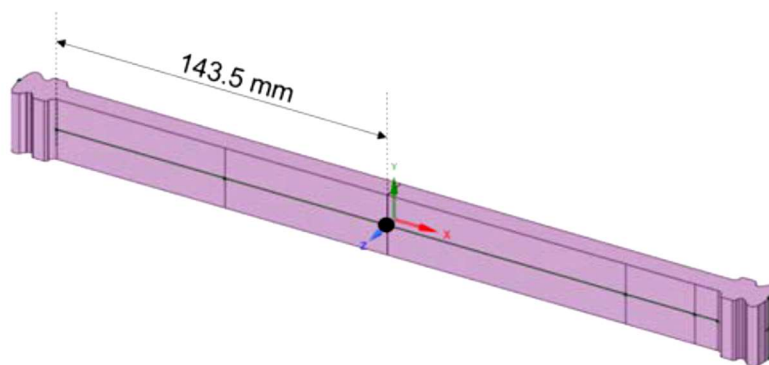


Figure 3.10: Measurement point for First Flexural Mode

#### 3.5.1.1 Effect of vibration amplitude on frequency and damping

##### Damping

The dependence of damping on vibration amplitude, visible in Figure 3.11, confirms the results by the Single Harmonic Balance Method [29].

The vibration amplitude shown in the below graphs is on the point indicated in Figure 3.10, which is the antinode of the first flexural mode. The damping trend by the SHBM was reported as a function of oscillation amplitude of the contact points, which in the case in question are the contact points of the dovetail joints. For small vibration amplitudes, there is constant damping, i.e., independent of the amplitude, which is an index of complete adhesion of contact areas. Therefore, it implies the linearity of the system in question. For amplitudes greater than a critical value, the damping shows a steep increase, indicating the beginning of possible sliding in the contact areas and the establishment of the hysteresis cycle due to the alternation between adhesion and sliding states during each oscillation cycle.

Dissipation of energy due to this phenomenon has a maximum according to the vibration amplitude, as can be seen in Figure 3.11, beyond which the damping decreases.

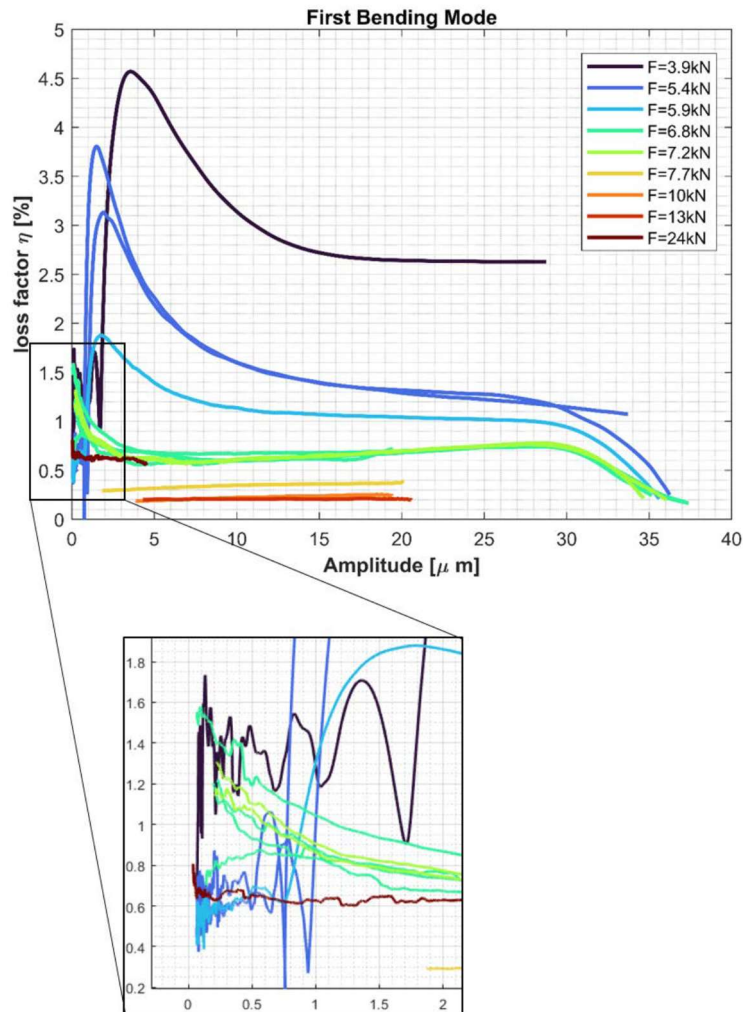


Figure 3.11: First Flexural Mode: Damping as a function of amplitude

## Frequency

The frequency dependence on the vibration amplitude, visible in Figure 3.12, differs from the Single Harmonic Balance Method [29], which was analyzed previously. This is likely due to the following factors:

- In Figure 3.12, the frequency is shown as a function of the oscillation amplitude on the antinode of the first flexural mode, different from the point of contact, as explained in detail in the previous paragraph.
- The frequency of the first inflectional model shown in Figure 3.12 depends on the behavior of four contact areas, including two for each dovetail joint. Instead, in the graphs of SHBM, the single contact is analyzed.

For small vibration amplitudes, it is still possible to observe a constant frequency, i.e., independent of amplitude as an index of complete adhesion, which implies the linearity of the system in question.

For amplitudes greater than a critical value, the frequency presents a step decrease, indicating the beginning of possible sliding in contact areas and the establishment of the hysteresis cycle due to the alternation between adhesion and sliding states during each oscillation cycle.

For low values of traction force, it is hypothesized that stiffening (frequency increase) observable as the vibration amplitude increases is due to the variation of normal force at contact areas caused by beam bending. An increase in this normal force could imply an

adhesion state. On the other hand, the hypothesis of constant normal force would be in sliding conditions.

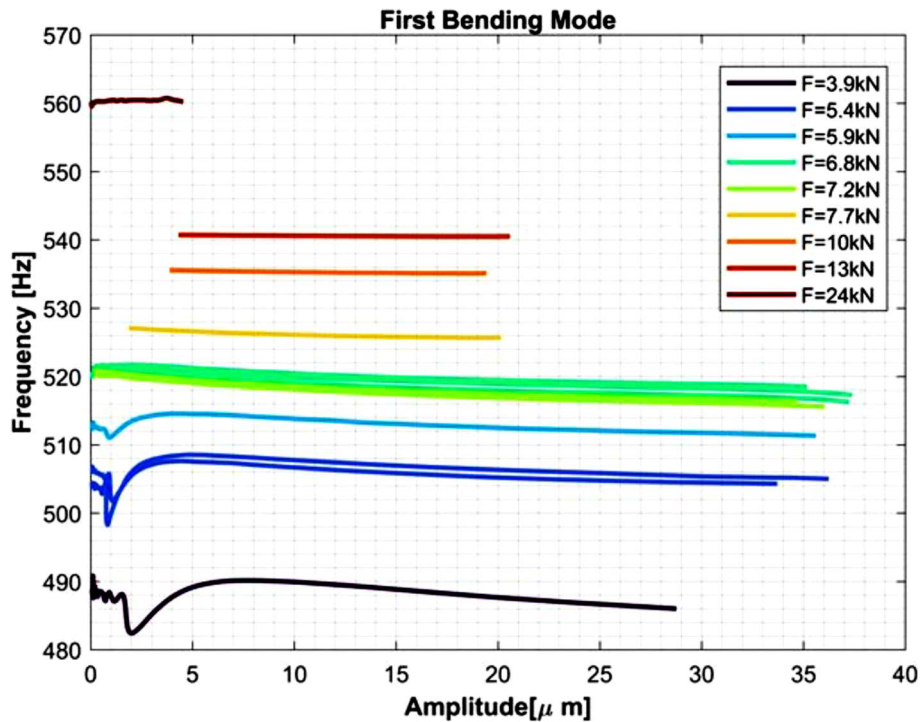


Figure 3.12: Frequency as a function of Amplitude Effect of traction force on frequency and damping for first flexural mode

### 3.5.1.2 Effect of traction force on frequency and damping

#### Damping

Figure 3.11 shows a reduction in the maximum damping as the traction force increases. This behavior can be explained by assuming that not all four contact areas are in the state of macro-slip, but there are some contact areas in the micro-slip state, sliding only at the edges of the contact area. This hypothesis is compatible with the previous supposition of variation in force normal on the contact areas caused by the bending of the beam.

In this hypothesis, an increase in traction force would imply an increase in normal contact force. For micro-slip areas, an increase in contact area in complete adhesion and a reduction in the peripheral area subject to sliding, caused a consequent reduction of energy dissipation and, therefore, damping.

Figure 3.13b, represents the damping under adhesion conditions as a function of traction force. There is also an increase in the average value of frequency (average with respect to the vibration amplitude) as the traction force increases as shows in Figure 3.13a.

This stiffening effect is also clearly visible in Figure 3.13a, which also shows the theoretical trend obtained from the model of Euler-Bernoulli beam stuck at the two ends, modified to consider the braking moment due to the normal stress in the deformed configuration of the beam [30].

Figure 3.13a also shows that for axial forces less than about 12kN, the frequency trend differs from the theoretical one. This phenomenon was also described in [1], where

it is assumed that for low values of traction force, micro-slips are present in contact areas, decreasing the effective stiffness of the dovetail joint.

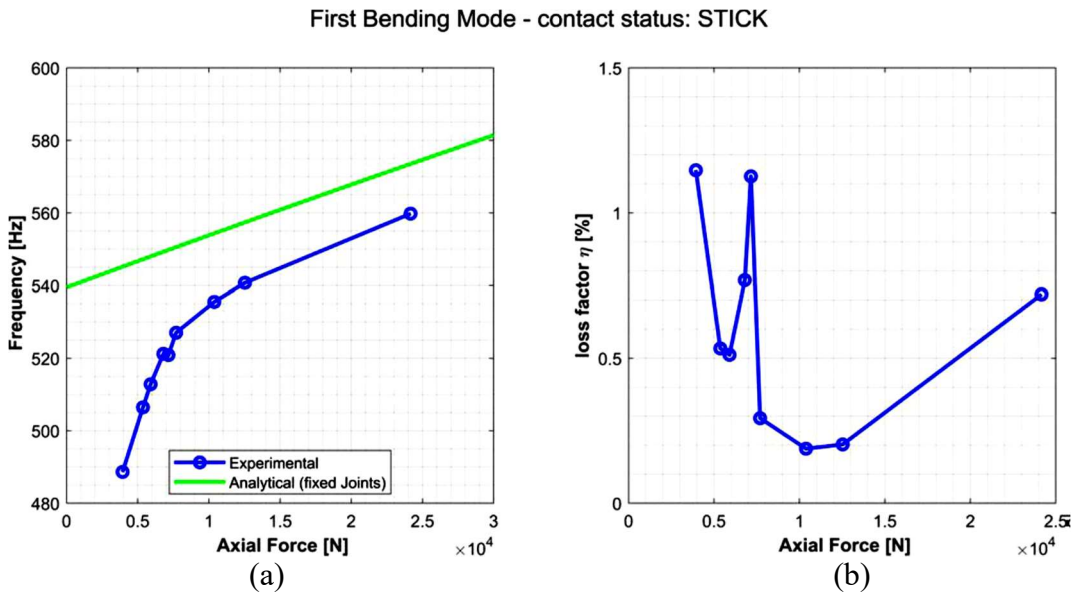


Figure 3.13: Effect of the tensile force on  $f_n$  and  $\eta$  under adhesion conditions

Visualization of combined effects of axial force and amplitude on damping and frequency in the first flexural mode is shown in Figure 3.14 and Figure 3.15.

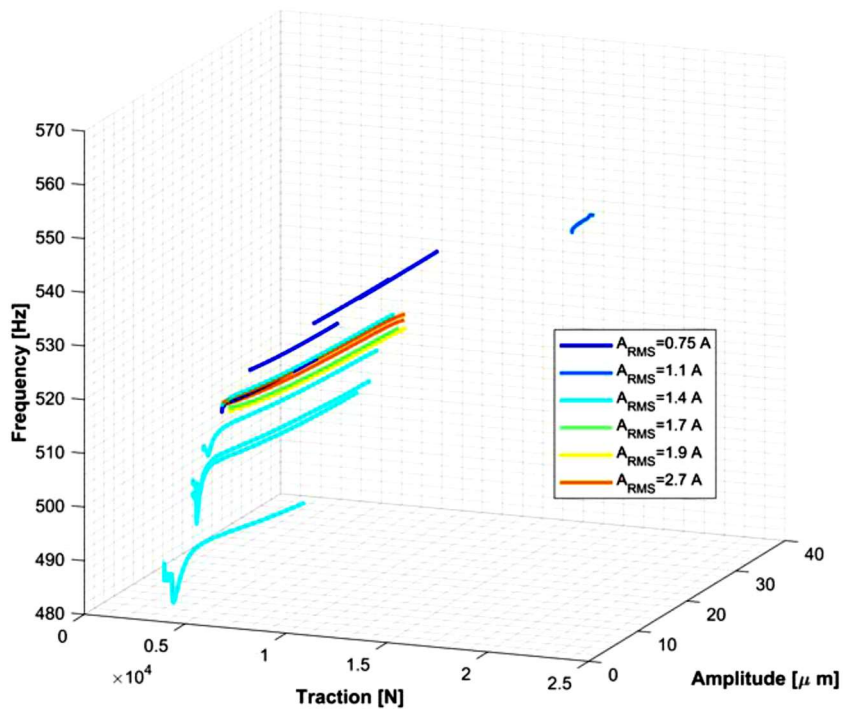


Figure 3.14: Natural frequency as a function of vibration amplitude and traction

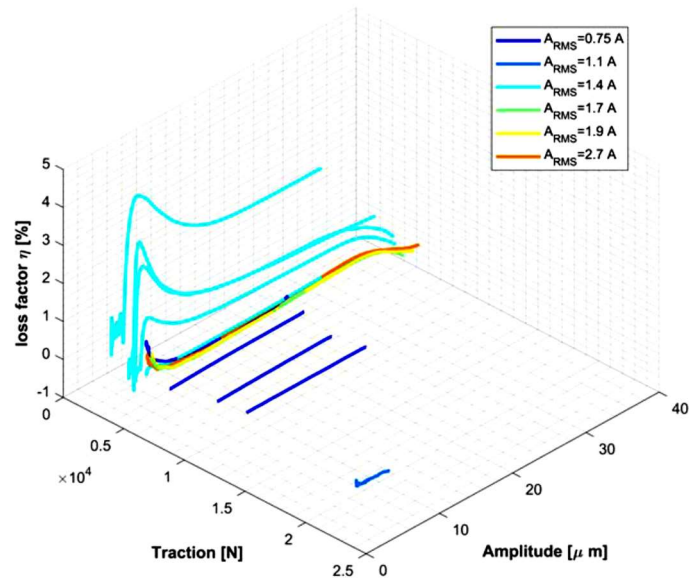


Figure 3.15: Damping as a function of the vibration amplitude and traction

### 3.5.2 Second Flexural Mode

To investigate the effect of vibration amplitude and traction force on frequency and damping in the first flexural mode, the measurement point is shown in Figure 3.16. It is supposed to be in this point to be matched with the relevant mode shape.

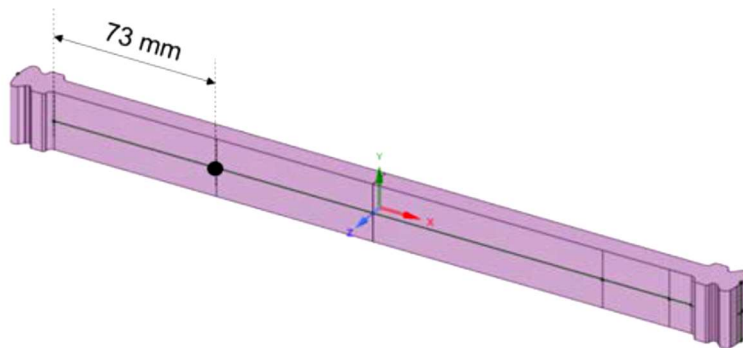


Figure 3.16: Second Flexural Mode measurement point

### 3.5.2.1 Effect of vibration amplitude on frequency and damping

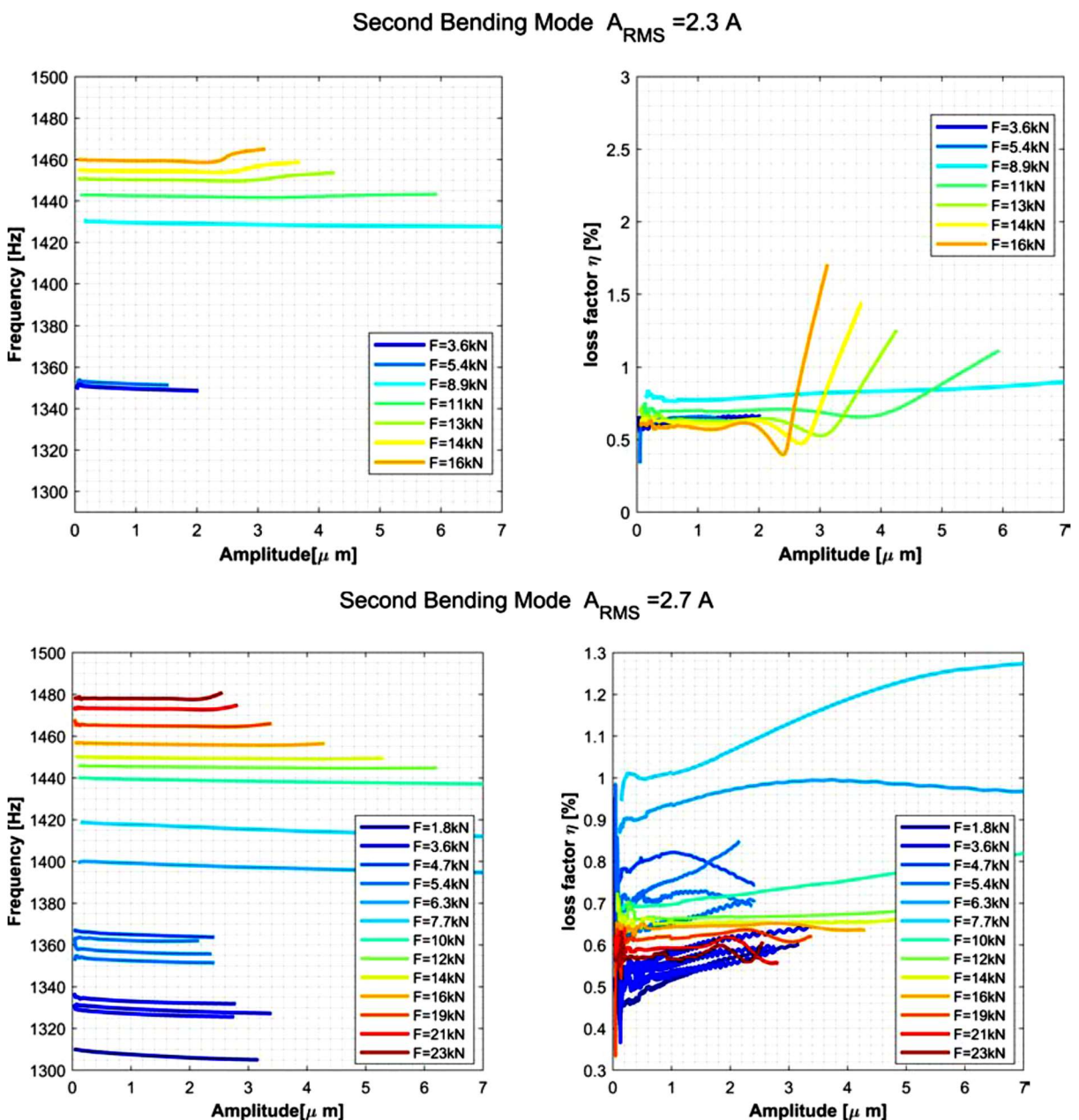
#### Damping

The dependence of damping on the vibration amplitude in the second flexural mode (Figure 3.17) recalls what was found for the first mode. There is an initial stretch of constant damping that is not dependent on the amplitude and a critical value beyond which the sliding begins, causing the steep growth of the damping.

For the same traction force, the critical amplitude depends on the effective  $A_{RMS}$  input current to the shaker. This current defines the amplitude of the exciting force before detachment of the shaker tip from the blade that means the vibration amplitude at the beginning of free decay.

#### Frequency

Dependence of the frequency to vibration amplitude (Figure 3.17) has a constant trait for low amplitude values, indicating the complete adhesion of contact areas.



### Second Bending Mode $A_{RMS} = 3.1 \text{ A}$

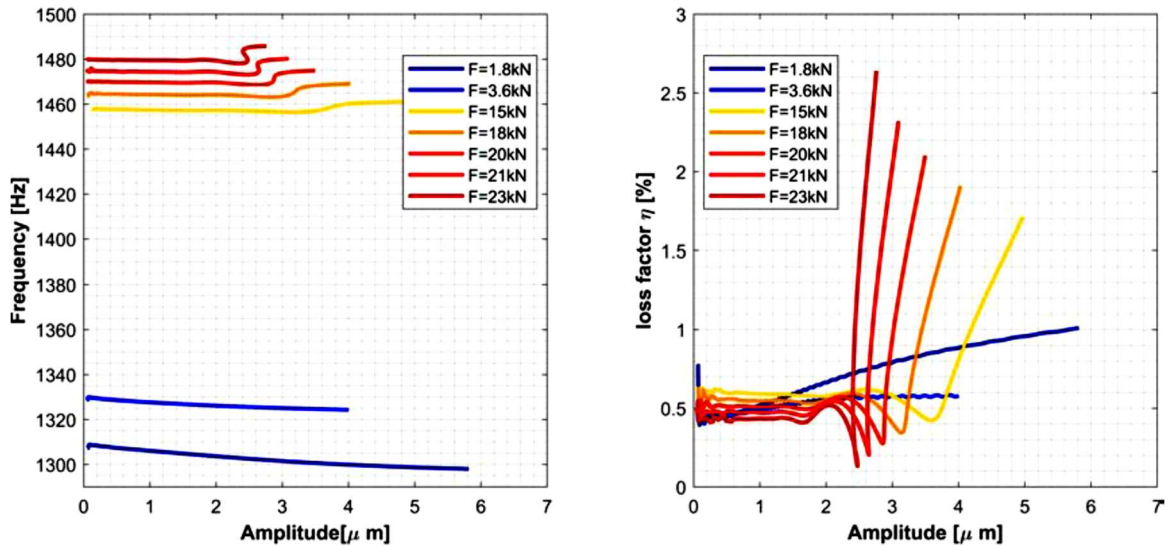


Figure 3.17: Second Flexural: Frequency =  $f_n$  (Amplitude), damping =  $\eta$  (Amplitude) for different values of effective ARMS current sent to the shaker

### 3.5.2.2 Effect of traction force on frequency and damping

#### Damping

As shown in Figure 3.17 and the second graph of Figure 3.18, incomplete damping adhesion has a maximum of about 8kN applied force, beyond which it decreases as the traction force increases. Also, a slight variability of the results was found as a function of  $A_{RMS}$  current entering the shaker.

From the graphs in Figure 3.17, there is a decrease in the critical amplitude as the traction force increases. Such a phenomenon also presents for the first flexion mode, to which a hypothesis was referred.

#### Frequency

The frequency trend as a function of traction force (Figures 3.17, 3.18) re-proposes the stiffening effect which was already found for the first flexural mode, with the deviation of the measured frequencies from the theoretical ones for low force values, a phenomenon probably due to the micro slip in the contacts.



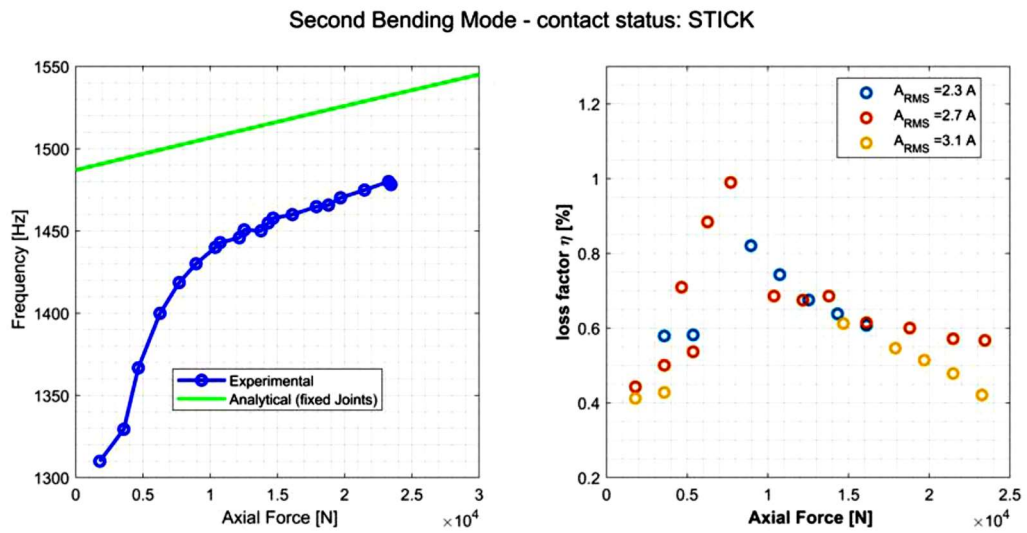


Figure 3.18: Effect of the tensile force on  $f_n$  and  $\eta$  under adhesion conditions

Visualization of the combined effects of axial force and amplitude on damping and frequency in the second flexural mode is shown in Figure 3.19 and Figure 3.20.

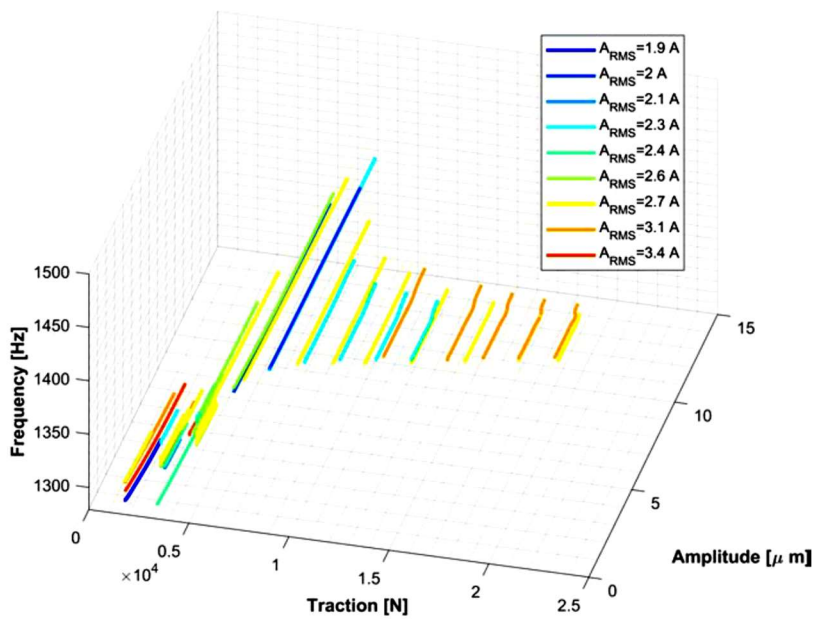


Figure 3.19: Frequency as a function of the amplitude of vibration and traction

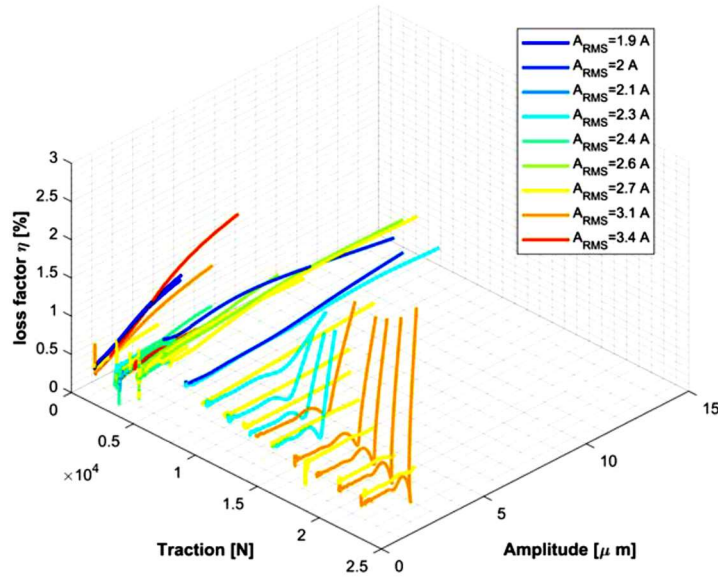


Figure 3.20: Damping as a function of vibration amplitude and traction

### 3.6 Estimation of errors

Measurement inaccuracies are critical when estimating the damping of a lightly damped structure. It is inevitable to have some errors during the measurement, so to increase the confidence in the results, a procedure is proposed in Appendix F to calculate the measurement error propagation to the calculated frequency and damping. The possible sources of the inaccuracy in the measurements can be summarized as follows:

1. uncertainty of axial traction force due to accuracy of pressure gauge used to measure the actuator pressure. This type of error can be easily estimated considering the accuracy of the pressure gauge:

$$\frac{\delta p}{p} = 1\% \quad @700bar$$

$$F = A_{cyl} \cdot p \rightarrow \frac{\delta F}{F} = 1\%$$

2. uncertainty of speed measurement due to the precision of laser interferometer and consequent propagation of this error in the signal analysis procedure

The error analysis was carried out only in the range of vibration amplitudes for which the contacts can be considered in full adhesion or where frequency and damping have a constant trend, not dependent on the amplitude.

For each axial force, the mean  $\bar{f}_j$ ,  $\bar{\eta}_j$  and the standard deviation were calculated  $(\sigma_f)_j$ ,  $(\sigma_\eta)_j$  for each j-th frequency and damping measurement.

$$f_j = \bar{f}_j \pm (\sigma_f)_j \quad (\sigma_f)_j = \sqrt{\frac{1}{n-1} \sum_i (f_i - \bar{f})^2}$$

$$\eta_j = \bar{\eta}_j \pm (\sigma_\eta)_j \quad (\sigma_\eta)_j = \sqrt{\frac{1}{n-1} \sum_i (\eta_i - \bar{\eta})^2} \quad (3.20)$$

The average values of all measurements carried out at the same axial force were then calculated and the error propagation was calculated using the formula:

$$x = \frac{\sum_j x_j}{N} \quad \delta x = \sqrt{\sum_j \left( \frac{\partial x}{\partial x_j} (\sigma_x)_j \right)^2} = \sqrt{\sum_j \left( \frac{1}{N} (\sigma_x)_j \right)^2} \quad x = f, \eta \quad (3.21)$$

$F_{ax}$ [N]	$f_n$ [Hz]	$\delta f_n$ [Hz]	$\delta f_n/f_n$	$\eta$	$\delta \eta$	$\delta \eta/\eta$
3580	480.03	0.28	0.058%	0.04864	0.00034	0.7%
3938	488.64	0.51	0.103%	0.01147	0.00049	21.7%
5370	505.34	0.11	0.022%	0.00573	0.00074	12.9%
5907	512.34	0.20	0.039%	0.00512	0.00066	12.8%
6802	521.17	0.08	0.013%	0.01121	0.00024	2.1%
7160	522.41	0.04	0.007%	0.01174	0.00030	2.6%
7697	527.78	0.02	0.004%	0.00293	0.00002	0.6%
10382	535.22	0.01	0.002%	0.00188	0.00001	0.6%
12530	540.31	0.01	0.001%	0.00203	0.00001	0.2%
24165	559.87	0.11	0.021%	0.00721	0.00041	5.8%

Table 3.1: First Flexural Mode: Error estimate - contact Status: STICK

$F_{ax}$ [N]	$f_n$ [Hz]	$\delta f_n$ [Hz]	$\delta f_n/f_n$	$\eta$	$\delta \eta$	$\delta \eta/\eta$
1790	1300.42	0.10	0.007%	0.00456	0.00023	5.1%
3401	1292.21	0.20	0.015%	0.00418	0.00030	5.0%
3580	1333.48	0.18	0.013%	0.00511	0.00021	7.2%
3759	1328.07	0.21	0.016%	0.00391	0.00058	4.1%
4654	1366.83	0.14	0.010%	0.00757	0.00062	14.8%
5012	1361.97	0.49	0.036%	0.00731	0.00014	8.2%
5191	1364.20	0.17	0.012%	0.00638	0.00017	1.9%
5370	1363.86	0.26	0.019%	0.00679	0.00025	2.7%
5549	1382.93	0.12	0.009%	0.00739	0.00029	3.7%
6265	1399.80	0.11	0.008%	0.00880	0.00005	3.9%
7160	1406.46	0.15	0.010%	0.01152	0.00007	0.6%
7697	1418.69	0.09	0.006%	0.00975	0.00016	0.6%
8950	1430.47	0.09	0.006%	0.00828	0.00009	1.6%
10382	1440.05	0.07	0.005%	0.00684	0.00003	1.1%
10740	1443.01	0.13	0.009%	0.00731	0.00018	0.4%
12172	1445.92	0.04	0.003%	0.00684	0.00011	2.5%
12530	1450.65	0.06	0.004%	0.00691	0.00017	1.6%
13783	1450.10	0.03	0.002%	0.00696	0.00017	2.5%
14320	1454.84	0.02	0.001%	0.00627	0.00015	2.4%
14678	1457.82	0.04	0.002%	0.00618	0.00007	2.4%
16110	1458.34	0.07	0.005%	0.00615	0.00008	1.1%
17900	1464.49	0.35	0.024%	0.00541	0.00031	1.3%
18795	1466.33	0.77	0.053%	0.00527	0.00089	5.7%
19690	1470.16	0.06	0.004%	0.00522	0.00012	16.9%
21480	1474.05	0.06	0.004%	0.00531	0.00009	2.3%
23270	1480.02	0.17	0.011%	0.00452	0.00038	1.7%
23449	1478.18	0.03	0.002%	0.00567	0.00002	8.4%

Table 3.2: Second Flexural Way: Error estimate - contact Status: STICK

# Chapter 4

## Numerical Simulations

### 4.1. The general procedure of simulation with Finite Elements

The objective of the numerical part of this work is to find the normal and tangential stiffness values,  $k_n$  and  $k_t$  of the contact areas of the dovetail joint, as shown in Figure 4.1. These values represent the input parameters of the typical Node-to-Node contact elements used in numerical simulations [21-23, 35, 36].

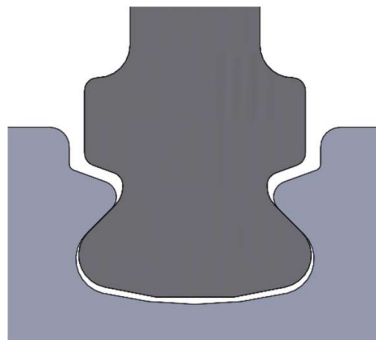


Figure 4.1: Dovetail joint under examination

The following procedure was followed to find the values of  $k_n$  and  $k_t$ :

1. The blade model with two dovetail ends was discretized with the finite element method implemented in ANSYS ®, as well as the beam supports (slots), paying particular attention to the coincidence of nodes in the contact interfaces
2. As the axial traction force changes, nonlinear static analysis was carried out just on the blade to obtain the stiffening effect of this force in stiffness matrices of the blade, which will be used later.

3. Model degrees of freedom were reduced using Craig-Bampton's Component Mode Synthesis technique [35]. Then the reduced model of mass and stiffness matrices were imported into MATLAB®. The reduction includes the contact nodes and other nodes necessary for displaying the modes.
4. The reduced models of the beam and supports were assembled in MATLAB® by introducing linear contact elements, i.e., contact elements that do not implement the sliding or separation state of the contact. The parameters of these elements are the values of  $k_n$  and  $k_t$ , which are the object of this research.
5. A developed code compares the frequencies of the first and second flexural modes of the F.E. model with corresponding frequencies obtained from the analysis of measurements. It is done in the range of axial traction forces in which complete adhesion of the contacts was found, which implies linearity of contacts.

## 4.2. Finite Element Model

The model was discretized with a structured mesh where possible. SOLID185 8-node hexahedral linear elements were used, the size of which was gradually reduced in the vicinity of the contact areas as shown in Figure 4.2

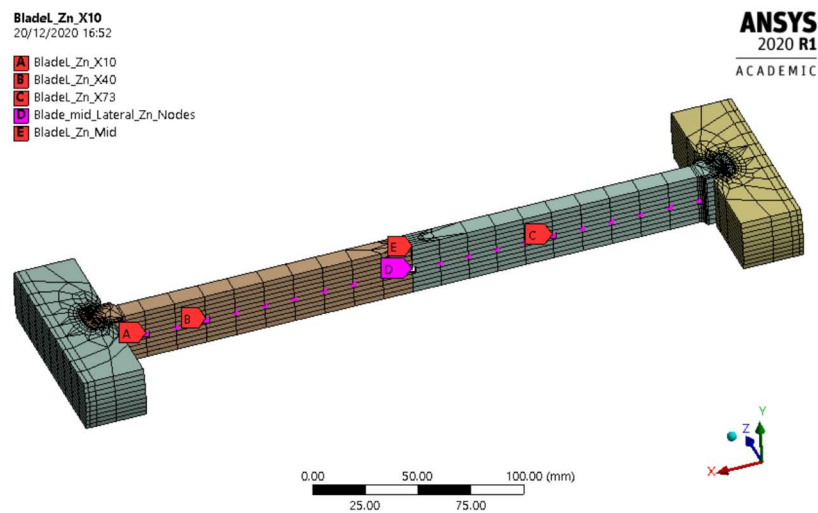


Figure 4.2: F.E. model of the blade simulacrum and slots

As shown in Figure 4.3, the coincidence of the beam nodes and the slots in the contact interfaces has been set geometric to use Node-to-Node contact elements in the subsequent assembly.

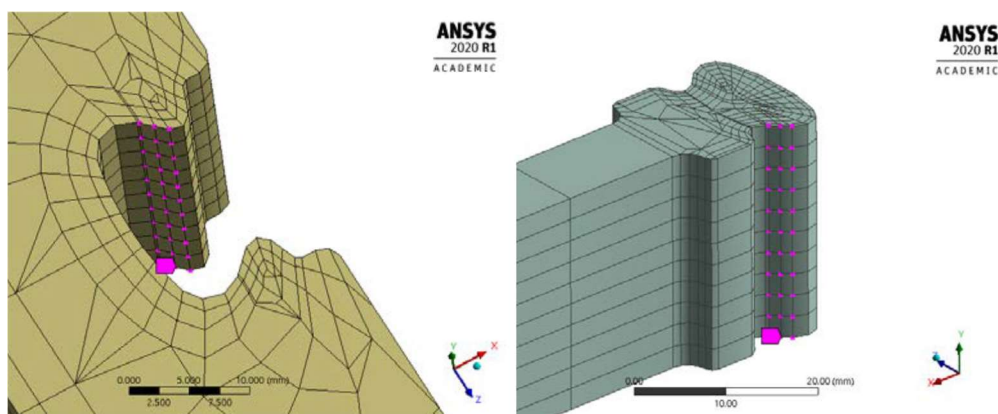


Figure 4.3: Nodes at the contact interface

In order to subsequently insert the contact elements, the nodes at the interface must be distinct and coincident only in the position. In other words, for each pair of nodes having the same position, the identification number of the beam node must be different from the slot node. However, the distinction between beam nodes and slots for interfaces is only necessary during the assembly of the bodies in MATLAB®, while in ANSYS®, beam and slots will be analyzed individually.

### 4.3 Stiffening effect of the axial load

To consider the nonlinearity due to the stiffening effect of the axial traction force, the static analyzes just on the beam should be carried out as the force varied. The additional stiffness matrix  $\Delta K_F$  was obtained for each force, which will be considered in the subsequent C.M.S. reduction of the model. Total stiffness can be defined as below:

$$K = K_{(F=0)} + \Delta K_F \quad (4.1)$$

$$\Delta K_F = \int_{vol} [S_g]^T [\sigma] [S_g] dvol \quad (4.2)$$

where  $[\sigma]$  is the stress tensor and  $[S_g]$  is the matrix of the derivatives of the shape functions [36].

The beam was loaded on both ends with forces normal to the contact areas, simulating the limit condition of zero tangential forces on contact. The reference loading for each static analysis is the axial force  $F_{ax}$  visible in Figure 4.4. The normal loads at the  $N_0$  contact were therefore imposed as a function of the axial force. So, from the balance of forces:

$$N_0 = \frac{F_{ax}}{2 \sin(\theta)} \quad \text{with } \theta = 45^\circ$$

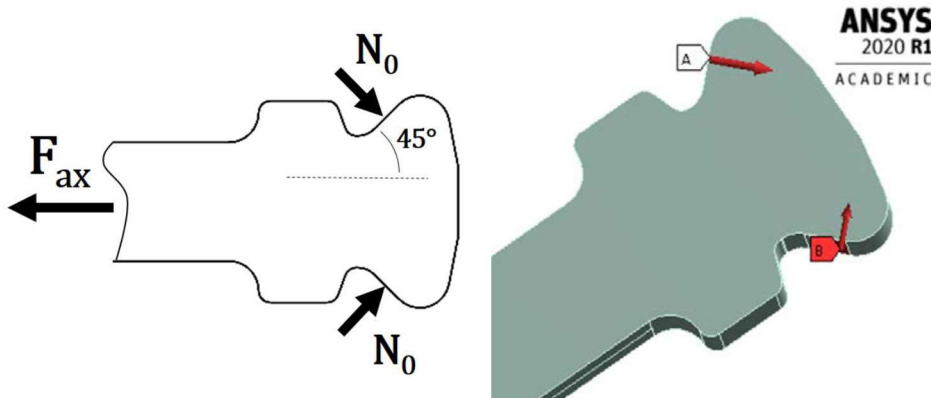


Figure 4.4: Load system for static analysis

The loaded blade thus is subject to a self-balanced system of forces. It does not require reactions. However, the software does not allow the static analysis to be carried out without introducing constraints. As shown in Figure 4.5, four elastic supports with stiffness close to zero are considered on specific nodes to avoid the influence on

subsequent analysis. These nodes are located in the first, middle and last nodes of the mid line of blade bottom. Another node is also selected in the mid of blade.

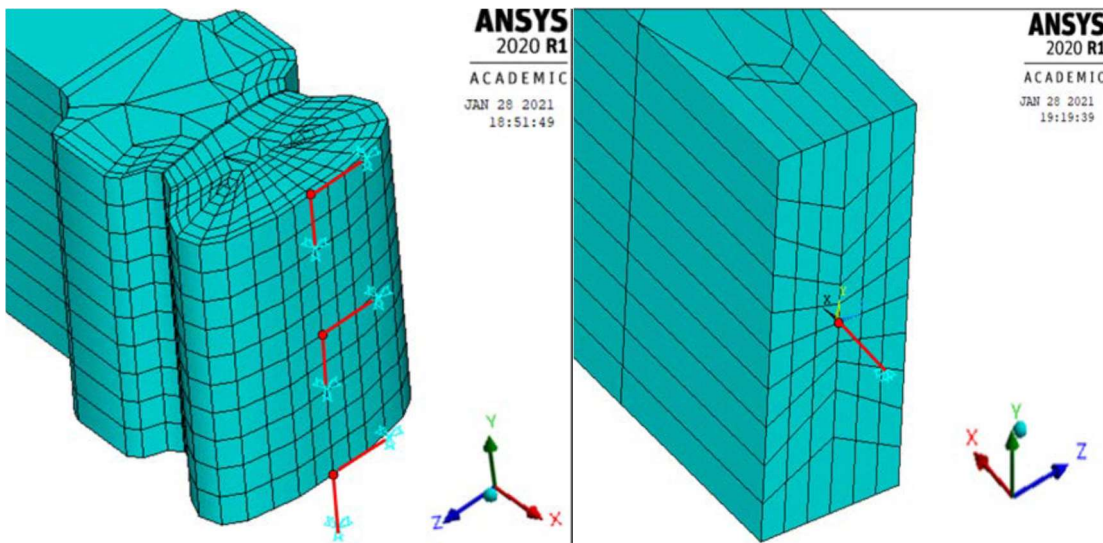


Figure 4.5: Constraints by elastic supports on specific nodes for static analysis

To verify that the assigned constraints did not affect the dynamic behavior of the beam, a comparison between the frequencies of a free beam with the constrained beam with elastic supports was made. The results in Table 4.1 show no stiffening effect due to the applied constraints.

Table 4.1: Comparison between the frequencies [Hz] of a free beam with the constrained beam with elastic supports

Mode	Free beam frequency[Hz]	Beam with Elastic Support frequency[Hz]
1	0	0
2	0	0
3	0	0
4	0	0.15
5	0	1.09
6	0	1.11
7	476.75	476.76
8	1162.9	1162.9
9	1284.6	1284.6
10	2613.6	2613.6
11	2869.3	2869.3
12	3154.8	3154.8

### 4.3.1 Stiffening effect on beam

For each associated static analysis to the assigned axial force, to check the effect of the additional stiffness matrix  $\Delta K_F$ , a linear modal analysis was carried out using equation (4.1). An increase in the value of frequencies was found with increasing axial force, such as predicted by theoretical models [30]. Stiffening effect of axial force on the beam is shown in Table 4.2 and Figure 4.6.

F [N]		1	5000	10000	15000	20000	25000	30000
Mode		f [Hz]						
X	1	0.0	0.0	0.0	0.0	0.0	0.0	0.0
Y	2	0.1	0.1	0.1	0.1	0.1	0.1	0.1
Z	3	0.1	0.1	0.1	0.1	0.1	0.1	0.1
Rx	4	0.1	0.1	0.1	0.1	0.1	0.1	0.1
Ry	5	1.1	74.7	105.5	129.1	149.0	166.4	182.2
Rz	6	1.1	76.4	108.0	132.2	152.6	170.6	186.8
1Fy	7	476.8	498.8	519.9	540.1	559.6	578.4	596.6
1Fz	8	1162.9	1172.6	1182.3	1191.8	1201.3	1210.7	1220.0
2Fy	9	1284.6	1302.0	1319.1	1336.0	1352.7	1369.2	1385.5
3Fy	10	2613.6	2627.9	2642.1	2656.3	2670.4	2684.5	2698.4

Table 4.2: Stiffening effect of axial force on the beam

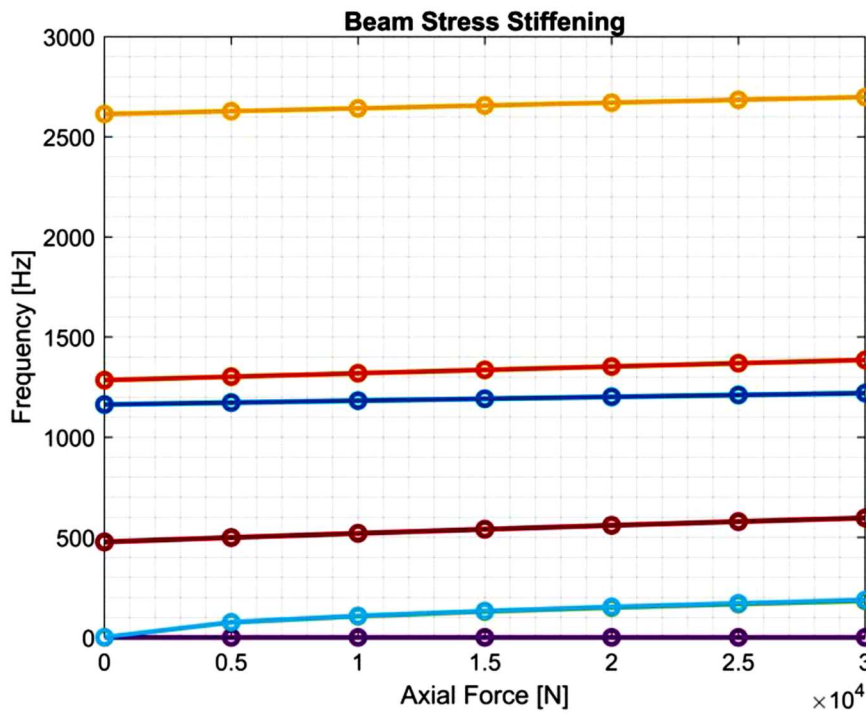


Figure 4.6: Stiffening effect of axial force on the beam



### 4.3.2 Stiffening effect on Slots

In a preliminary analysis, the stiffening effect was also introduced for the slots. For this analysis, the nodes at the base of the supports were constrained, and a force was applied on the contact surfaces, Figure 4.7. As shown in Figure 4.8, the stiffening effect was found negligible. Therefore, the supports model can be considered in further analysis without loads or constraints.

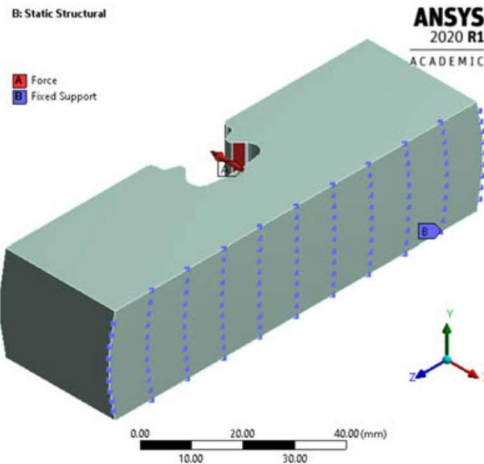


Figure 4.7: Load and constraints on slots to investigate the stiffening effect

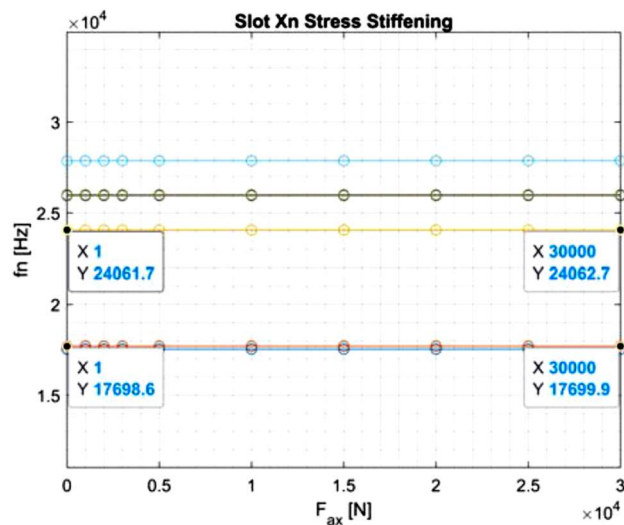


Figure 4.8: Negligible stiffening effect on slots

### 4.4 CMS reduction of the model

To identify the stiffness values by comparing F.E. frequencies with experimental measurements, a global search method varying  $k_n$ ,  $k_t$  is considered. So, many modal analyzes should be carried out to this purpose. To reduce the computation cost, it was decided to preliminarily reduce the degrees of freedom of beam and support models with a procedure belonging to the Component Mode Synthesis proposed by Craig-Bampton [35].

In this method, a change of coordinates of the motion equations should be implemented. The first step is to break down the degrees of freedom of the model into "master D.O.F.s" - which will be also present in the final reduced model - and "slave D.O.F.s". Given the system of equations of the motion as below:

$$[M]\{\ddot{u}\} + [K]\{u\} = \{0\} \quad (4.3)$$

The following partitioning can be considered:

$$\{u\} = \begin{Bmatrix} u_m \\ u_s \end{Bmatrix} \quad [M] = \begin{bmatrix} M_{mm} & 0 \\ 0 & M_{ss} \end{bmatrix} \quad [K] = \begin{bmatrix} K_{mm} & K_{ms} \\ K_{sm} & K_{ss} \end{bmatrix} \quad (4.4)$$

Defining the "Static Modes"  $[\Phi_C]$  as the displacements of the "slave D.O.F.s" due to the displacements of "Master D.O.F.s," can be written as:

$$\begin{bmatrix} K_{mm} & K_{ms} \\ K_{sm} & K_{ss} \end{bmatrix} \begin{Bmatrix} u_m \\ u_s \end{Bmatrix} = \begin{Bmatrix} F_m \\ F_s \end{Bmatrix} = \begin{Bmatrix} 0 \\ 0 \end{Bmatrix} \quad \Rightarrow \quad [K_{sm}]\{u_m\} + [K_{ss}]\{u_s\} = \{0\} \\ \Rightarrow \quad \{u_s\} = \underbrace{-[K_{ss}]^{-1}[K_{sm}]\{u_m\}}_{[\Phi_C]} \quad (4.5)$$

The "Internal Modes"  $[\Phi_N]$  is defined as the structure modes when all the "master D.O.F.s" is bound:

$$\omega^2[M_{ss}][\Phi_N] = [K_{ss}][\Phi_N] \quad (4.6)$$

It is now assumed that, when all the "master D.O.F.s" is bound, the movements of the "slave D.O.F.s" can be approximated by the combination of a subset of the internal modes:

$$\{u_s\} = [\Phi_N]\{p_N\} = [\bar{\Phi}_N|\hat{\Phi}_N] \begin{Bmatrix} \bar{p}_N \\ \hat{p}_N \end{Bmatrix} \simeq [\bar{\Phi}_N]\{\bar{p}_N\} \quad (4.7)$$

A new generalized coordinate system is adopted consisting of the "master" degrees of freedom and the coordinates  $\{p_N\}$ :

$$\{p\} = \begin{Bmatrix} u_m \\ p_N \end{Bmatrix} \quad (4.8)$$

Therefore, the movements of the "slave D.O.F.s" can be written according to the new coordinates Using Static Modes and Internal Modes:

$$\{u_s\} = [\Phi_C]\{u_m\} + [\Phi_N]\{p_N\} \quad (4.9)$$

That is, the initial degrees of freedom and the new generalized coordinate system are related by transformation matrix:

$$\begin{Bmatrix} u_m \\ u_s \end{Bmatrix} = \begin{bmatrix} I & 0 \\ \bar{\Phi}_C & \bar{\Phi}_N \end{bmatrix} \begin{Bmatrix} u_m \\ \bar{p}_N \end{Bmatrix} \Rightarrow \{u\} = [\alpha]\{p\} \quad (4.10)$$

The equations of motion of the structure in the new coordinates are therefore:

$$[M]\{\ddot{u}\} + [K]\{u\} = \{0\} \Rightarrow [\alpha]^T ([M][\alpha]\{\ddot{p}\} + [K][\alpha]\{p\}) = \{0\} \Rightarrow [\bar{M}]\{\ddot{p}\} + [\bar{K}]\{p\} = \{0\} \quad (4.11)$$

So the matrices  $[M]$ ,  $[K]$  of the reduced system can be obtained as below:

$$[\bar{K}] = [\alpha]^T [K][\alpha] = \begin{bmatrix} \bar{K}_{mm} & 0 \\ 0 & \bar{K}_{NN} \end{bmatrix} \quad [\bar{M}] = [\alpha]^T [M][\alpha] = \begin{bmatrix} \bar{M}_{mm} & \bar{M}_{mN} \\ \bar{M}_{Nm} & \bar{M}_{NN} \end{bmatrix} \quad (4.12)$$

Where

$$\begin{aligned} \bar{K}_{mm} &= [K_{mm}] + [K_{ms}][\bar{\Phi}_C] \\ \bar{K}_{NN} &= [\bar{\Phi}_N]^T [K_{ss}][\bar{\Phi}_N] \\ \bar{M}_{mm} &= [M_{mm}] + [\bar{\Phi}_C]^T [M_{ss}] \\ \bar{M}_{mN} &= \bar{M}_{Nm}^T = [\bar{\Phi}_C]^T [M_{ss}][\bar{\Phi}_N] \\ \bar{M}_{NN} &= [\bar{\Phi}_N]^T [M_{ss}][\bar{\Phi}_N] \end{aligned}$$

#### 4.4.1 Choice of Master Nodes

The master nodes chosen for the beam (to which the master D.O.F.s correspond) includes:

- selected nodes for each of the four contact interfaces;
- selected nodes along the longitudinal axis of the beam, for each of the two sides to view the modal forms of the reduced model.

The following master nodes have also been chosen for each of the two supports:

- selected nodes for each of the two contact interfaces;
- selected nodes corresponding to the vertices of the support for displaying the modes;
- the nodes at the base of the support to be subsequently constrained in MATLAB

The selected nodes described above are shown in Figure 4.9.

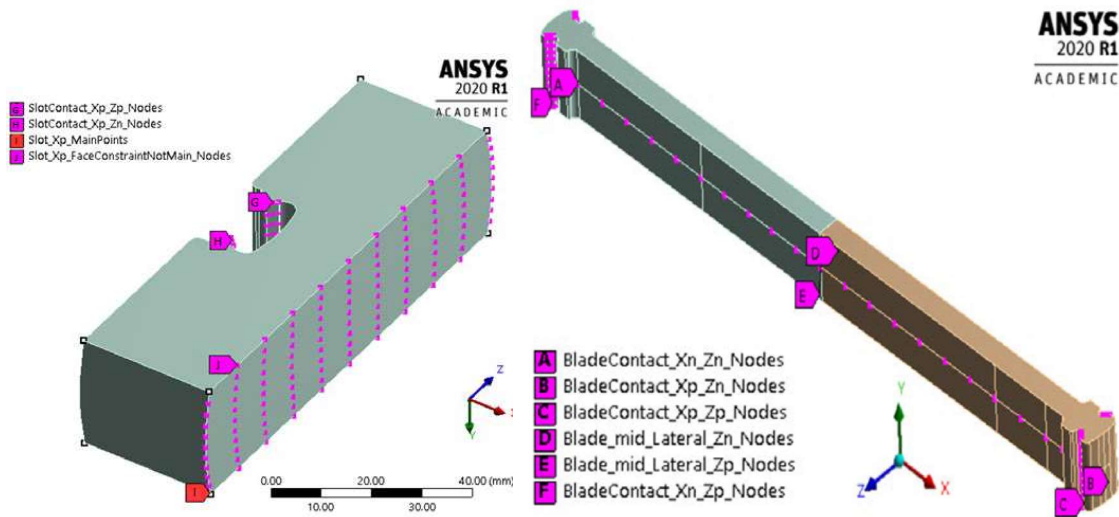


Figure 4.9: Master nodes for the reduced model

Once the master nodes were defined, the reduction of each was carried out on ANSYS® of the three models including the beam and two slots, and respectively reduced matrices  $[M]$ ,  $[K]$  have been exported.

The matrices of the reduced models were imported into MATLAB®, and the modal analysis was performed for each model (beam and the two supports). The frequencies obtained were compared with those deriving from the modal analysis of the respective non-reduced models carried out on ANSYS®. The results were obtained with a maximum percentage difference of 0.05%.

## 4.5 Resonance frequency dependence on the tensile load

In this section the numerical method is used to estimate the variation of frequency with the variation of the tensile load. The below procedure has been done and the results are shown in further figures:

- 1- Static solution with pre-stress effects calculation, Pressure applied on the contact surfaces
- 2- Modal solution including pre-stress effects, remove the pressure applied and apply different boundary conditions
  - 3-1 All nodes of contact surfaces are fixed in both normal and tangential directions
  - 3-2 All nodes fixed in normal direction

As shown in Figure 4.10, all nodes in contact surfaces were fixed in normal direction. The obtained frequencies using this assumption is shown in Table 4.3. It reflects the frictionless status.

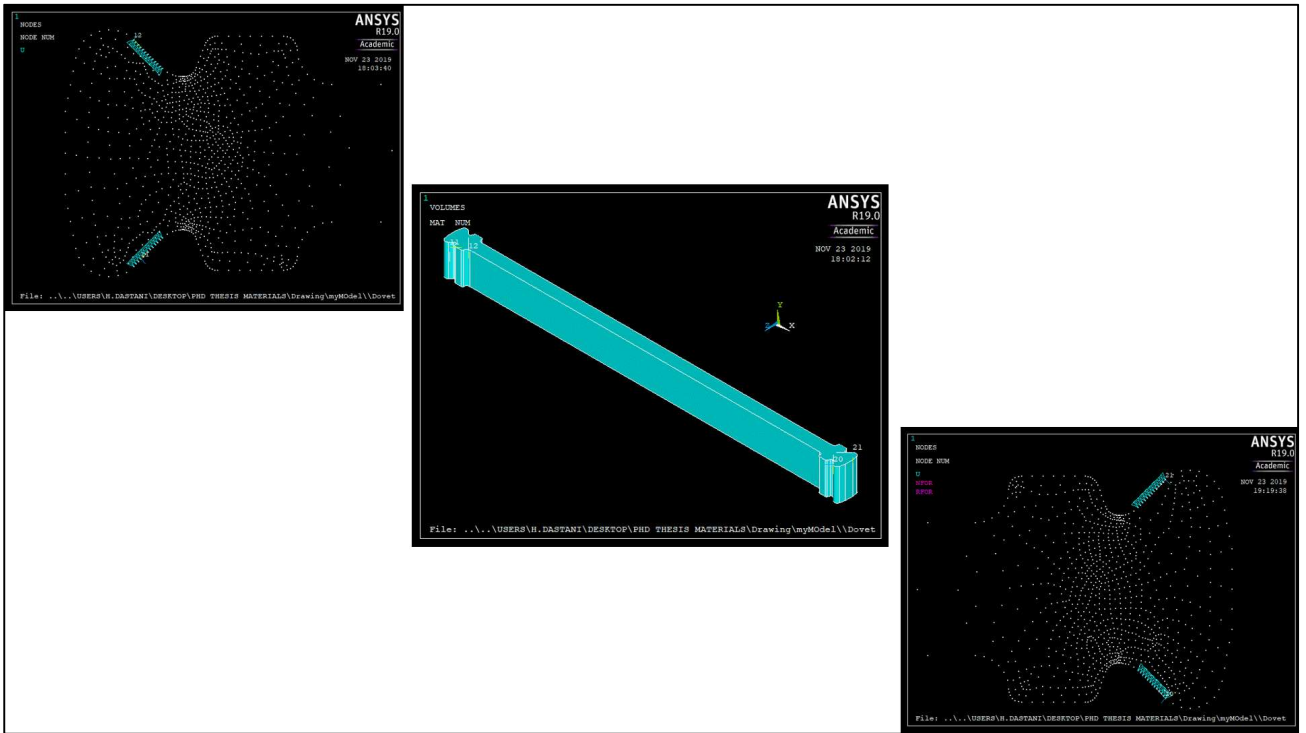


Figure 4.10: All nodes fixed in normal direction

Table 4.3: Frequency variations considering all nodes fixed in normal direction

Force, KN	first bending frequency	second bending frequency
0	519	1171
10.8	530	1193
21.6	541	1213
32.5	552	1234
43.3	562	1254
54.1	572	1274
64.9	582	1294
75.8	592	1314
86.6	601	1333

As shown in Figure 4.11, all nodes in contact surfaces were fixed in in both normal and tangential directions. The obtained frequencies using this assumption is shown in Table 4.4.

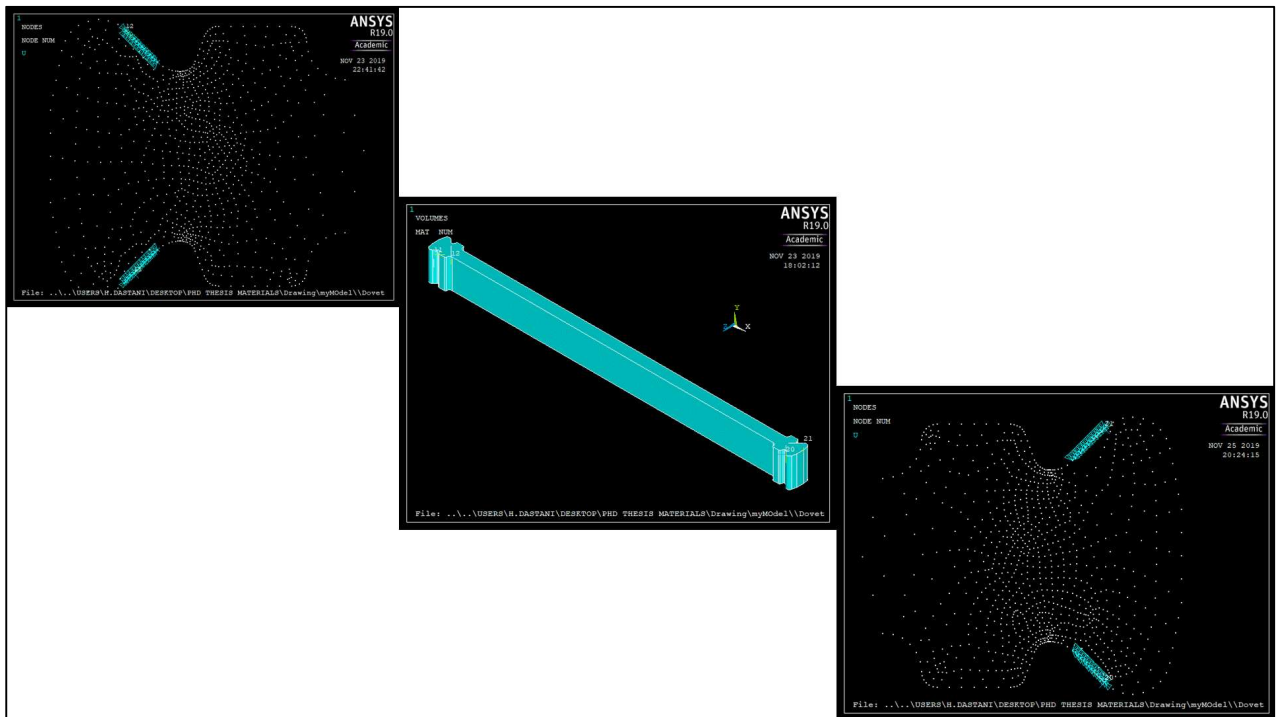


Figure 4.11: All nodes of contact surfaces fixed in both normal and tangential directions

Table 4.4: Frequency variations considering all nodes of contact surfaces fixed in both normal and tangential directions

Force, KN	first bending frequency	second bending frequency
0	562	1525
10.8	577	1547
21.6	592	1567
32.5	607	1589
43.3	622	1609
54.1	636	1629
64.9	649	1649
75.8	663	1669
86.6	676	1688

Figure 4.12 and Figure 4.13 shows the resonance frequency dependence on tensile load in first/second bending modes respectively for both constraint' assumptions.

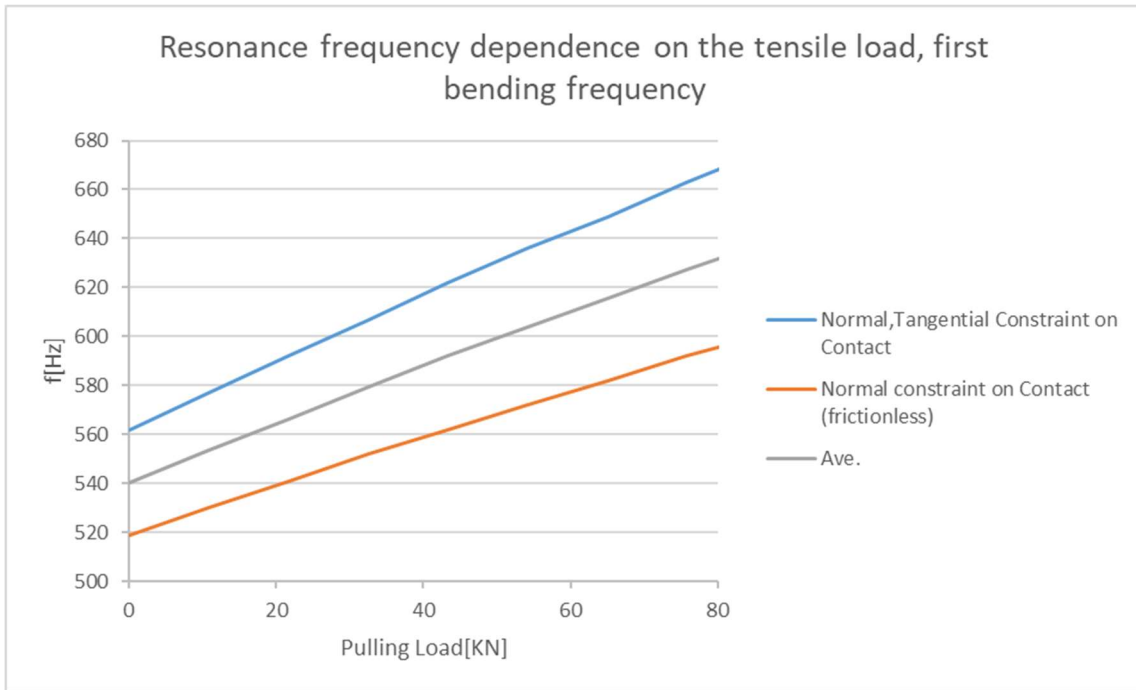


Figure 4.12: Resonance frequency dependence on tensile load, first bending mode

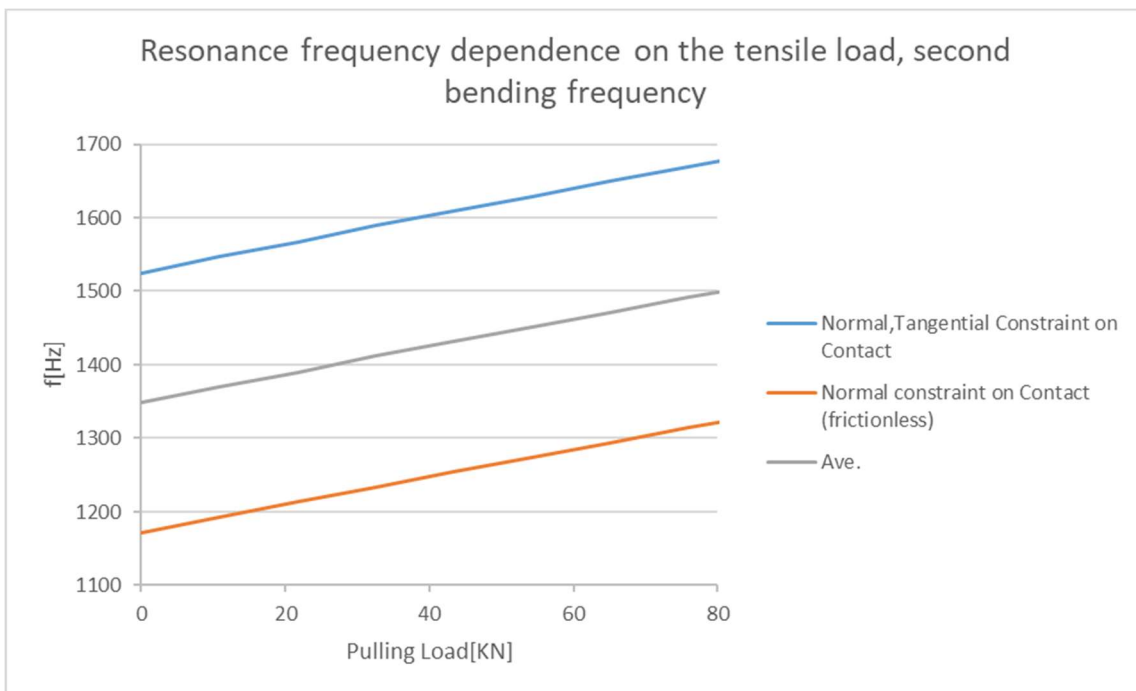


Figure 4.13: Resonance frequency dependence on tensile load, second bending mode

# Chapter 5

## Contact Stiffness Model

Contact models are essential to predict the dynamic behavior of structures that include contacts. Forces that develop at the contact surfaces may affect the structures in different ways. The non-linear behavior of the contact and the coupling between tangential and normal forces induce non-linear static and dynamic responses e.g. stick-slip oscillation, noise, chattering.

In this chapter, a contact stiffness model is described in which the  $[\bar{M}]$  and  $[\bar{K}]$  matrices of the reduced models for the beam, and two supports are used to define the global matrices  $[M_{\text{GLOB}}]$  and  $[K_{\text{GLOB}}]$  for the complete assembly, including the beam and two slots. This procedure was repeated for each matrix  $[K]_i$  of the beam, which contains the stiffening effect of the  $i$ -th axial traction force. The nodes at the base of slots were constrained, and contact elements which are defined by the parameters  $k_n$  and  $k_t$ , were added to the interfaces.

### 5.1. Definition of assembly matrices

By defining the proper nodes in contact interfaces on the blade and slots in different directions, the integration of  $[\bar{M}]$  and  $[\bar{K}]$  matrices in assembly can be indicated in Figures 5.1 and 5.2.



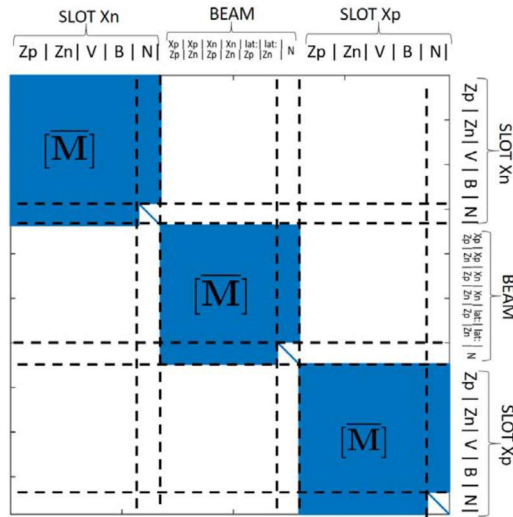


Figure 5.1: Assembly of the super element mass matrices

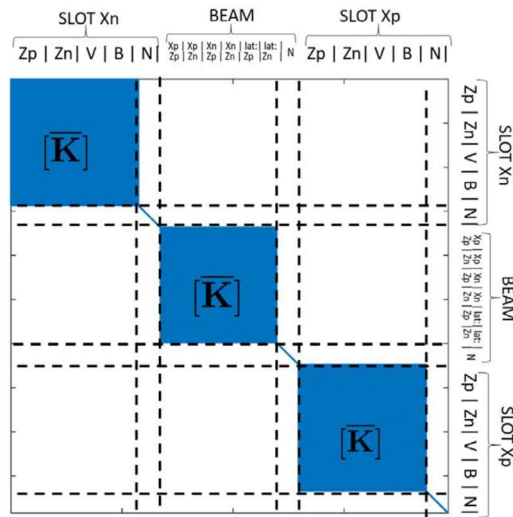


Figure 5.2: Assembly of the super element stiffness matrices

### 5.1.1 Constraints on the supports

For the subsequent modal analysis, it was necessary to constrain the nodes at the base of the supports. These nodes were previously inserted between the master nodes to possibly carry out static analysis by applying the loads on them. Target nodes at the base of the supports are shown in Figure 5.3.

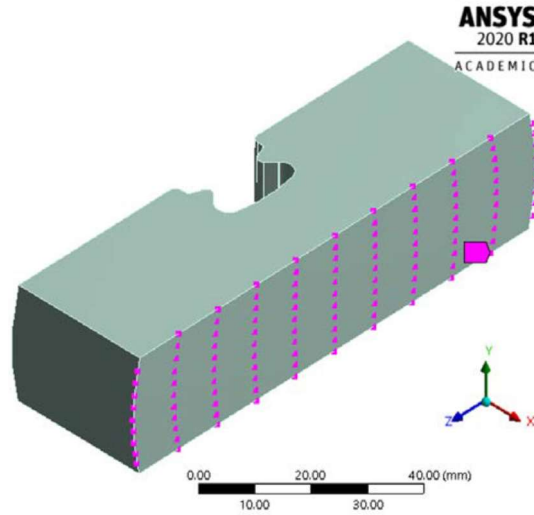


Figure 5.3: Target nodes at the base of the supports

By dividing the degrees of freedom between the effectively free (F) and the constrained ones (C), it was possible to partition the mass and stiffness matrices as below:

$$(-\omega^2[M_{GLOB}] + [K_{GLOB}]) \{ \mathbf{q} \} = \{ \mathbf{0} \} + \{ R_v \}$$

$$\left( -\omega^2 \begin{bmatrix} [M_{FF}] & [M_{FC}] \\ [M_{CF}] & [M_{CC}] \end{bmatrix} + \begin{bmatrix} [K_{FF}] & [K_{FC}] \\ [K_{CF}] & [K_{CC}] \end{bmatrix} \right) \begin{Bmatrix} \mathbf{q}_F \\ \mathbf{q}_C = \mathbf{0} \end{Bmatrix} = \begin{Bmatrix} \mathbf{0} \\ \mathbf{0} \end{Bmatrix} + \begin{Bmatrix} \mathbf{0} \\ R_v \end{Bmatrix} \quad (5.1)$$

From which

$$\left\{ \begin{array}{l} \boxed{(-\omega^2[M_{FF}] + [K_{FF}]) \{ \mathbf{q}_F \} = \{ \mathbf{0} \}} \\ (-\omega^2[M_{CF}] + [K_{CF}]) \{ \mathbf{q}_F \} = \{ R_v \} \end{array} \right. \quad (5.2)$$

Then the modal analyzes were carried out using the matrices  $[M_{FF}]$ ,  $[K_{FF}]$ , obtained from the global matrices  $[M_{GLOB}]$ ,  $[K_{GLOB}]$  by eliminating the rows and columns corresponding to the degrees of freedom of bases (B) of two supports. The structure of the resulting matrices can be seen in Figures 5.4 and 5.5.

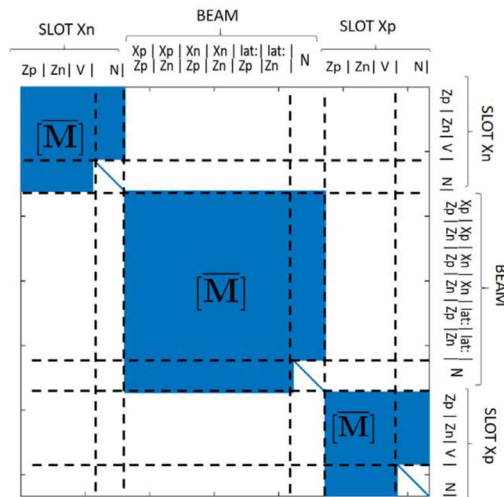


Figure 5.4: Global mass matrix after adding the constraints

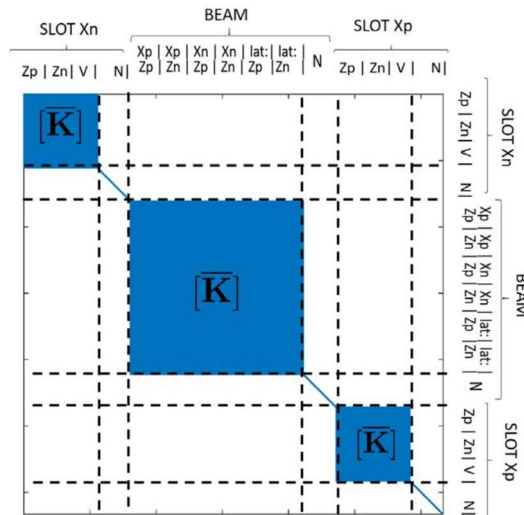


Figure 5.5: Global stiffness matrix after adding the constraints

### 5.1.2 Connectivity matrix

To insert the contact elements to the interfaces, a connectivity matrix should be defined to associate the degrees of freedom of coincident nodes of beam and supports. Each row of the connectivity matrix corresponds to a pair of coincident nodes between which a contact element should be inserted.

$$\text{CONNECTIVITY} = \begin{bmatrix} \overbrace{(\text{Xdof} \quad \text{Ydof} \quad \text{Zdof})}^{\text{Beam}} & \overbrace{(\text{Xdof} \quad \text{Ydof} \quad \text{Zdof})}^{\text{SlotXn}} \\ \vdots & \vdots \\ \overbrace{(\text{Xdof} \quad \text{Ydof} \quad \text{Zdof})}^{\text{Beam}} & \overbrace{(\text{Xdof} \quad \text{Ydof} \quad \text{Zdof})}^{\text{SlotXp}} \\ \vdots & \vdots \end{bmatrix}$$

Coincident nodes were identified by looking for nodes with the same identification number used in ANSYS. It was verified that this method is equivalent to searching for nodes having the same coordinates.

### 5.1.3 Contact Element

As shown in Figure 5.6, linear contact elements were considered which do not implement sliding nor the separation of contact. The stiffness matrix in local coordinates can be written as below:

$$K_{(e)}^L = \begin{bmatrix} k_n & 0 & 0 & -k_n & 0 & 0 \\ 0 & k_t & 0 & 0 & -k_t & 0 \\ 0 & 0 & k_t & 0 & 0 & -k_t \\ -k_n & 0 & 0 & k_n & 0 & 0 \\ 0 & -k_t & 0 & 0 & k_t & 0 \\ 0 & 0 & -k_t & 0 & 0 & k_t \end{bmatrix} \quad U^L = \begin{Bmatrix} U_{x1} \\ U_{y1} \\ U_{z1} \\ U_{x2} \\ U_{y2} \\ U_{z2} \end{Bmatrix}$$

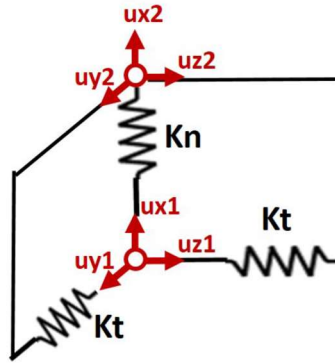


Figure 5.6: Linear contact element

### 5.1.4 Stiffness matrix in global coordinates

As the total potential energy is invariant with respect to the reference system, the rotation matrix  $[\Lambda]$  can be used to switch from the local to the global system. The rotation matrix is given by the relation:

$$\{U_{(e)}^L\} = [\Lambda_{(e)}^L] \{U_{(e)}^G\}$$

$$\left. \begin{aligned} U_P &= \frac{1}{2} \{U_{(e)}^G\}^T [K_{(e)}^G] \{U_{(e)}^G\} \\ U_P &= \frac{1}{2} \{U_{(e)}^L\}^T [K_{(e)}^L] \{U_{(e)}^L\} = \frac{1}{2} ([\Lambda_{(e)}] \{U^G\})^T \cdot [K_{(e)}^L] \cdot ([\Lambda_{(e)}] \{U^G\}) = \frac{1}{2} \{U^G\}^T ([\Lambda_{(e)}]^T [K_{(e)}^L] [\Lambda_{(e)}]) \cdot \{U^G\} \end{aligned} \right\}$$

$$\Rightarrow [K_{(e)}^G] = [\Lambda_{(e)}]^T [K_{(e)}^L] [\Lambda_{(e)}]$$

(5.3)

Where the rotation matrix is given by the relation

$$\{U^L\} = \begin{Bmatrix} U_{x1}^L \\ U_{y1}^L \\ U_{z1}^L \\ U_{x2}^L \\ U_{y2}^L \\ U_{z2}^L \end{Bmatrix} = [\Lambda_{(e)}^L] \{U_{(e)}^G\} = \begin{bmatrix} c & 0 & s & 0 & 0 & 0 \\ 0 & 1 & 0 & 0 & 0 & 0 \\ -s & 0 & c & 0 & 0 & 0 \\ 0 & 0 & 0 & c & 0 & s \\ 0 & 0 & 0 & 0 & 1 & 0 \\ 0 & 0 & 0 & -s & 0 & c \end{bmatrix} \begin{Bmatrix} U_{x1}^G \\ U_{y1}^G \\ U_{z1}^G \\ U_{x2}^G \\ U_{y2}^G \\ U_{z2}^G \end{Bmatrix}$$

With  $\begin{cases} c := \cos\theta \\ s := \sin\theta \end{cases}$

Rotation state of the coordinates of the contact elements is shown in Figure 5.7.

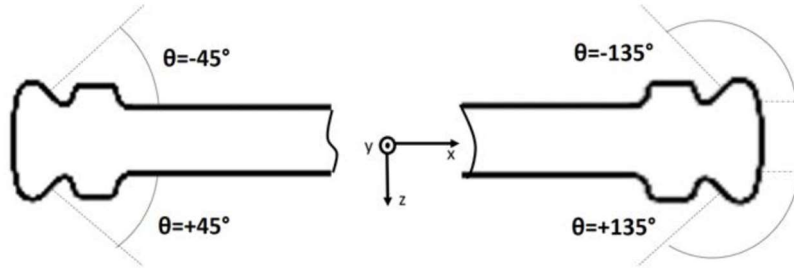


Figure 5.7: Rotation of the coordinates of the contact elements

For the assembly of the contact elements, a contact element was then inserted for each pair of coincident nodes by adding the element matrix in global coordinates  $[K_{(e)}^G]$  to the global matrix of the assembly  $[(K_{GLOB})_{FF}]$ . The assembly procedure can be verified by the structure of the resulting global matrix, shown in Figure 5.8.

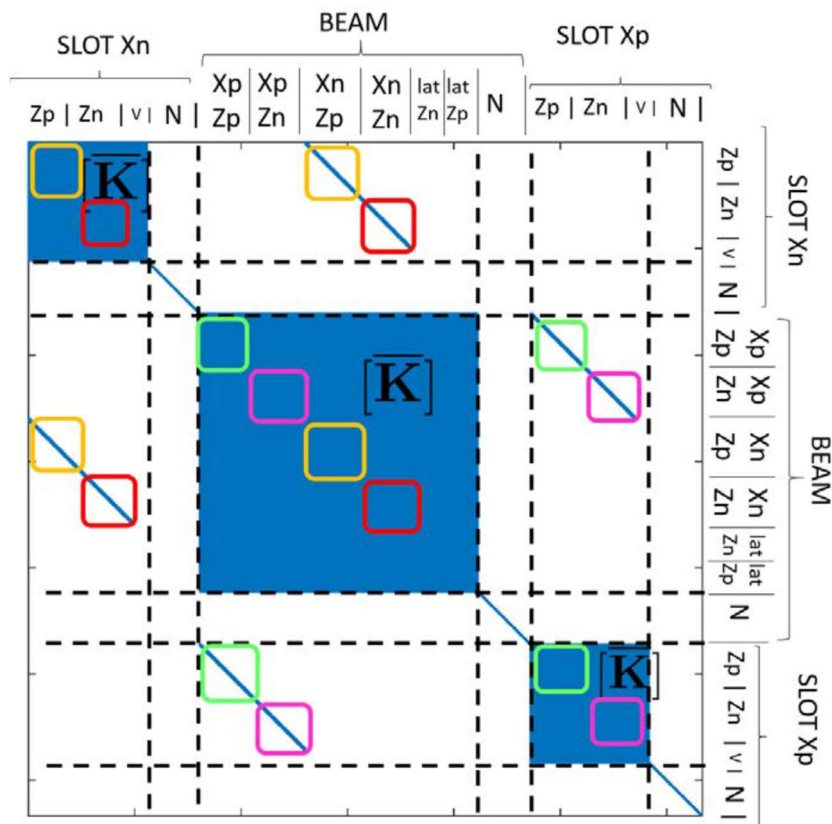


Figure 5.8: Assembly of the contact elements

## 5.2 Search of the $k_n$ and $k_t$

The global matrix  $[(K_{\text{GLOB}})_{\text{FF}}]$  depends on the values of parameters  $k_n$ ,  $k_t$ , which is the object of the present research. The frequencies were compared to obtain an estimate of these F.E. values with the measured frequencies, for the first and second flexural modes, for each axial traction force.

The F.E. model has contact elements that do not implement sliding or separation. Therefore, for each axial force  $F_{\text{ax}}$ , there is a linear model. To compare the natural frequencies of this model with those measured, it was necessary to extract the frequencies obtained during the complete adhesion of contact regions from the measurements.

By analyzing the curves  $f_n(A)$  obtained from the measurements for each axial force, the frequency in which  $f_{\text{stick}}$  has a constant trend has been selected. It is an index of complete contact adhesion and linearity of system for that range of vibration amplitudes (Figure 5.9).

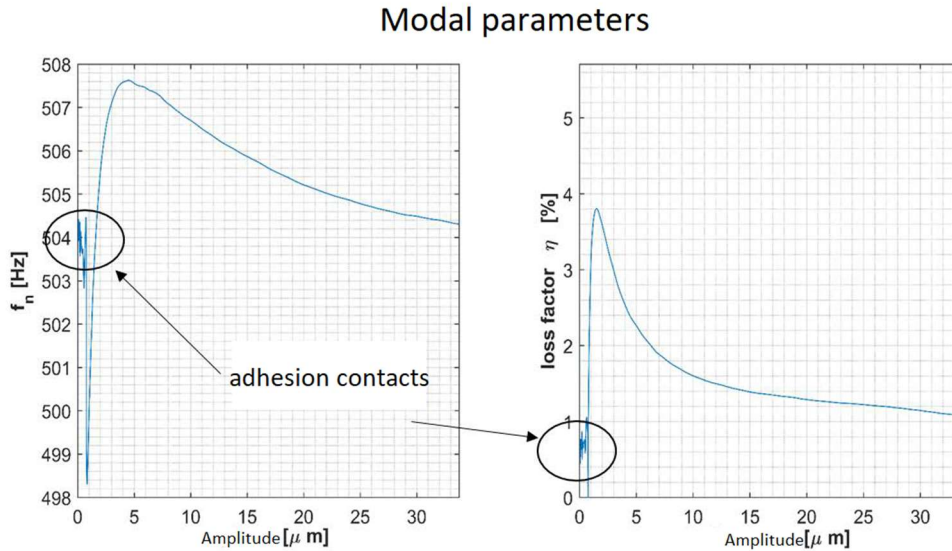


Figure 5.9: Selection of frequencies in complete adhesion status of the contacts

Figure 5.10 shows the extracted values of frequencies with respect to the relevant axial force. These curves were compared with the theoretical ones obtained from the Euler-Bernoulli beam model, which has been modified to consider the stiffening effect of the traction force [30].

For low traction values, the deviation of measured frequencies from the theoretical linear trend is attributable to the micro slip of contacts. So, for further analyses, the axial forces greater than 12kN is considered to provide the linear behavior in complete adhesion status.

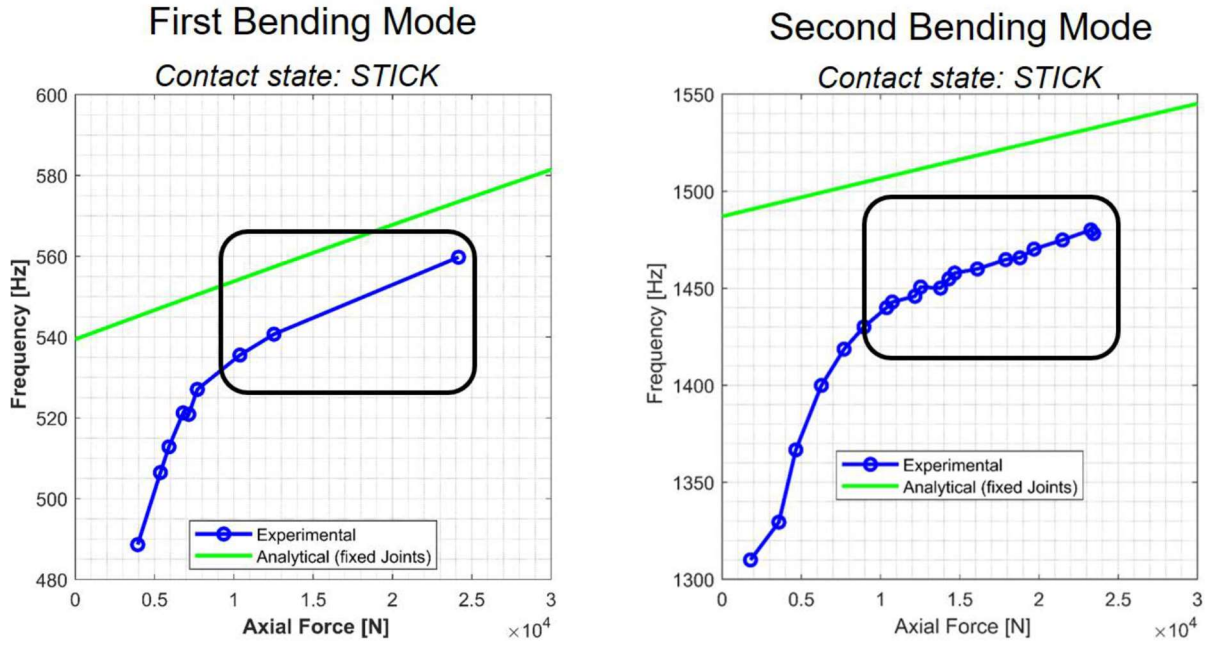


Figure 5.10: Selection of  $f_{stick}$ , frequencies for  $F_{ax} > 12kN$

### 5.2.1 Nonlinearity behavior of the system

For each axial traction force, the frequencies of the linear F.E. model were obtained from the classical linear modal analysis. Considering the global matrices as  $[M] = [(M_{GLOB})_{FF}]$ ,  $[K] = [(K_{GLOB})_{FF}]$ , the general equation can be written  $\forall F_{ax}$  i-th as below:

$$[M]\{\ddot{\mathbf{q}}(t)\} + [K_i(k_n, k_t)]\{\mathbf{q}(t)\} = \mathbf{0} \quad (5.4)$$

the linear solution is the harmonic type:

$$\{\mathbf{q}(t)\} = \{\bar{\mathbf{q}}\}e^{i\omega t} \Rightarrow (-\omega^2 M + K_i)\{\bar{\mathbf{q}}\} = \mathbf{0} \quad (5.5)$$

Excluding the trivial solution  $\{\mathbf{q}\} = 0$ , the other possible solutions (eigenvectors) are obtained for those values of  $\omega^2$  (eigenvalues of the generalized problem) for which the matrix  $(-\omega^2 M + K)$  is not invertible. This condition is verified when:

$$\det(-\omega^2 M + K_i(k_n, k_t)) = 0 \quad \forall F_i \quad (5.6)$$

which the roots  $\omega_{n,i}^2$  are the eigenvalues:

$$\sum_{j=0}^{Ndof} a_j(k_n, k_t) \cdot (\omega_{n,i}^2)^j = 0 \quad \forall F_i$$

The natural vibration frequency  $\omega_n = 2\pi f_n$  of each mode depends on the coefficients  $a_j$  of the polynomial characteristic, which refers to the nonlinear functions of the stiffness parameters  $k_n, k_t$ . So the frequencies depend non-linearly on  $k_n, k_t$  which  $f_{n(FEM)} = f_{n(k_n, k_t)}$  as shown in Figure 5.11

For the comparison:

$$(f_n)_{MEASURES} - (f_{n,i})_{FEM}(k_n, k_t) = 0 \quad \forall F_i \quad (5.7)$$

In the equation (5.7),  $n$  represents 1B for the First Bending Mode and 2B for the Second Bending Mode. It requires an iterative local method or a global one to find the solution of  $(k_n, k_t)$

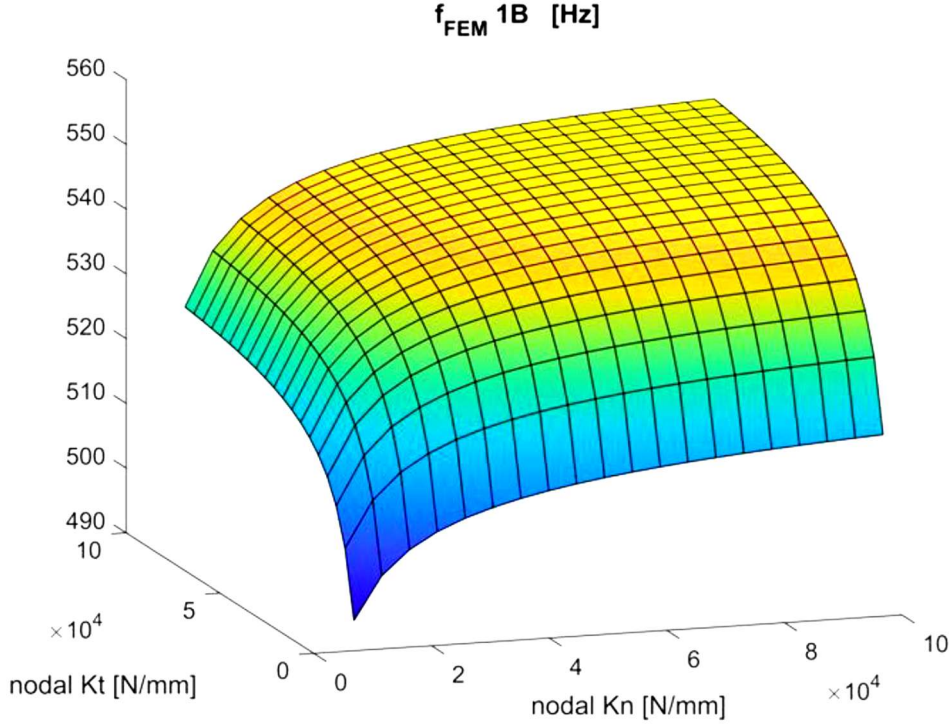


Figure 5.11: Example of nonlinear dependence of the frequency on  $k_n, k_t$

### 5.2.2 Determination of $(k_n, k_t)$ for each axial force

As there are two unknowns of the problem ( $k_n, k_t$ ), it was necessary to consider at least two equations to obtain a solution. So, the solution ( $k_n, k_t$ ) for each  $i$ -th axial force is considered, imposing the comparison between the measured frequencies and those of the F.E. model for the first and second flexural mode:

$$\begin{cases} (f_{1B})_{FEM}(k_n, k_t) - (f_{1B})_{MISURES} = 0 \\ (f_{2B})_{FEM}(k_n, k_t) - (f_{2B})_{MISURES} = 0 \end{cases} \quad \forall F_i \quad (5.8)$$

Which can be written in vector form as:

$$\{\Delta f\} = \begin{Bmatrix} (\Delta f)_{1B}(k_n, k_t) \\ (\Delta f)_{2B}(k_n, k_t) \end{Bmatrix} = \begin{Bmatrix} 0 \\ 0 \end{Bmatrix} \quad (5.9)$$

To converge the above set of equations, which means  $(k_n, k_t)$  satisfy both  $(\Delta f)_{1B}$  and  $(\Delta f)_{2B}$ , the error on  $\Delta f$  due to measurement and F.E. calculations should be considered.



1B refers to first bending mode and 2B refers to second bending mode. The system of equations then becomes:

$$\{|\Delta f|\} < \delta\{\Delta f\} \quad (5.10)$$

This system was solved with a global approach on the  $(k_n, k_t)$  domain considering the below condition:

$$\|\{\Delta f\}\| < \delta \|\{\Delta f\}\|$$

Where  $\|\{\Delta f\}\|$  is the Euclidean norm of the vector  $\{\Delta f\}$  and  $\delta \|\{\Delta f\}\|$  is the norm error, calculated with the theory of error propagation, as described below. In this way, there are two variables  $(k_n, k_t)$  and a scalar value of the objective function  $\|\{\Delta f\}\|$ .

### 5.2.3 Error propagation of measurements

From the theory of error propagation, given a function  $q$  of the variables  $x_j = x_j \pm \delta x_j$ , the maximum uncertainty  $\delta q$  is given by:

$$\delta q = \sum_j \left| \frac{\partial q}{\partial x_j} \right| \delta x_j$$

$$\|\{\Delta f\}\| = \sqrt{\sum_{i=1}^N (\Delta f)_i^2} \quad (5.11)$$

In this case:

$$q = \|\{\Delta f\}\| = \sqrt{(f_{FEM} - f_{MIS})_{1B}^2 + (f_{FEM} - f_{MIS})_{2B}^2}$$

$$\delta \|\{\Delta f\}\| = \frac{1}{\|\{\Delta f\}\|} \cdot [|\Delta f|_{1B} (\delta f_{1BMIS} + \delta f_{1BFEM}) + |\Delta f|_{2B} (\delta f_{2BMIS} + \delta f_{2BFEM})] \quad (5.12)$$

Where  $\delta f_{1BMIS}$ ,  $\delta f_{2BMIS}$  are the uncertainties of measurements and  $\delta f_{1BFEM}$ ,  $\delta f_{2BFEM}$  are the errors of the F.E. model inserted to take into account the possible invalidity of the assumptions made, including the linearity of the system, or complete adhesion of contact areas. As the axial forces of each point ( $F_{ax}$ ,  $F_{MIS}$ ) of measurements and finite element calculation do not necessarily match, linear interpolation needs to be applied on the measured frequencies to estimate the frequency at the same force used in F.E. So in this interpolation process, the error of measurements can be written as below:

$$f(F) = f_1 + \frac{f_2 - f_1}{F_2 - F_1} (F - F_1) \quad (5.13)$$

Where

F = Force used in the FEM

f1, f2 = measured frequencies

F1, F2 = measured forces

Assuming independent and random errors:

$$\delta f = \sqrt{\sum_j \left( \frac{\partial f}{\partial x_j} \delta x_j \right)^2} \quad x_j = f_1, f_2, F_1, F_2 \quad (5.14)$$

Error of the measured frequencies interpolated for the F.E. forces is mentioned in the Table 5.1.

F	[kN]	12	14	16	18	20	22
$\delta f_{1BMIS}$	[Hz]	0.24	0.19	0.19	0.22	0.28	0.34
$\Delta f_{2BMIS}$	[Hz]	0.22	0.89	0.09	0.46	0.37	0.56

Table 5.1: Error of the measured frequencies interpolated for the F.E. forces

Figure 5.12 shows that the possible solutions ( $k_n$ ,  $k_t$ ) can belong to a curve with a trend similar to an equilateral hyperbola.

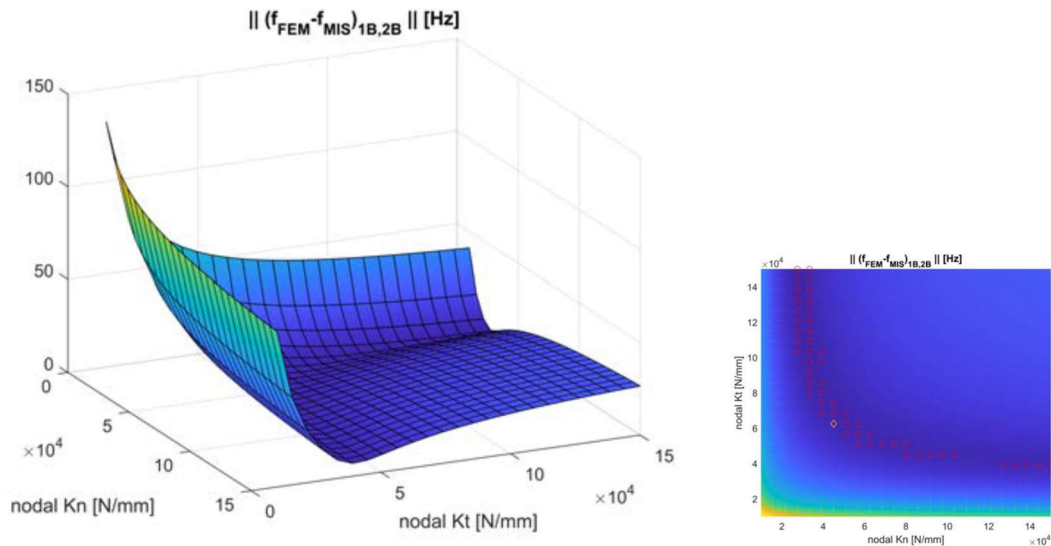


Figure 5.12: Example of solution space (red circles) - ( $F_{ax} = 12\text{kN}$ )

### 5.3 Estimation of error of $k_n$ , $k_t$ and search for the solution with minimum error

To define a single solution, the associated error with stiffness ( $k_n$ ,  $k_t$ ) of the set of solutions was estimated. The point with the least error was therefore considered as the final solution. The procedure for estimating the error is described in detail in [38]. The vector function consisting of the frequencies  $(f_{1B})_{FEM.(k_n, k_t)}$ ,  $(f_{2B})_{F.E.(k_n, k_t)}$  can be written as:

$$\mathbf{f}(k_n, k_t) = \left\{ \begin{array}{l} (f_{1B})_{FEM}(k_n, k_t) \\ (f_{2B})_{FEM}(k_n, k_t) \end{array} \right\}$$

This expression can be approximated around the solution point  $(k_n, k_t)_0$  with Taylor expansion using the Jacobian:

$$\mathbf{f} = \mathbf{f}_0 + \sum_j \left( \frac{\partial \mathbf{f}(n, \mathbf{k})}{\partial k_j} \right)_{\mathbf{k}_0} (k_j - k_{0j}) \quad (5.15)$$

$$\begin{cases} k = \begin{cases} k_n \\ k_t \end{cases} \\ k_0 \text{ is the selection point} \\ j = 1, 2 \\ n \text{ is Mode } 1B, 2B \end{cases}$$

Which in matrix form becomes:

$$\mathbf{f} = \mathbf{f}_0 + \mathbf{J}(\mathbf{k} - \mathbf{k}_0) \quad \mathbf{J} = \begin{bmatrix} \frac{\partial \mathbf{f}_{1B}}{\partial k_n} & \frac{\partial \mathbf{f}_{1B}}{\partial k_t} \\ \frac{\partial \mathbf{f}_{2B}}{\partial k_n} & \frac{\partial \mathbf{f}_{2B}}{\partial k_t} \end{bmatrix} \quad (5.16)$$

Generic error on frequency around the solution - indicated with "0" - can therefore be written as a function of generic error on stiffness:

$$\delta \mathbf{f} = \mathbf{J} \delta \mathbf{k} \quad (5.17)$$

The diagonal matrix is defined

$$[1/\sigma^2] = \begin{bmatrix} 1/\sigma_{1B}^2 & 0 \\ 0 & 1/\sigma_{2B}^2 \end{bmatrix} \quad (5.18)$$

Containing the inverse of variances means square of standard deviations of frequency measurements errors. Pre-multiplying by  $\mathbf{J}^T [1/\sigma^2]$ :

$$\mathbf{J}^T [1/\sigma^2] \delta \mathbf{f} = \mathbf{J}^T [1/\sigma^2] \mathbf{J} \cdot \delta \mathbf{k} \quad (5.19)$$

From which:

$$\delta \mathbf{k} = \mathbf{C} \mathbf{J}^T [1/\sigma^2] \cdot \delta \mathbf{f} \quad \mathbf{C} = (\mathbf{J}^T [1/\sigma^2] \mathbf{J})^{-1}$$

By indicating with  $\langle x \rangle$  the expected value of x, the covariance matrix of the stiffness in the solution point  $\mathbf{k}_0 = \{k_n, k_t\}_0$  can be calculated as follows:

$$\begin{aligned} \sigma_{\mathbf{k}}^2 &= \begin{bmatrix} \sigma_{nn}^2 & \sigma_{nt}^2 \\ \sigma_{tn}^2 & \sigma_{tt}^2 \end{bmatrix} = \langle \delta \mathbf{k} \delta \mathbf{k}^T \rangle = \langle \mathbf{C} \mathbf{J}^T [1/\sigma^2] \delta \mathbf{f} (\mathbf{C} \mathbf{J}^T [1/\sigma^2] \cdot \delta \mathbf{f})^T \rangle = \\ &= \langle \mathbf{C} \mathbf{J}^T [1/\sigma^2] \delta \mathbf{f} \delta \mathbf{f}^T [1/\sigma^2]^T \mathbf{J} \mathbf{C}^T \rangle = \\ &= \mathbf{C} \mathbf{J}^T [1/\sigma^2] \langle \delta \mathbf{f} \delta \mathbf{f}^T \rangle [1/\sigma^2] \mathbf{J} \mathbf{C}^T \end{aligned} \quad (5.20)$$

Assuming the errors  $\delta f_j$  of the statistically uncorrelated frequency measurements:

$$\langle \delta \mathbf{f} \delta \mathbf{f}^T \rangle = \begin{bmatrix} \sigma_{1B}^2 & 0 \\ 0 & \sigma_{2B}^2 \end{bmatrix} := [\sigma^2] \quad (5.21)$$

$$\sigma_{\mathbf{k}}^2 = \mathbf{C} \mathbf{J}^T [1/\sigma^2] [\sigma^2] [\mathbf{J}] \mathbf{C}^T = \mathbf{C} (\mathbf{J}^T [1/\sigma^2] \mathbf{J}) \mathbf{C}^T = \mathbf{C} \cdot \mathbf{C}^{-1} \cdot \mathbf{C}^T = \mathbf{C}^T = \mathbf{C}$$

Where the ultimate equality derives from the symmetry of matrix C. In conclusion:

$$\begin{bmatrix} \sigma_{nn}^2 & \sigma_{nt}^2 \\ \sigma_{tn}^2 & \sigma_{tt}^2 \end{bmatrix} = \sigma_{\mathbf{k}}^2 = \mathbf{C} = (\mathbf{J}^T [1/\sigma^2] \mathbf{J})^{-1} \quad \mathbf{J} = \begin{bmatrix} \frac{\partial \mathbf{f}_{1B}}{\partial k_n} & \frac{\partial \mathbf{f}_{1B}}{\partial k_t} \\ \frac{\partial \mathbf{f}_{2B}}{\partial k_n} & \frac{\partial \mathbf{f}_{2B}}{\partial k_t} \end{bmatrix} \quad [1/\sigma^2] = \begin{bmatrix} 1/\sigma_{1B}^2 & 0 \\ 0 & 1/\sigma_{2B}^2 \end{bmatrix} \quad (5.22)$$

The covariance matrix of the stiffness is obtained for each point of the set of solutions found previously. The following overall error measurement was used to find the solution with minimum error:

$$Err = \|\sigma_{\mathbf{k}}^2\|_2 \quad (5.23)$$

At the final solution point with min Err, the standard deviations of two stiffness values  $k_{n0}$ ,  $k_{t0}$  are respectively  $\sigma_{nn}$  and  $\sigma_{tt}$ . So can be written as:

$$k_n = k_{n0} \pm \sigma_{nn} \quad k_t = k_{t0} \pm \sigma_{tt} \quad (5.24)$$

An example of the point with minimum error between the set of solution points found for  $F_{ax} = 12\text{kN}$  is shown in Figure 5.13 with yellow marks. Percentage errors of  $k_n$  and  $k_t$  are also shown in Figure 5.14.

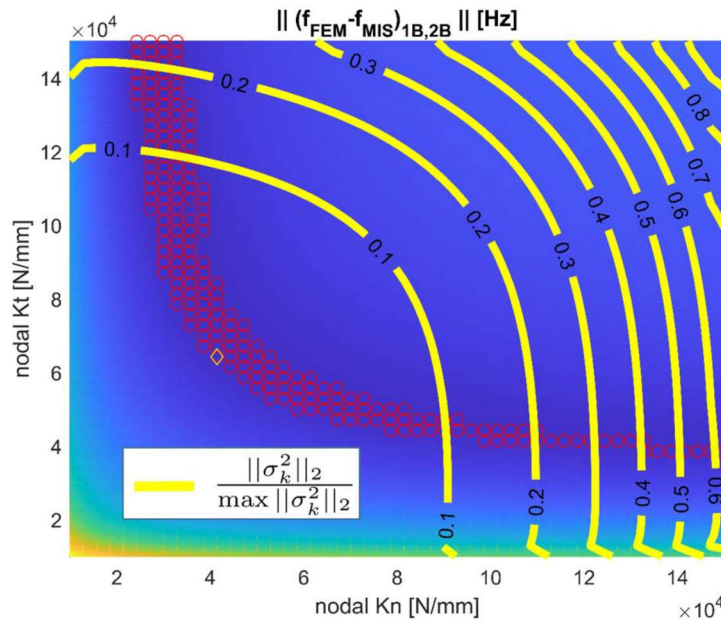


Figure 5.13: Solution ( $k_n$ ,  $k_t$ ) with minimum error ( $F_{ax}=12\text{kN}$ )

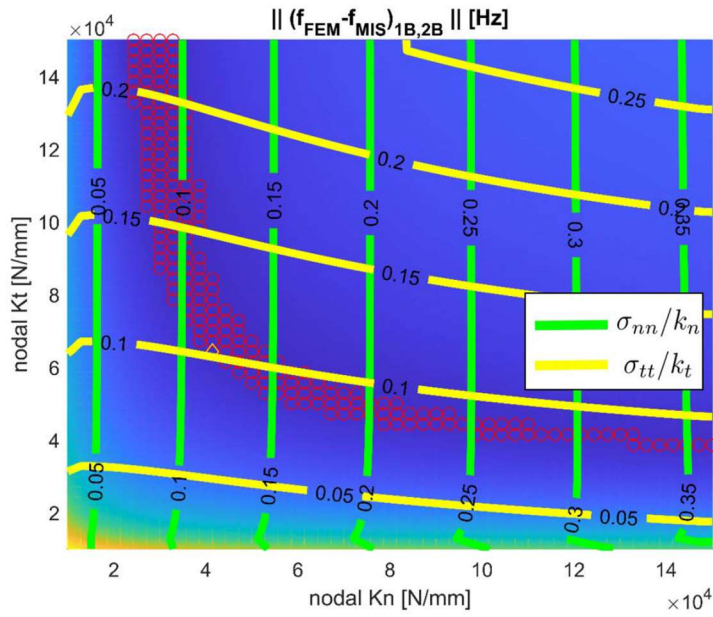


Figure 5.14: Percentage errors of  $k_n$  and  $k_t$

## 5.4 Search results for $k_n$ , $k_t$

The procedure for finding  $k_n$  and  $k_t$  described up to now was carried out for each  $i$ -th axial force of the interval visible in Figure 5.10. The results are shown in Table 5.2. Note that the found stiffness are the nodal ones. It is necessary to multiply the results by the number of nodes used for each interface to estimate the overall value of each contact region.

F [kN]	$k_n$ [N/mm]	$\delta k_n$ [N/mm]	$\delta k_n/k_n$ [%]	$k_t$ [N/mm]	$\delta k_t$ [N/mm]	$\delta k_t/k_t$ [%]
12	41428.6	4866.6	11.7%	64285.7	6587.3	10.2%
14	50000.0	10042.7	20.1%	61428.6	10822.9	17.6%
16	51000.1	5439.5	10.9%	72857.1	6550.6	9.0%
18	55714.3	9546.6	17.1%	75714.2	11395.4	15.2%
20	58571.4	11673.4	19.9%	84285.7	14891.3	17.7%
22	61428.6	16485.6	26.7%	85334.1	19768.2	23.5%

Table 5.2: Final results of the search for  $k_n$ ,  $k_t$

Normal and tangential stiffness variations considering the estimated errors is shown in Figure 5.15 and Figure 5.16 respectively.

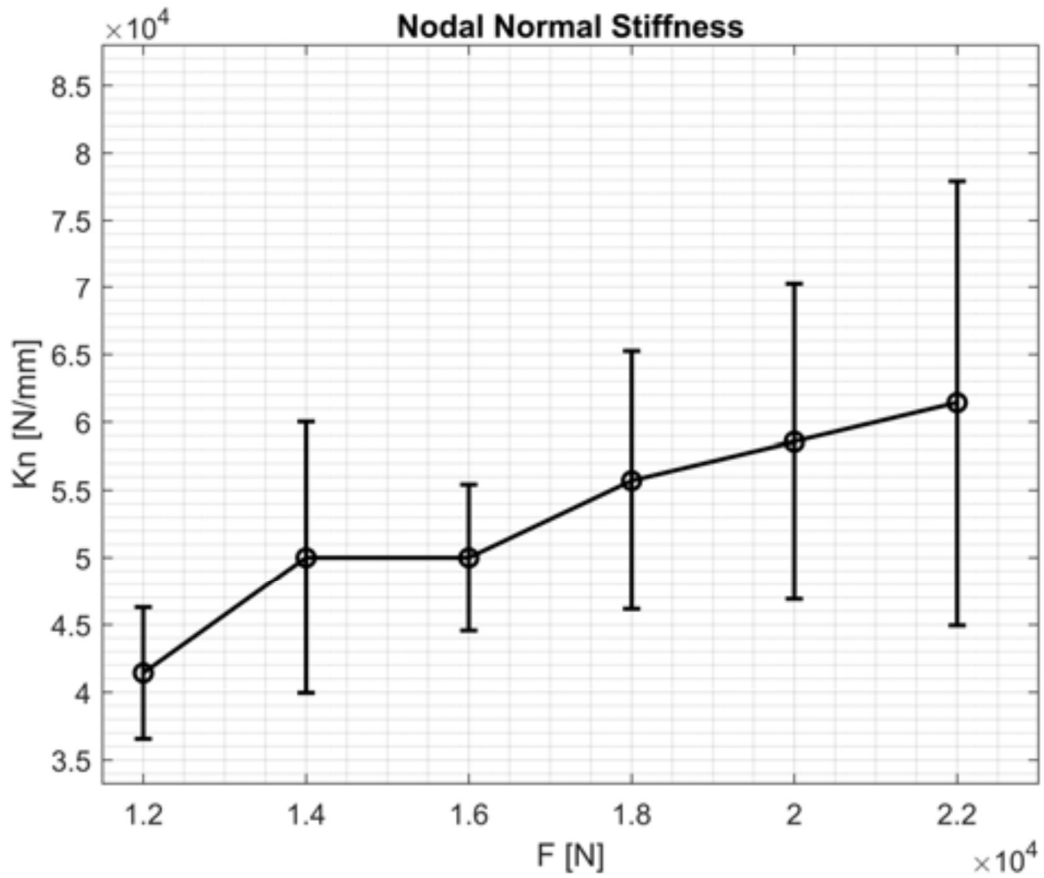


Figure 5.15: Normal stiffness variations considering the estimated errors

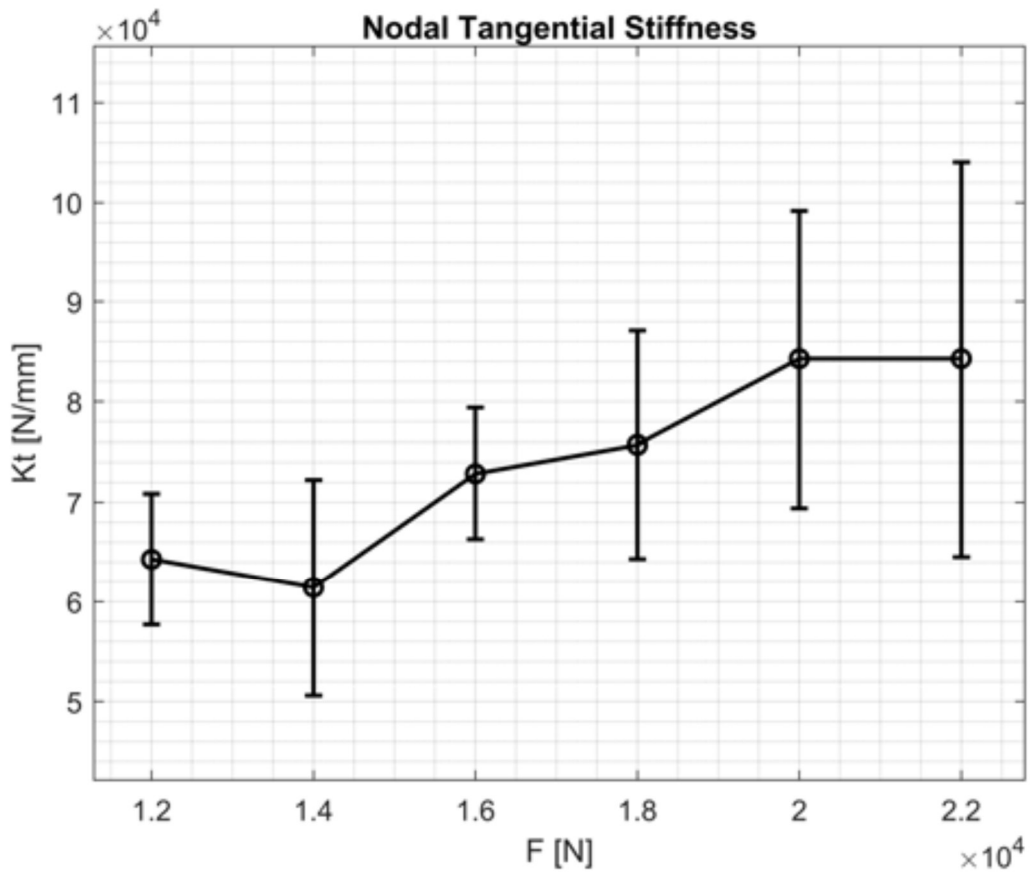


Figure 5.16: Tangential stiffness variations considering the estimated errors

The obtained stiffness are associated with the frequencies of the finite element model visible in Figure 5.17 and Figure 5.18 for both first and second bending mode in stick contact status.

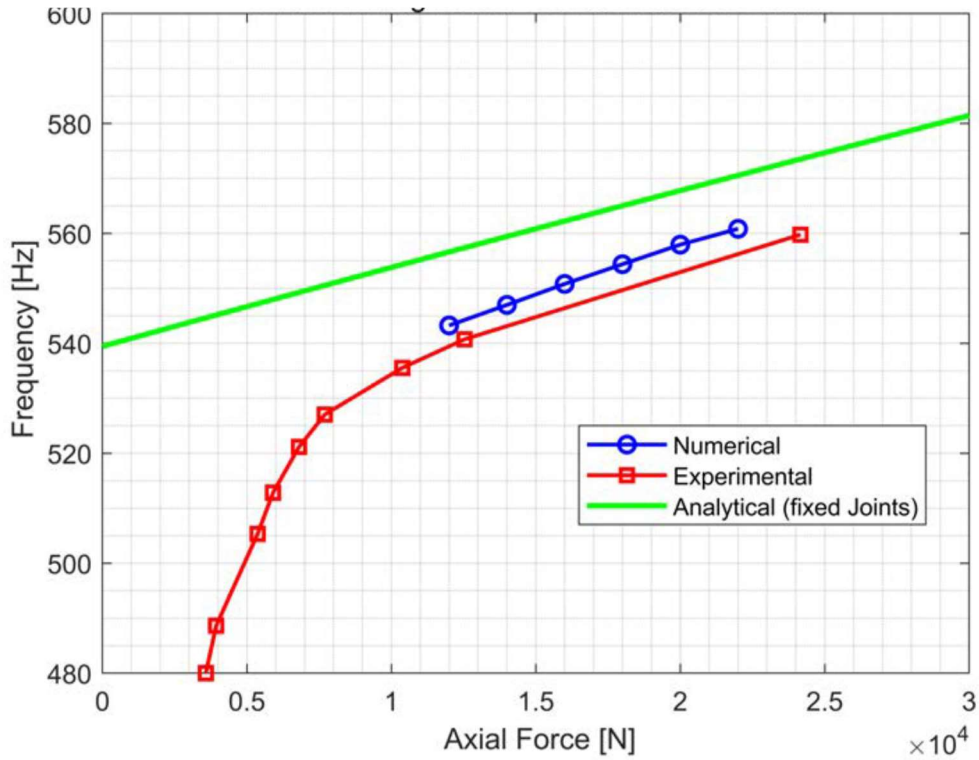


Figure 5.17: Results of the frequency comparison for the first bending mode in stick contact status

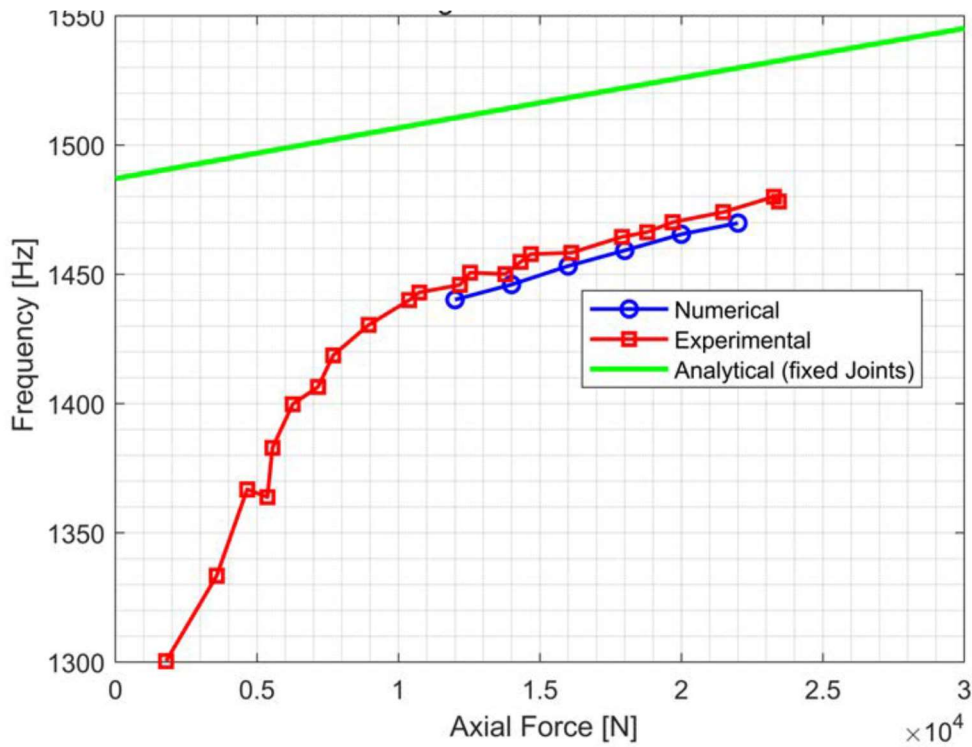


Figure 5.18: Results of the frequency comparison for the second bending mode in stick contact status

# Chapter 6

## Theoretical estimate of contact stiffness

The sliding contact between conformal surfaces was theoretically studied in [44], where a model of the indenter (Figure 6.1) with the rounded edges pressed on the flat half-space. It is extended to the three-dimensional case, and displacements are calculated using the potential theory developed by Cerruti and Bussinesq [43, 45].

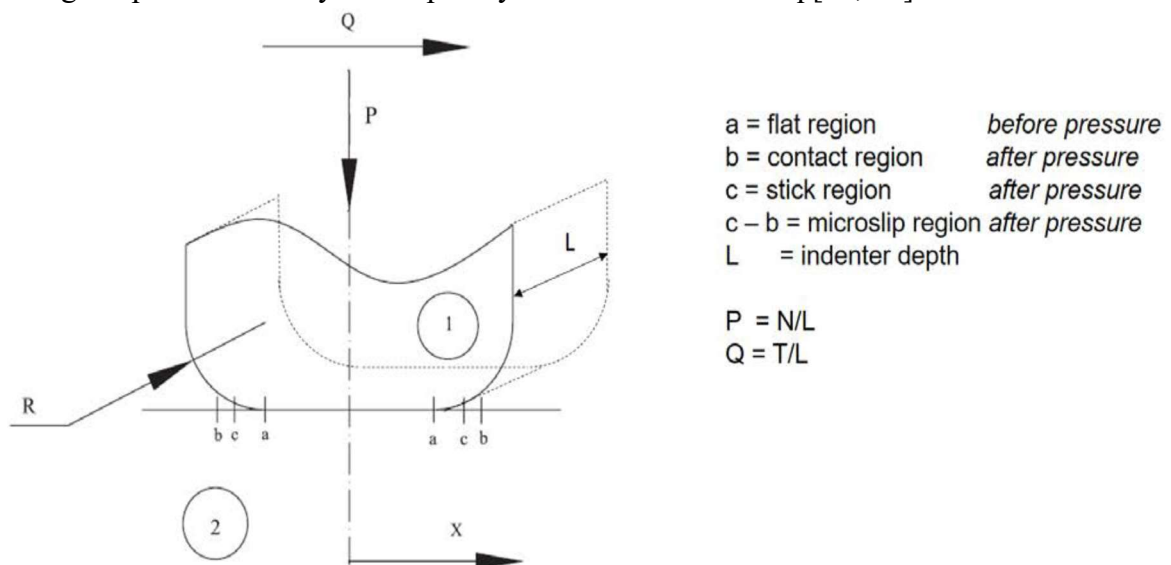


Figure 6.1: Model of the indenter (1) on the flat half-space (2) [44]



## 6.1 Contact Model

The analytical model developed to evaluate the hysteresis cycles at the contact is based on a number of hypothesis to permit to solve the analytical problem and obtain a solution suitable for the implementation on the forced response calculation of bladed disk with contact interfaces. The below items are considered to this purpose:

- The material of two bodies is perfectly elastic. The elastic limit is not reached in the contact areas.
- The two bodies under examination must be isotropic.
- The contacting surfaces are perfectly smooth, so that contact is continuous over a defined area. This hypothesis implies that the roughness is not considered.
- The complex geometry of the blade root under study is transformed into an analogue contact problem. Interaction between the dovetail segment of the blade and attachment slot of the disk, can be modelled by the contact of an indenter with flat base and the rounded edges on a half space, i.e. semi-infinite bodies with infinitely remote boundaries. The half plane (or half space) idealization is certainly justified when the ratio between the half width of the contact area and the radius of curvature,  $a/R$ , is small. Actually the outer parts of the indenter will support the contact area in the same way as for the Hertzian case. As the contact patch extends further into the curved region the half plane assumption becomes poorer and the overall geometry becomes increasingly more important. The real model of dovetail and load applied at 2D state is shown in Figure 6.2.

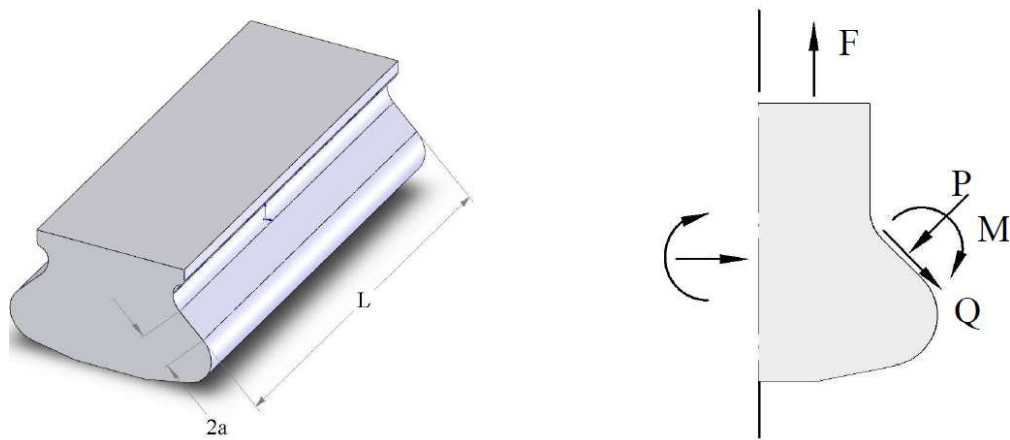


Figure 6.2: On the left real dovetail geometry, on the right load applied at 2D problem.

These first hypothesis are basically the same proposed by Hertz to solve the problem of spheres in contact.

- Amonton's law of friction with constant coefficient of friction , this hypothesis considers:

$$|q(x, y)| \leq \mu |p(x, y)| \quad (6.1)$$

in the stick region and

$$|q(x, y)| = \mu |p(x, y)| \quad (6.2)$$

in the slip region.

- Constant normal load at the contact. In dovetail joint, if the centrifugal load is kipped constant, the forces induced by vibrations can change both normal and tangential load at the interface of blade to disc. It is assumed in this study that the variation of normal load due to vibrations is negligible in comparison with the constant normal load generated by centrifugal force.
- Normal pressure distributions and shear traction distributions are obtained under the hypothesis of 2D contact problem. The length of the joint,  $L$ , in comparison with the contact area,  $2a$ , justifies this hypothesis. Obviously the real contact is three-dimensional and therefore demands theoretically a three dimensional solution. But few solutions are known in three dimensional theory, typically for axis-symmetric problems, therefore it is often better to approximate the geometry in 2D state. So, the plain strain hypothesis is applied [35].

By means of these hypothesis the distributions of pressure and shear traction on the contact surfaces are known [35, 36]. To obtain the relation between the displacement of a point distant from the contact area and the tangential load it is, however, necessary abandoning the 2D contact hypothesis. Actually in 2D contact problems the absolute displacement depends on an arbitrary constant that can be found only by choosing a datum depth at which the displacement are assumed to vanish. However, by taking the datum depth deeper and deeper the displacements increase without limit.

The approach here proposed uses the Cerruti potential equations for 3D general contact problem with the pressure and tangential traction distributions obtained for a 2D contact problem kept constant in  $L$  dimension. An analogous approach was utilized to evaluate the normal deformation of cylinders in contact [37]. This method involves to neglect the edge effect. Indeed, if an indenter of finite length is pressed normally onto the surface of an elastic half plane, a more severe stress occurs at the ends. This problem may be avoided by barreling the indenter in the  $L$  direction to achieve constant distributions of normal pressure and shear traction distributions in the transverse direction. The normal-pressure distribution on the 3D half-plane is shown in Figure 6.3.

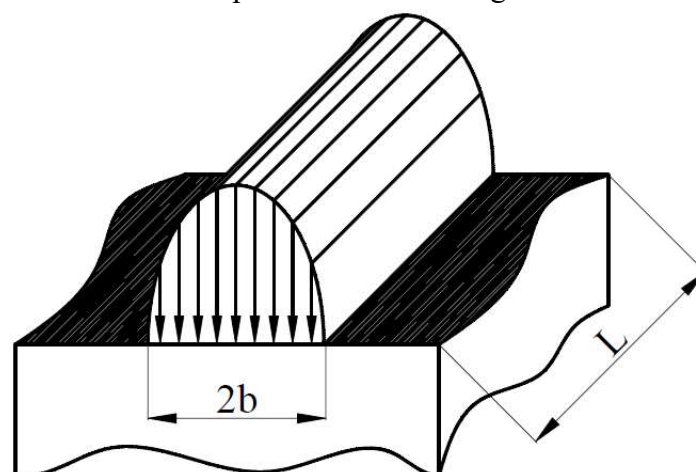


Figure 6.3. Normal-pressure distribution on the 3D half-plane.

The distribution is obtained by assuming in the narrow dimension ( $2b$ ) the solution of the 2D contact problem and keeping it constant in the length of the contact ( $L$ ). The

edge effects are neglected. The same methodology is utilized for the shear traction distribution.

## 6.2 2D pressure and shear traction distributions

The contact problem for indentation by a flat punch with rounded edges in this section reported. The solution for a flat punch with rounded edges was performed by Ciavarella et al [35]. Previous works about this geometry were published by Goodier and Loutzenheiser [38], Galin [39] and Steurman [40]. The geometry studied is shown in Fig. 5.5. The shape of the flat indenter with rounded edges is described by the function (6.3):

$$h(x) = \begin{cases} \frac{(x+a)^2}{2R} & \text{if } -b \leq x \leq -a \\ 0 & \text{if } -a \leq x \leq a \\ \frac{(x-a)^2}{2R} & \text{if } a \leq x \leq b \end{cases} \quad (6.3)$$

Where 'a' is the semi-width of the straight part of the punch and R is the edge radius. The elastic punch is pressed against an elastic half-plane. In general the two bodies can be elastically dissimilar.

However the solution is exact only for elastically similar bodies. In this case shearing tractions induce equal and opposite vertical displacement in each body, so the contact pressure distribution is unmodified. Differently for dissimilar elastic bodies coupling occurs and the pressure distribution is affected by shearing tractions. However this effect is shown to be usually negligible ([41,42]).

Under the hypothesis reported in the previous paragraph the pressure and shear traction distribution are found. The normal pressure distribution is provided by the following equations:

$$\frac{bp(\varphi)}{P} = \frac{2/\pi}{\pi - 2\varphi_0 - \sin 2\varphi_0} \left\{ (\pi - 2\varphi_0) \cos(\varphi) + \ln \left[ \frac{|\sin(\varphi + \varphi_0)|^{\sin \varphi}}{|\sin(\varphi - \varphi_0)|} \cdot \left| \tan \frac{\varphi + \varphi_0}{2} \tan \frac{\varphi - \varphi_0}{2} \right|^{\sin \varphi_0} \right] \right\} \quad (6.4)$$

Where

$$\sin(\varphi) = \frac{x}{b}$$

and b is half-width of the contact area. The angle  $\varphi_0$ , and therefore the size of the contact area, may be found using the following implicit equation

$$\frac{4PR}{a^2 E^*} = \frac{\pi - 2\varphi_0}{2 \sin^2 \varphi_0} - \cot(\varphi_0) = \frac{\pi - 2\varphi_0 - 2 \sin \varphi_0 \cos \varphi_0}{2 \sin^2 \varphi_0} = \frac{\pi - 2\varphi_0 - \sin 2\varphi_0}{2 \sin^2 \varphi_0} \quad (6.5)$$

Where

$$\sin(\varphi_0) = \frac{a}{b}$$

and  $E^*$  is a measure of the combination stiffness of the two bodies in contact, defined under plain strain conditions by

$$\frac{1}{E^*} = \frac{1}{E_1} (1 - \nu_1^2) + \frac{1}{E_2} (1 - \nu_2^2) \quad (6.6)$$

where  $E_i$  is the Young's modulus and  $\nu_i$  is the Poisson's ratio of body  $i$ .

The parameter

$$f = \frac{4PR}{a^2 E^*}$$

can vary from zero to infinite, varying the shape of the indenter. When  $f$  vanishes the indenter tends to a flat pad indenter with rounded edges, on the other hand if  $f$  tends to infinity the shape of the indenter tends to a cylindrical indenter. The width of the contact region  $b$  is a function of geometry ( $a, R$ ), normal load per unit of length ( $P = N / L$ ) and material ( $E, \nu \rightarrow E^*$ ). In Figure 6.4 the pressure distribution, for different ratio between tangential force and normal force is shown.

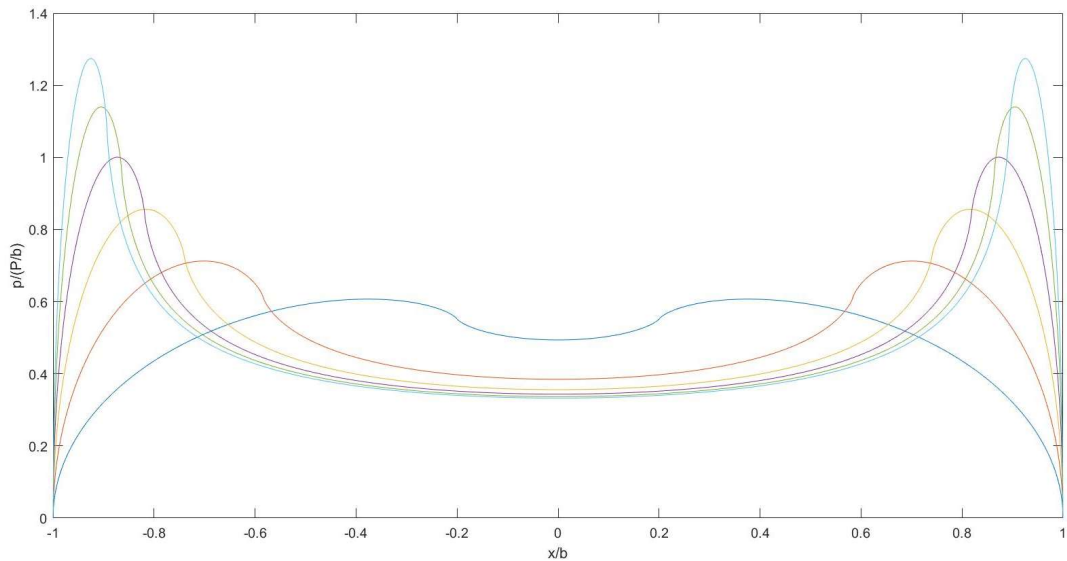


Figure 6.4: Pressure distribution, for different ratio between tangential force and normal force

In Figure 6.5 shear traction distributions for different values of the ratio between the tangential force and the normal force is shown. In [35] it is reported that in the flat part micro-slip is not permitted, i.e. the value of  $c/b$  must be always larger than  $a/b$ . This statement is true only if the punch is perfectly aligned with the half plane. If the punch is inclined the micro-slip can gradually penetrate into the flat part of the indenter, as it is reported in [36].

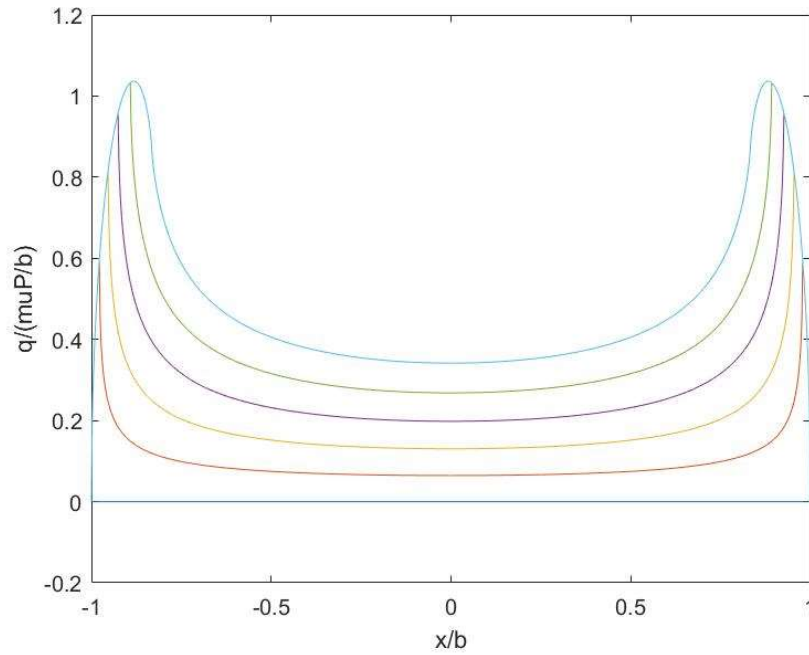


Figure 6.5: Shear distribution for different ratio between tangential force and normal force

The two-dimensional distributions of pressure and shear stress obtained above are used as a starting point to derive the displacements of three-dimensional cases.

The contact geometry of the dovetail joint under examination differs from the indenter model, as shown in Figure 6.6. To apply the theoretical model the following parameters were used:

a [mm]	2.5665/2	E [GPa]	210
R [mm]	2.50	$\nu$	0.3
L [mm]	26	$\mu$	0.42 [46]

The largest radius of curvature between  $R = 2.5\text{mm}$  and  $R = 1.25\text{mm}$  was used. To derive the contact stiffness, the values of the forces were calculated (Tangential or Normal) for the corresponding displacements obtained with the procedure described in [44].

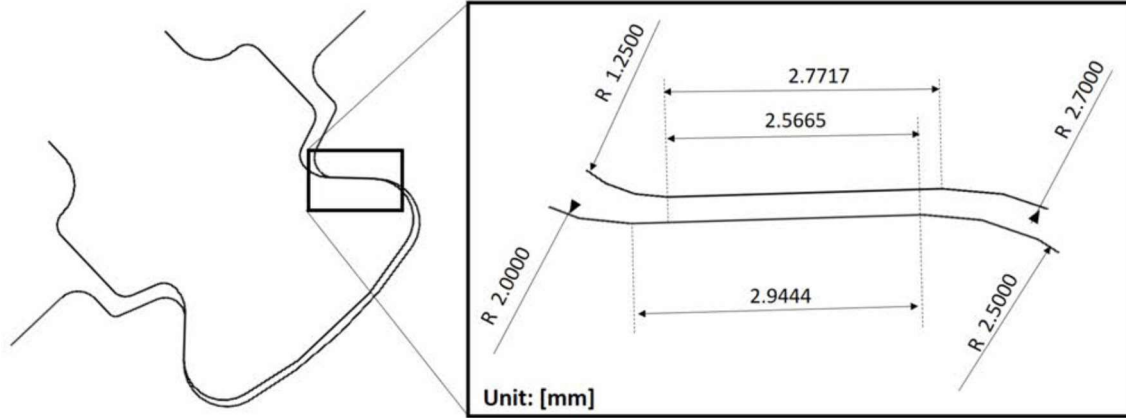


Figure 6.6: Contact geometry

The shear stress can be written as the superposition of two distributions [44], [43]:

$$q(x) = \mu p(x) - q^*(x) \quad (6.7)$$

Where  $\mu p(x)$  is the shear stress that would occur if the contact were in complete sliding and  $q^*$  can be obtained in an analogous way to  $p(x)$ . The width of the adhesion region  $c$  is also obtained through solving:

$$\sin \theta_0 = \frac{a}{c} \quad \frac{4PR}{a^2 E^*} \left(1 - \frac{Q}{\mu P}\right) = \frac{\pi - 2\theta_0}{2 \sin^2 \theta_0} - \cot \theta_0 \quad (6.8)$$

Where

$$\frac{x}{c} = \sin \theta$$

the corrective distribution  $q^*$  is given by the below expression:

$$\frac{c q^*(\theta)}{\mu P - Q} = -\frac{2/\pi}{\pi - 2\theta_0 - \sin 2\theta_0} \left\{ (\pi - 2\theta_0) \cos \theta + \ln \left[ \left| \frac{\sin(\theta + \theta_0)}{\sin(\theta - \theta_0)} \right|^{\sin \theta} \cdot \left| \tan \frac{\theta + \theta_0}{2} \tan \frac{\theta - \theta_0}{2} \right|^{\sin \theta_0} \right] \right\} \quad (6.9)$$

### 6.3 Tangential stiffness

Using the pressure and shear distributions given above, through the theory of the potential of Boussinesq-Cerruti [45] it is possible to evaluate the tangential displacement  $u_{x1}$ ,  $u_{x2}$  [44] of the two bodies and therefore their relative displacement  $\delta x$  as a function of the normal load  $N = P \cdot L$  and tangential load  $T = Q \cdot L$ :

$$\delta_x = u_{x1} - u_{x2} = \frac{2}{\pi E^*} \left[ -\int_{-b}^b q_x(r) \ln \left| \frac{r}{b} \right| dr + Q \left( \ln \left| \frac{r}{b} \right| + \frac{v}{1-v} \right) \right] = f(P, Q) \quad (6.10)$$

The tangential stiffness as a function of the normal force  $N$  was then calculated numerically:

$$k_t(N) = \left( \frac{\partial T}{\partial \delta_x} \right)_{\delta_x=0} = \frac{1}{\left( \frac{\partial \delta_x}{\partial T} (N, T) \right)_{T=0}} \quad (6.11)$$

Tangential stiffness variations considering the normal Force is shown in Figure 6.7.

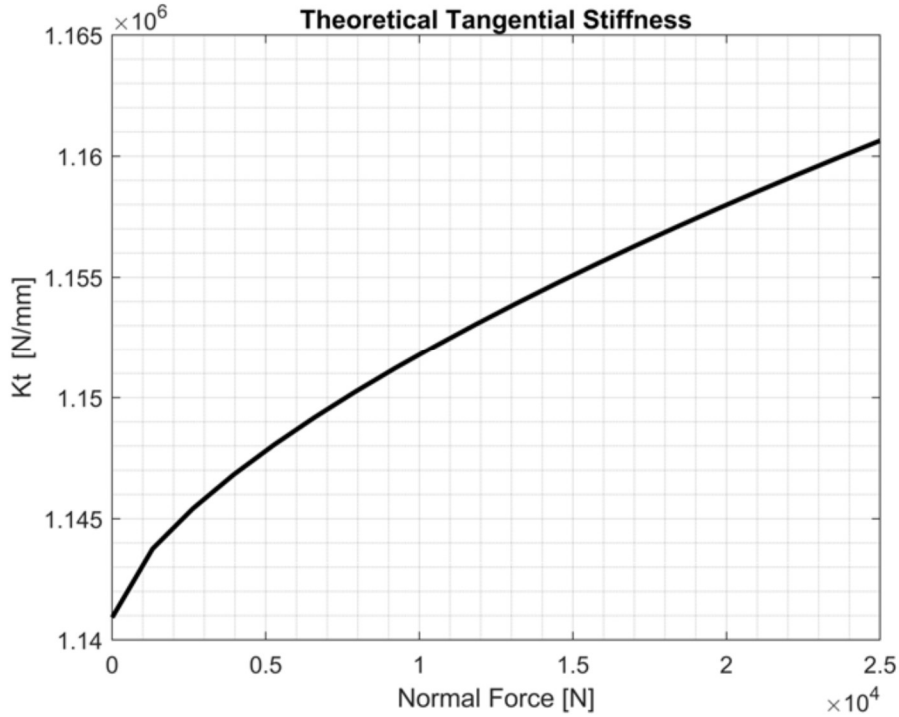


Figure 6.7: Tangential Stiffness variations considering the Normal Force

## 6.4 Normal Stiffness

Similarly to what was done for tangential stiffness, pressure distribution is possible calculate the normal displacements  $u_{z1}$ ,  $u_{z2}$  through the theory of potential [45] studying separately the influence of pressure on the displacement  $u_z$ , or by analyzing the case in which  $q_x = 0$ :

$$u_z = \frac{1-\nu^2}{\pi E} \int_{\Sigma} p(r, s) \cdot \frac{1}{\rho(r, s)} dr ds \quad \rho = \sqrt{(r-x)^2 + (s-y)^2 + z^2} \quad (6.12)$$

In the case in question, a constant  $p = p(r)$  distribution along  $L$ .

$$\begin{aligned}
u_{z0} = u_z(x = y = z = 0) &= \frac{1 - \nu^2}{\pi E} \int_{-b}^b p(r) \cdot \left( \int_{-L/2}^{L/2} \frac{1}{\sqrt{r^2 + s^2}} ds \right) dr \\
&= \frac{1 - \nu^2}{\pi E} \int_{-b}^b p(r) \cdot \left[ \ln \left| s + \sqrt{s^2 + r^2} \right| \right]_{-L/2}^{L/2} dr = \\
&= \frac{1 - \nu^2}{\pi E} \int_{-b}^b p(r) \cdot \ln \left| \frac{\frac{L}{2} + \sqrt{\left(\frac{L}{2}\right)^2 + r^2}}{-\frac{L}{2} + \sqrt{\left(\frac{L}{2}\right)^2 + r^2}} \right| dr
\end{aligned} \tag{6.13}$$

Therefore the relative displacement is:

$$\delta_z = u_{z1} - u_{z2} = \frac{1}{\pi E^*} \int_{-b}^b p(r) \cdot \ln \left| \frac{\frac{L}{2} + \sqrt{\left(\frac{L}{2}\right)^2 + r^2}}{-\frac{L}{2} + \sqrt{\left(\frac{L}{2}\right)^2 + r^2}} \right| dr \tag{6.14}$$

The normal stiffness as a function of the normal force N was then calculated numerically:

$$k_n(N) = \frac{\partial N}{\partial \delta_z} = \frac{1}{\frac{\partial \delta_z}{\partial N}(N)} \tag{6.15}$$

Normal stiffness variations considering the normal force is shown in Figure 6.8.

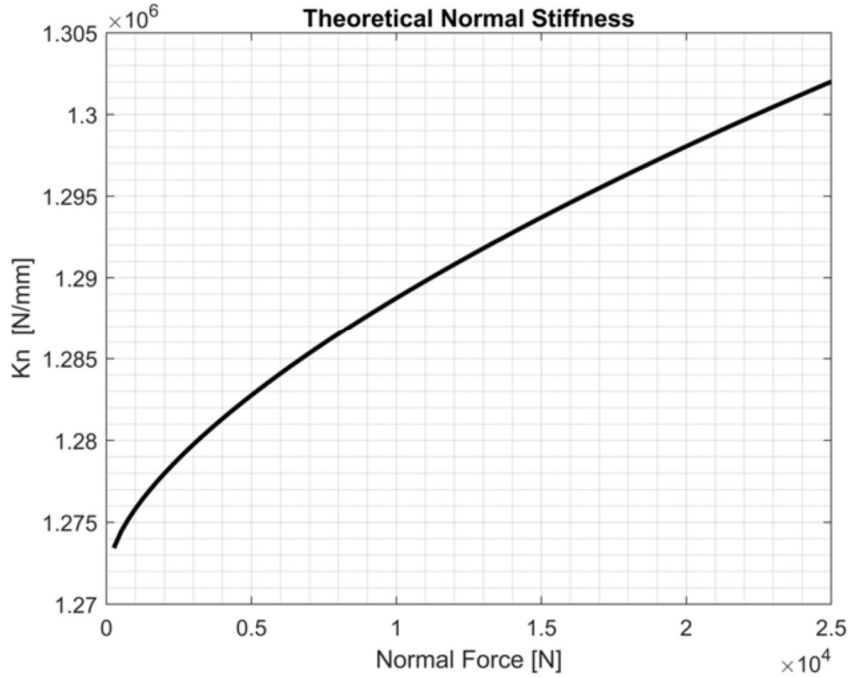


Figure 6.8: Normal Stiffness variations considering the Normal Force

## 6.5 Comparison of the Stiffness values obtained with the theoretical ones

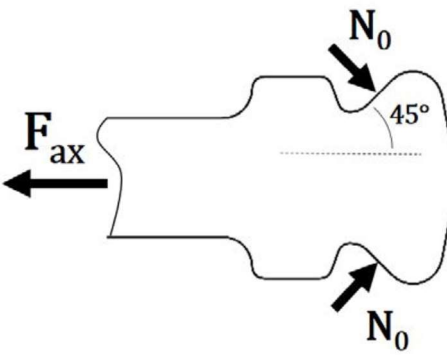


To compare the theoretical stiffness  $k_n$ ,  $k_t$  of the contact with the nodal stiffness obtained from the model FEM it was necessary to multiply these stiffness by the number of nodes at the interface which here is 33.

$$\begin{aligned} (k_n)_{tot} &= 33 \cdot (k_n)_{nodal} & \left(\frac{\delta k_n}{k_n}\right)_{tot} &= \left(\frac{\delta k_n}{k_n}\right)_{nodal} \\ (k_t)_{tot} &= 33 \cdot (k_t)_{nodal} & \left(\frac{\delta k_t}{k_t}\right)_{tot} &= \left(\frac{\delta k_t}{k_t}\right)_{nodal} \end{aligned} \quad (6.16)$$

The theoretical stiffness are functions of the normal force  $N$ , instead the results of the present work are reported as a function of the axial traction force. To compare the results the borderline cases  $T = 0$  and  $T = \mu N$  were considered:

$$2(N \sin \theta + T \cos \theta) = F_{ax}$$

$$F_{ax} = \begin{cases} (2 \sin \theta) \cdot N & @T = 0 \\ 2(\sin \theta + \mu \cos \theta) \cdot N & @T = \mu N \end{cases}$$


Thus, by reporting the comparison between the obtained and theoretical stiffness (Figures 6.9, 6.10), it was noted that the numerical-experimental procedure used in the present work provides some rigidity higher than those of the analytical model and a dependence of the stiffness on the axial force more marked than the theoretical one.

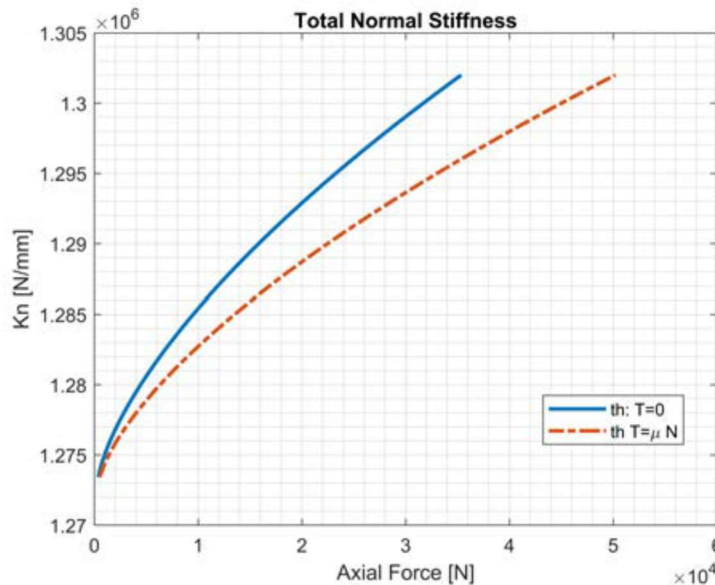


Figure 6.9: Normal Stiffness variation in two states  $T=0$  and  $T=\mu N$

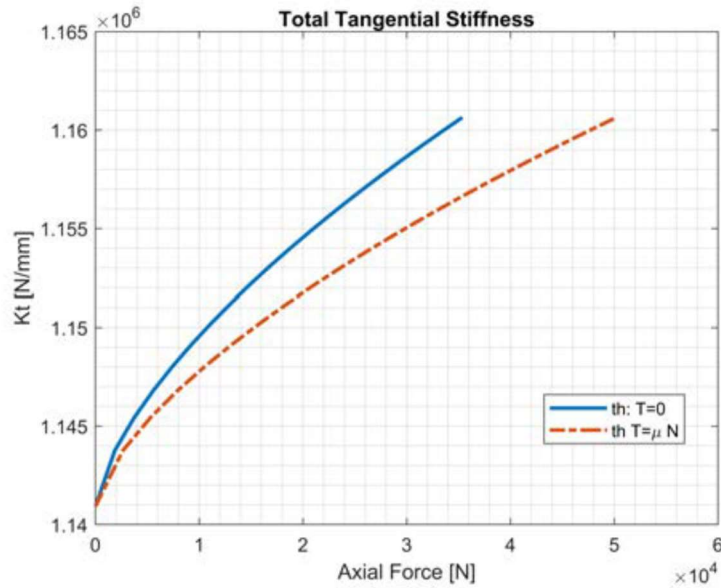


Figure 6.10: Tangential Stiffness variation in two states  $T=0$  and  $T=\mu N$

Furthermore, theoretical vs numerical-experimental comparison of normal stiffness is shown in Figure 6.11 and this comparison for tangential stiffness is shown in Figure 6.12. As shows in these figures, there is a difference between the numerical-experimental results and theoretical ones that comes from different reasons including: considered simplicity in 2D of a punch in a surface and the errors of experimental procedure, however the contact model can be considered as an indicative method for further investigations.

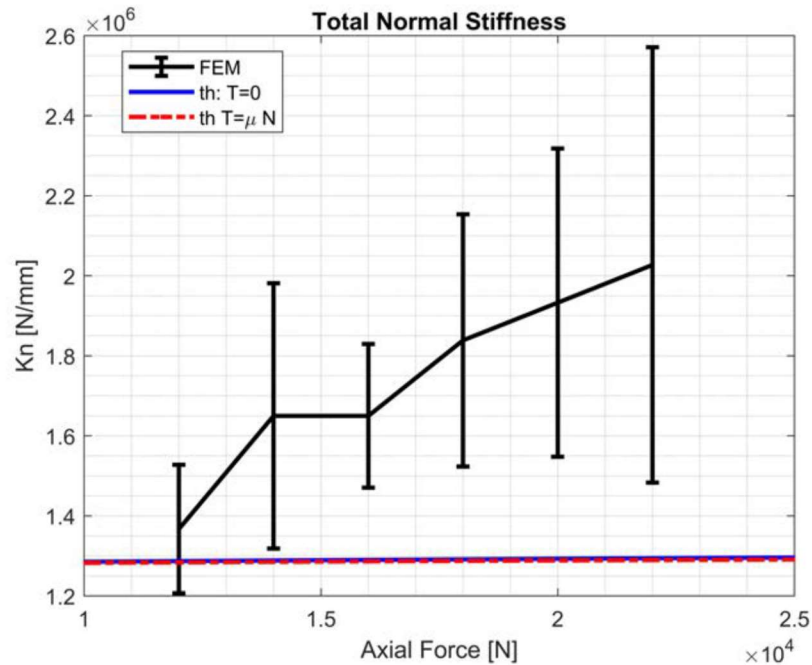


Figure 6.11: Theoretical vs numerical-experimental comparison of normal stiffness

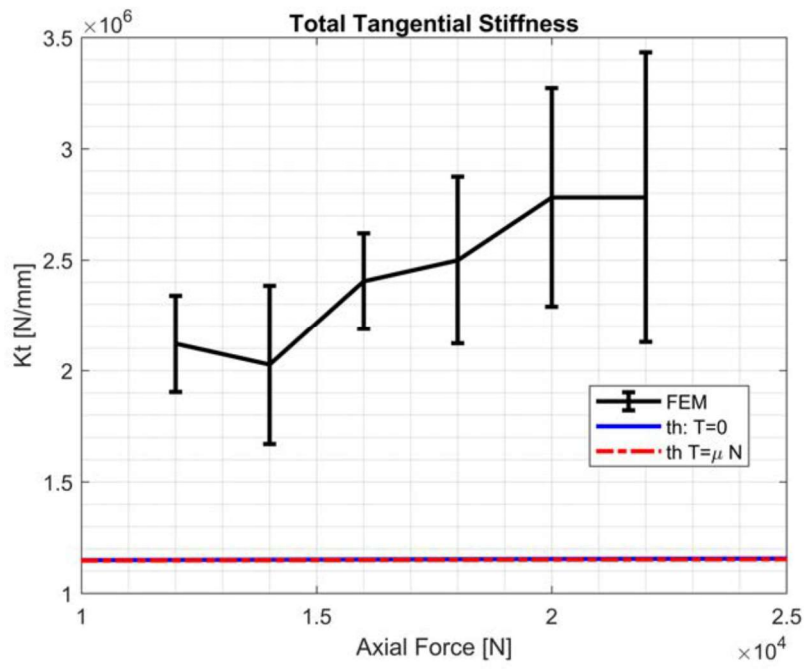


Figure 6.12: Theoretical vs numerical-experimental of tangential stiffness

# Chapter 7

## Conclusions

As mentioned in the below summary, in this research valuable outcomes for further contact mechanics studies in design and analysis of blade root joints are obtained.

- An experimental method has been defined for the identification of modal parameters (frequency and damping) of a system that simulates the vibrations of a turbine blade connected to the disc via a dovetail joint.

The first and second flexural modes of the system were investigated. The frequency and damping were extracted from the free response of the following system to an oscillatory excitation with a frequency close to the modal form in question.

The nonlinear dependence of frequency and damping on the vibration amplitude was obtained, as the axial traction force varies (simulating the centrifugal force of the blade)

- A numerical-experimental method has been defined for the determination of stiffness normal  $k_n$  and tangential contact  $k_t$  for the system under investigation.
- The obtained stiffness were compared with those of a theoretical model of contact

Final remarks on the results of the measurements are summarized as follows:

- As the centrifugal force increases, the damping decreases. This probably is due to the reduction of the micro-sliding area of the contact regions
- As the centrifugal force increases, the natural frequency of each mode increases, such as provided by the analytical models [30]
- In the range of axial forces analyzed ( $F_{ax} < 25\text{kN}$ , similar to the centrifugal forces for the headstock), the nonlinear dependence of natural frequencies and amplitude damping of vibration is not negligible.

- The linear behavior of the dovetail joint, i.e. the complete adhesion of the contacts, occurs only for small vibration amplitudes and high centrifugal loads ( $F_{ax} > 8\text{kN}$  and  $A < 2\mu\text{m}$  for the first flexural mode;  $F_{ax} > 12\text{kN}$  and  $A < 2\mu\text{m}$  for the second flexural mode)
- The dependence of natural frequencies on the Centrifugal Force differs from that expected from the analytical models [30] for force values lower than 12kN. This difference is attributable to the micro-sliding of the contacts.
- The previous observations imply that for low centrifugal forces, the effect of nonlinearity contact must be considered for a correct estimate of the resonance frequencies. Finally, it has been noted that this range of centrifugal forces corresponds to the speeds of rotation of the turbines associated with the descent phase of aircraft flight.

Final remarks on the results of the numerical research of  $k_n$ ,  $k_t$  are summarized as follows:

- The stiffness  $k_n$ ,  $k_t$  obtained have a significant dependence on the axial force (similar to the centrifugal force of the blade), showing an increasing trend with increasing force.
- This trend can also be found in the theoretical model of contact adopted in the present work for comparison of results. However, the variation of stiffness predicted by this analytical model is negligible compared to the variation obtained with the numerical procedure proposed here.
- The theoretical values of the stiffness turn out to be about half of those obtained here. This probably is due to the imperfect correspondence between the geometry in the theoretical model and real contact.
- The relatively large uncertainty of the obtained stiffness with the numerical-experimental method (of the order of 15%) is due to the weak sensitivity of natural frequency to variation of the stiffness of the contacts.

## Possible further developments

The research of the stiffness  $k_n$ ,  $k_t$  was carried out here using linear contact elements and comparing only the frequencies of the model with those measured in the range of forces and amplitudes, so the system exhibits a linear behavior. The vibration amplitude was not used for this research.

A possible development to include this further condition and possibly reduce uncertainty of the obtained stiffness consists in:

- The implementation of the nonlinear contact element
- Simulation of the free response of the system through direct time integration comprising the nonlinear behavior of the contacts
- Comparison of the simulation results with the measurements made in the present work.

# Appendix A

## Technical Data of Blade Roots Tested

### A1.1 Dovetail Joint

Dovetail joint utilized in blade root damping tests was machined with the same geometry of a real blade, precisely the sixth turbine stage of Avio turbo engine GE90.



Figure A1.1. GE90 turbo engine

Knowing the rotation speed of the rotor and the mass of the blade (here not reported for confidence reasons) it is easy to evaluate the centrifugal force acting on the blade. On the real engine, the maximum load that would act on the studied dovetail joint is 35kN, corresponding to the take-off of the aircraft (Fig A1.2).

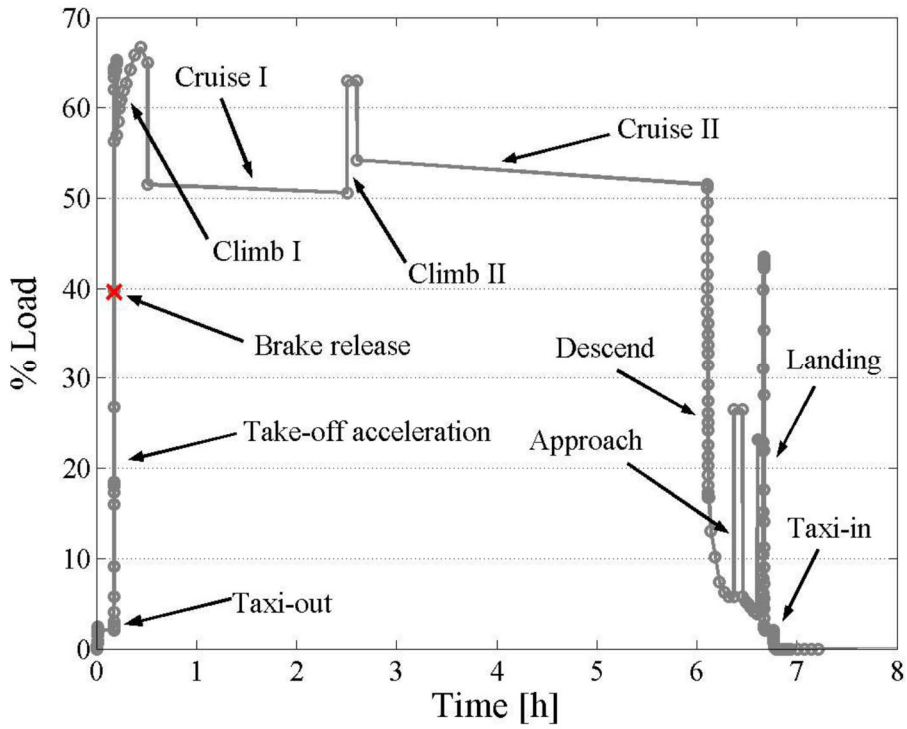


Figure A1.2. Variation of the centrifugal force acting on the blade during a typical flying plan.

This engine is used for power generation, so that the centrifugal load acting on the blades is almost constant in working condition (Fig A1.3). In the tests a maximum load equal to 10% more than upper limit of the operative range, equal to about 44kN, is used. In Fig (A1.3) it can be seen that the rotational speed of the shaft is reduced to 3600 rpm by means of a reduction gear to produce 60 Hz electric energy.

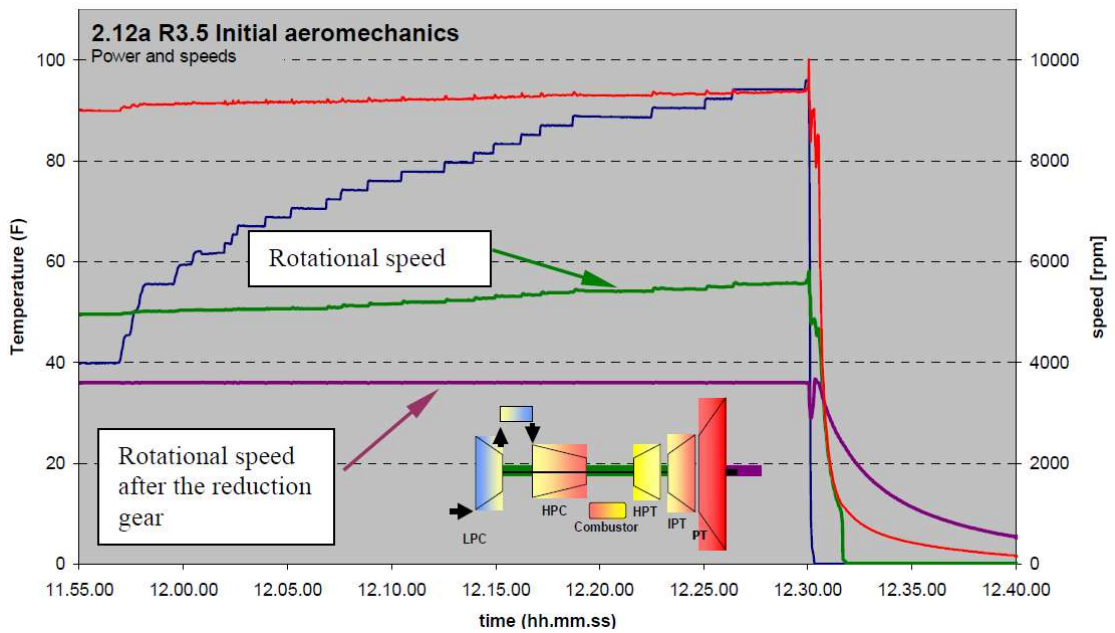


Figure. A1.3. Rotational speed in working condition

## Appendix B

### Theoretical estimate of the stiffening effect of the Traction force

The stiffening effect due to the axial traction force was initially estimated analytically through the method proposed in [30].

#### Dynamic model of the beam with stiffening effect

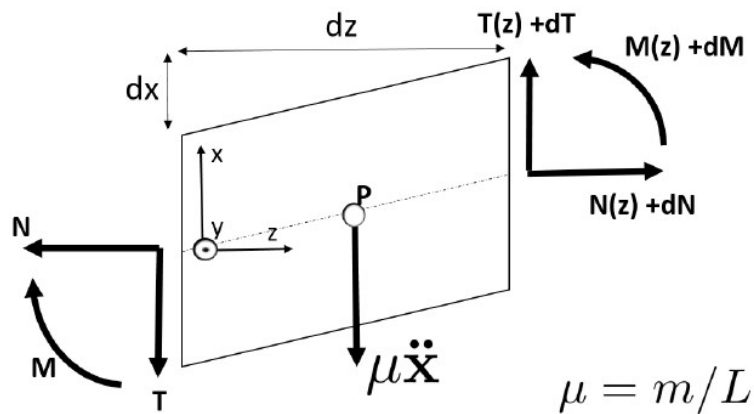


Figure B.1: Elementary segment of the deformed beam

The equilibrium equations of the elementary segment of the deformed beam are:



$$\begin{cases} dT - \mu \ddot{x} dz = 0 \\ N - N - dN = 0 \\ M + dM - M + T \frac{dz}{2} \cdot 2 + dT \frac{dz}{2} - Nd x - dN \frac{dx}{2} = 0 \end{cases} \Rightarrow \begin{cases} \frac{dT}{dz} = \mu \ddot{x} \\ \frac{dN}{dz} = 0 \\ \frac{dM}{dz} + T - N \frac{dx}{dz} = 0 \end{cases} \quad (\text{B-1})$$

Deriving the last equation in z:

$$\frac{d^2 M}{dz^2} + \frac{dT}{dz} - \frac{d}{dz} \left( N \frac{dx}{dz} \right) = 0 \quad (\text{B-2})$$

Using the other two equilibrium equations:

$$\frac{d^2 M}{dz^2} + \mu \ddot{x} - N \frac{d^2 x}{dz^2} = 0 \quad (\text{B-3})$$

From geometric considerations:

$$\begin{aligned} dw &= x \tan(-d\alpha_y) \simeq -x \cdot d\alpha_y \quad \Rightarrow \quad \varepsilon_{zz} = \frac{dw}{dz} = -\frac{d\alpha_y}{dz} \cdot x = -k_y \cdot x \\ M &= -\int \sigma_{zz} \cdot x dA = -\int E \varepsilon_{zz} x dA = +\int E k_y x^2 dA = E k_y I_y \quad \Rightarrow \quad k_y = \frac{M}{EI_y} \\ \alpha_y &\simeq \tan \alpha_y = \frac{dx}{dz} \quad \Rightarrow \quad k_y = \frac{1}{r} = \frac{d\alpha_y}{dz} = \frac{d^2 x}{dz^2} \quad \Rightarrow \quad M = EI_y \frac{d^2 x}{dz^2} \end{aligned} \quad (\text{B-4})$$

Substituting in (B-3):

$$EI_y \frac{d^4 x}{dz^4} + \mu \ddot{x} - N \frac{d^2 x}{dz^2} = 0 \quad (\text{B-5})$$

Applying the method of separating variables:

$$EI_y \frac{d^4 X}{dz^4} q + \mu X \ddot{q} - N \frac{d^2 X}{dz^2} q = 0 \quad \Rightarrow \quad \mu X \ddot{q} + \left[ EI_y \frac{d^4 X}{dz^4} - N \frac{d^2 X}{dz^2} \right] \cdot q = 0 \quad (\text{B-6})$$

Assuming harmonic solution  $q(t) = \cos(\omega(t) + \phi)$  and dividing by  $q(t)$ :

$$-\omega^2 \mu X + EI_y \frac{d^4 X}{dz^4} - N \frac{d^2 X}{dz^2} = 0 \quad (\text{B-7})$$

By dimensioning z:  $Z = z / L$ :

$$\frac{EI_y}{L^4} \frac{d^4 X}{dZ^4} - \frac{N}{L^2} \frac{d^2 X}{dZ^2} - \mu \omega^2 X = 0 \quad (\text{B-8})$$

Multiplying by X and integrating in z by the length of the beam:

$$\frac{EI_y}{L^4} \int_0^1 X \frac{d^4 X}{dZ^4} dZ - \frac{N}{L^2} \int_0^1 X \frac{d^2 X}{dZ^2} dZ - \mu \omega^2 \int_0^1 X^2 dZ = 0 \quad (\text{B-9})$$

By imposing the boundary conditions of the beam wedged at both ends:

$$\begin{cases} X(Z=0) = 0 \\ \alpha_y(Z=0) = \frac{dX}{dZ} = 0 \end{cases} \quad \begin{cases} X(Z=1) = 0 \\ \alpha_y(Z=1) = \frac{dX}{dZ} = 0 \end{cases} \quad (\text{B-10})$$

The first integral becomes:

$$\begin{aligned} \int_0^1 X \frac{d^4 X}{dZ^4} dZ &= \left[ X \cdot \frac{d^3 X}{dZ^3} \right]_0^1 - \int_0^1 \frac{dX}{dZ} \frac{d^3 X}{dZ^3} dZ = \\ &= - \left\{ \left[ \frac{dX}{dZ} \cdot \frac{d^2 X}{dZ^2} \right]_0^1 - \int_0^1 \left( \frac{d^2 X}{dZ^2} \right)^2 dZ \right\} = + \int_0^1 \left( \frac{d^2 X}{dZ^2} \right)^2 dZ \end{aligned} \quad (\text{B-11})$$

the second integral becomes:

$$\int_0^1 X \frac{d^2 X}{dZ^2} dZ = \left[ X \frac{dX}{dZ} \right]_0^1 - \int_0^1 \left( \frac{dX}{dZ} \right)^2 dZ = - \int_0^1 \left( \frac{dX}{dZ} \right)^2 dZ$$

$$\frac{EI_y}{L^4} \int_0^1 \left( \frac{d^2 X}{dZ^2} \right)^2 dZ + \frac{N}{L^2} \int_0^1 \left( \frac{dX}{dZ} \right)^2 dZ - \mu \omega^2 \int_0^1 X^2 dZ = 0$$

The natural pulsation  $\omega$  can therefore be estimated with the expression:

$$\omega^2 = \frac{EI_y}{\mu L^4} \frac{\int_0^1 \left( \frac{d^2 X}{dZ^2} \right)^2 dZ}{\int_0^1 X^2 dZ} + N \cdot \frac{1}{\mu L^2} \frac{\int_0^1 \left( \frac{dX}{dZ} \right)^2 dZ}{\int_0^1 X^2 dZ} = (\omega_n^2)_{N=0} + N \cdot \frac{1}{\mu L^2} \frac{\int_0^1 \left( \frac{dX}{dZ} \right)^2 dZ}{\int_0^1 X^2 dZ} \quad (\text{B-12})$$

where  $(\omega_n^2)_{N=0}$  is the natural pulsation obtained from the beam model without stiffening effect described below - and the modal form  $X$  is approximated with that of the following model.

## Dynamic model of the beam without stiffening effect

$$+EI_y \frac{d^4 X}{dZ^4} - \omega^2 \mu X = 0 \quad \Rightarrow \quad \frac{d^4 X}{dZ^4} - \beta^4 X = 0 \quad \text{con } \beta^4 = \frac{\mu \omega^2}{EI_y} \quad (\text{B-13})$$

whose solution is known:

$$X(z) = A \cos(\beta z) + B \sin(\beta z) + D \cosh(\beta z) + E \sinh(\beta z) \quad (\text{B-14})$$

Defining for simplicity of notation:

$$c = \cos(\beta L) \quad s = \sin(\beta L) \quad ch = \cosh(\beta L) \quad sh = \sinh(\beta L)$$

By imposing the boundary conditions:

$$X(z=0) = 0 \quad \Rightarrow \quad A = -D$$

$$X(z=L) = 0 \quad \Rightarrow \quad Ac + Bs + Dch + Esh = 0$$

$$\frac{dX}{dz} = -A\beta \sin(\beta z) + B\beta \cos(\beta z) + D\beta \sinh(\beta z) + E\beta \cosh(\beta z)$$

$$\frac{dX}{dz}(z=0) = 0 \quad \Rightarrow \quad B = -E$$

$$\frac{dX}{dz}(z=L) = 0 \quad \Rightarrow \quad \beta(-As + Bc + Dsh + Ech) = 0$$

(B-15)

By putting the four expressions found into a system:

$$\begin{bmatrix} (ch-c) & (sh-s) \\ (sh+s) & (ch-c) \end{bmatrix} \begin{Bmatrix} D \\ E \end{Bmatrix} = \begin{Bmatrix} 0 \\ 0 \end{Bmatrix}$$

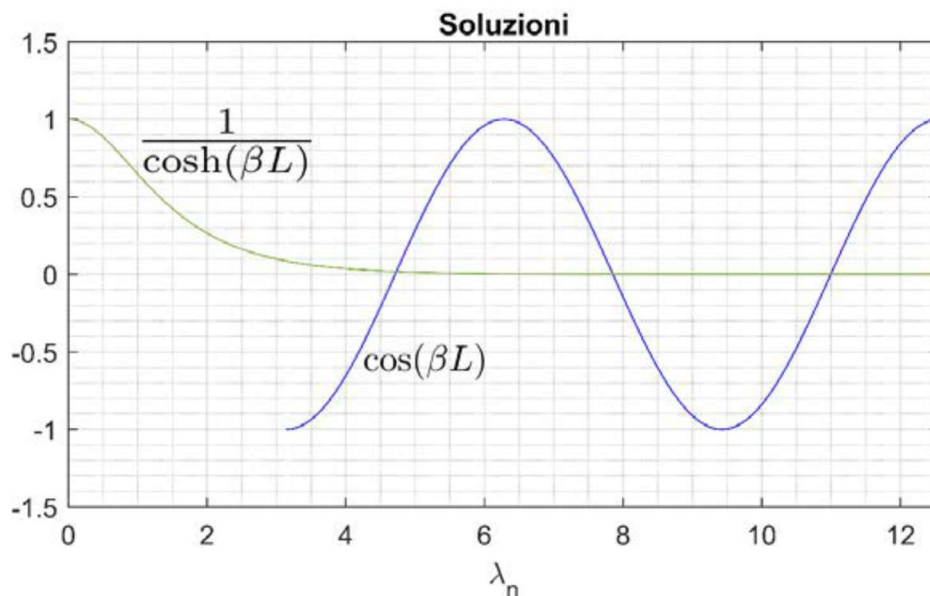
(B-16)

whose non-trivial solution is found by nullifying the determinant:

$$\cos(\beta L) \cdot \cosh(\beta L) = +1$$

$$\lambda_n = \beta L \quad \beta^4 = \frac{\mu \omega^2}{EI_y} \quad \Rightarrow \quad \omega_n = \left( \frac{\lambda_n}{L} \right)^2 \sqrt{\frac{EI_y}{\mu}}$$

(B-17)

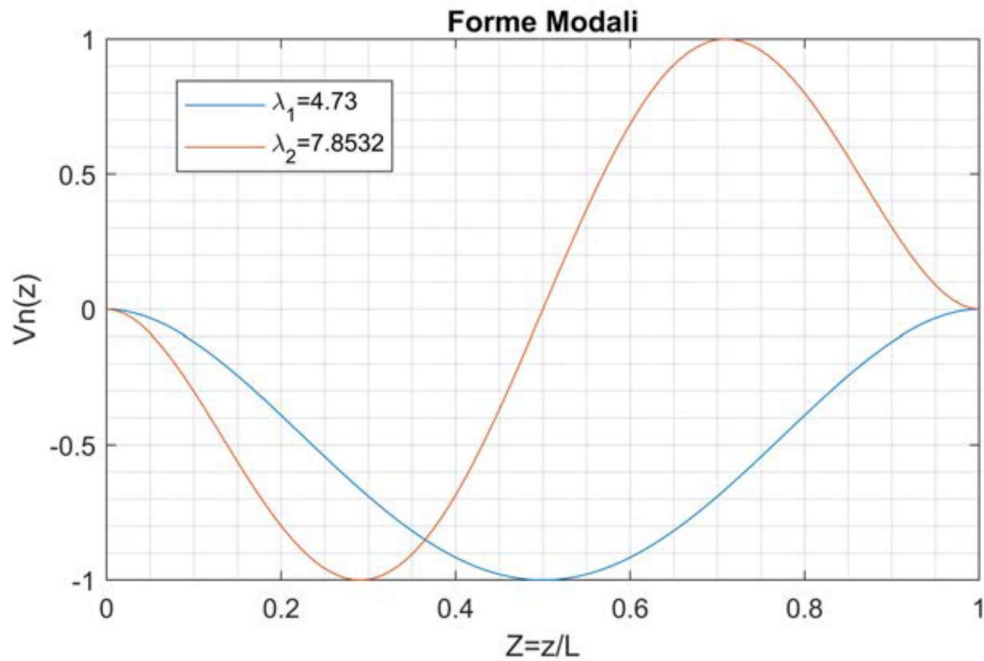


The modal forms can then be calculated:

$$D_n = -\frac{sh-s}{ch-c} E_n \quad \beta z = \frac{\lambda_n}{L} \cdot z = \lambda_n Z$$

(B-18)

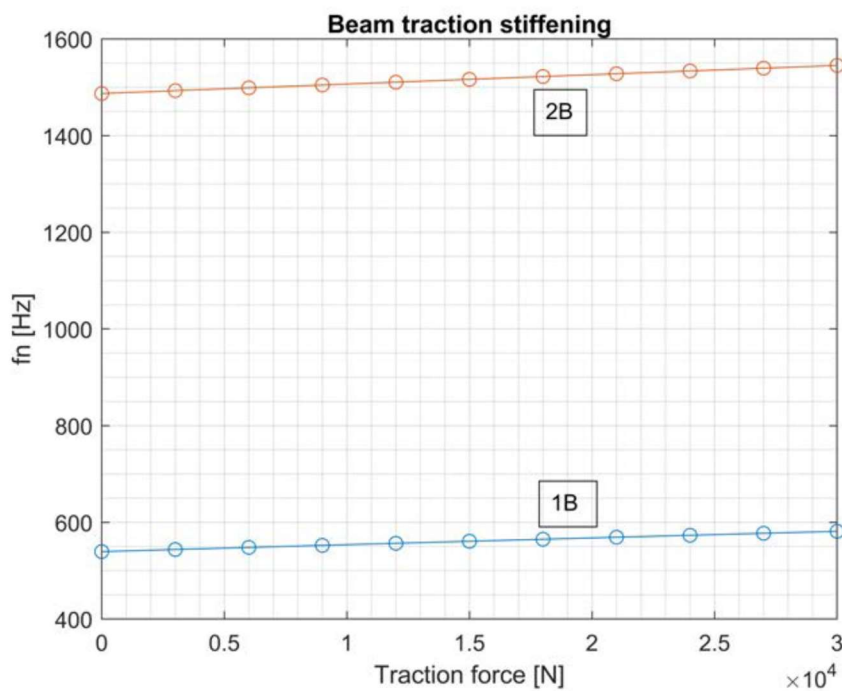
$$X_n(Z) = E_n \left[ \sinh(\lambda_n Z) - \sin(\lambda_n Z) - \left( \frac{\sinh(\lambda_n L) - \sin(\lambda_n L)}{\cosh(\lambda_n L) - \cos(\lambda_n L)} \right) (\cosh(\lambda_n Z) - \cos(\lambda_n Z)) \right]$$



With  $I_y = hb^3/12$

So through expression 9.4 it was possible to calculate the stiffening effect:

F [%]	0	0.1	0.2	0.3	0.4	0.5	0.6	0.7	0.8	0.9	1	
F [N]	0	3000	6000	9000	12000	15000	18000	21000	24000	27000	30000	
n \ λn	fn [Hz]											
1	4.730	539.5	543.8	548.1	552.4	556.6	560.8	565.0	569.2	573.3	577.4	581.4
2	7.853	1487.0	1492.9	1498.8	1504.7	1510.5	1516.3	1522.1	1527.9	1533.7	1539.4	1545.1



## Appendix C

### Cylindrical Hertzian Contact

Surface displacements for a cylindrical Hertzian contact problem have been published by Poritsky (1950). In his work the displacements on the surface of an half plane loaded are provided by a shear traction distribution given by:

$$q(x) = \frac{2Q}{\pi b} \sqrt{1 - \left(\frac{x}{b}\right)^2} \quad (\text{C-1})$$

where  $Q$  is the tangential load, per unit of length, applied to the bodies in contact and  $b$  is the half width of contact area. The displacements on the surface are:

$$u(x) = \frac{2Q}{\pi E^*} \left(\frac{x}{b}\right)^2 + C_1 \quad \text{if } |x| \leq b$$

$$u(x) = \frac{2Q}{\pi E^*} \left( \ln \left( \left| \frac{x}{b} \right| + \sqrt{\left(\frac{x}{b}\right)^2 - 1} \right) + \frac{1}{2} \left( \left(\frac{x}{b}\right) + \sqrt{\left(\frac{x}{b}\right)^2 - 1} \right)^{-2} \right) + C_2 \quad \text{if } |x| \geq b$$

The slip between the two bodies can be evaluated conveniently by superposition of the solution for the surface displacements (Eqs. 2) in the sliding case, since  $q(x)$  is the sum of two elliptical distributions (Chapter 5)

$$s(x) = 2 \cdot u(x) = 2 \cdot \frac{2}{\pi E^*} \mu P \left(\frac{c}{b}\right)^2 \left[ \frac{x}{c} \sqrt{\left(\frac{x}{c}\right)^2 - 1} - \ln \left( \left(\frac{x}{c}\right) + \sqrt{\left(\frac{x}{c}\right)^2 - 1} \right) \right]$$

where the constants C1 and C2 are removed imposing that the slip vanishes in the stick region. This equation has been utilized to check the Matlab routine written to evaluate displacements for a flat pad with rounded edges. It is obtained the cylindrical solution reducing to zero the flat part. In the following figure the results obtained by numerical integration, Eq. 5.29, and the analytical formulation are compared. The two approaches, confirming the correctness of the routine applied, provide the same results.

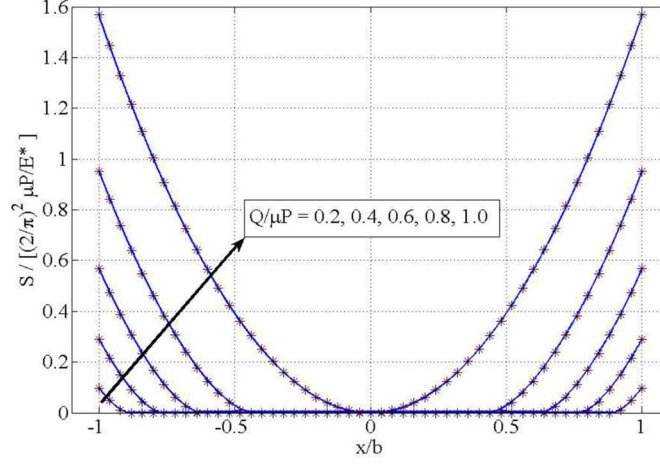


Figure C.1. Displacements on contact surface for a cylindrical Hertzian contact.

Solid line, numerical solution; asterisks, analytical solution.

Another useful benchmark, provided by Poritsky solution, concerns the dissipated energy calculation. Indeed the damage parameter,  $D$ , in the case of incipient full sliding, for the Hertzian case, is:

$$D_{Lim} = \frac{\mu^2 P b}{\pi R} \left( \frac{x}{b} \right)^2 \sqrt{1 - \left( \frac{x}{b} \right)^2}$$

This function is analytically integrable on the slip area providing the dissipated energy:

$$E_{Lim} = \frac{\mu^2 P b^2}{\pi R} \int_{A_{SLIP}} \left( \frac{x}{b} \right)^2 \sqrt{1 - \left( \frac{x}{b} \right)^2} d\left( \frac{x}{b} \right)$$

Inserting in Eq. A4.5

$$b^2 = \frac{4 PR}{\pi E^*}$$

And evaluating the integral ( $x/b = t$ ),

$$E_{Lim} = \left( \frac{2}{\pi} \right)^2 \frac{(\mu P)^2}{E^*} \left[ \frac{1}{8} \left( t \sqrt{1-t^2} (2t^2-1) + a \sin(t) \right) \right]_{-1}^1 = \left( \frac{2}{\pi} \right)^2 \frac{(\mu P)^2}{E^*} \cdot \frac{\pi}{8}$$

Introducing in Eq. A4.7 the same dimensionless used in Fig. 5.15. (Chapter 5), and bearing in mind that the energy dissipated in a full load cycle is equal to four time the energy evaluated in A4.5 (  $Q$  varies fro 0 to  $Q_{max}$ , from  $Q_{max}$  to 0, from 0 to  $-Q_{MAX}$ , from  $-Q_{MAX}$  to zero ) the value,  $\pi/2$  plotted in Fig A4.5 is obtained:

$$\frac{E_{Lim}}{\left( \frac{2}{\pi} \right)^2 \frac{(\mu P)^2}{E^*}} = \frac{\pi}{2}$$

## Appendix D

### HBM and Harmonic Contact Stiffness

The hypothesis standing over the harmonic balance method (HBM) assumes that the output signals,  $y(t)$ , of a non-linear dynamic system, are periodic with the same period of the input signal,  $x(t)$ .

The Fourier first order approximation of a generic function,  $f_t(\theta)$ , is calculated as:

$$F_0 = \frac{1}{2\pi} \int_0^{2\pi} f(\vartheta) d\vartheta$$

$$F_c = \frac{1}{\pi} \int_0^{2\pi} f_t(\vartheta) \cos(\vartheta) d\vartheta$$

$$F_s = \frac{1}{\pi} \int_0^{2\pi} f_t(\vartheta) \sin(\vartheta) d\vartheta$$

$$(\vartheta = \omega t)$$

$$f_t(\vartheta) \cong F_c \cos(\vartheta) + F_s \sin(\vartheta) = |F_t| \cos(\vartheta + \varphi)$$

Through the use of rotating vectors it is easy to demonstrate that:

$$|F_t| = \sqrt{F_c^2 + F_s^2}$$

$$\tan(\varphi) = \frac{F_s}{F_c}$$

In the case of friction forces, if the output signal is the tangential force acting on the contact interface,  $F_t$  is the amplitude of the harmonic output signal approximating the

friction force, while  $\varphi$  is the phase between the input signal (the harmonic oscillation  $u(\theta)$ ) and the friction force approximation  $f_t(\theta)$ . In a complex notation it is possible to write

$$f_t(\vartheta) = \text{Re}\left(F_t |e^{j\varphi} e^{j\vartheta}\right)$$

$$|F_t| e^{j\varphi} = \text{Re}(F_t) + j \text{Im}(F_t)$$

Then

$$F_c = \text{Re}(F_t)$$

$$F_s = -\text{Im}(F_t)$$

The tangential force creating a hysteresis loop is substituted by harmonic force oscillating with the angular frequency of the exciting force (Fig. A5.1):

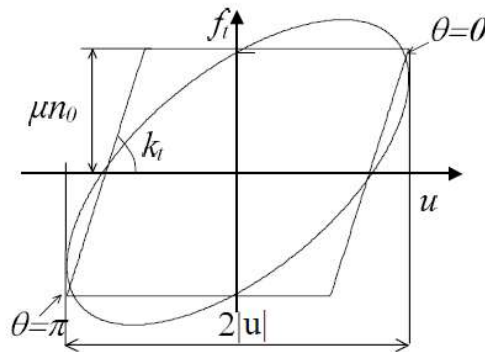


Figure. A5.1

It can be noted that in this appendix the value  $\theta=0$  corresponds to the maximum displacement of the harmonic tangential relative displacement. When HBM is included in the equilibrium equations of a dynamic system, it is necessary to remember that the displacement has a further phase  $\psi$  due to the presence of some kind of structural damping not equal to zero which determines the phase delay between the response and the excitation force. The excitation force is in fact usually chosen as reference input signal. Hence also the HBM approximated non-linear force must be shifted in time with respect to this delay in order to be inserted in the equilibrium equations (Fig. A5.2).

The non-linear contact forces can also be seen as complex stiffness. The non-linear force approximated by truncating the Fourier series to the first order can be divided into two components: one component proportional to the relative displacement and one component that has a phase delay of  $\pi/2$  with respect to  $u(t)$  (Fig.A5.2).



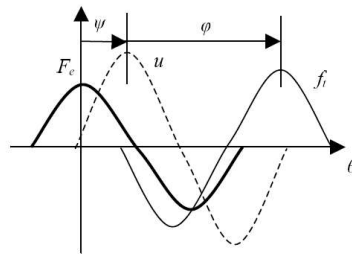


Figure. A5.2

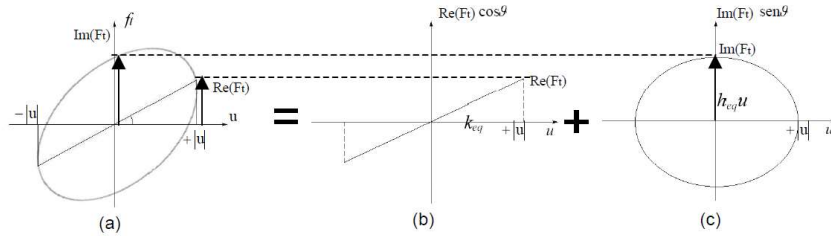


Figure. A5.3

For  $\theta = \pi/2$ :  $f_t(t=T/4) = -\text{Im}(F_t)$ . Hence the maximum value for the two components (Fig.A5.3b-c) are determined.

If the real part of  $F_t$  is divided for the amplitude of  $u(t)$  an equivalent stiffness  $k_{eq}$  determined. If the imaginary part of  $F_t$  is divided for the amplitude of an equivalent hysteretic damping  $h_{eq}$  is determined. The sum of the two components divided for  $|u|$  forms a complex stiffness:

$$\frac{F_t}{|u|} = \frac{|F_t| e^{j\varphi}}{|u|} = \frac{\text{Re}(F_t)}{|u|} + j \frac{\text{Im}(F_t)}{|u|}$$

$$\bar{k} = k_{eq} + j h_{eq}$$

# Appendix E

## Normal Contact Stiffness

To evaluate the normal contact stiffness, the pressure distributions and size of the contact area developed for 2D contact problem were used, as shown in Chapter 5. To determine the deformation, the contact area will be taken as being a finite rectangle with one side very much greater than the other, keeping constant the pressure distribution in the larger dimension. It is the same approach with the same hypotheses, based on Cerruti and Bussinesq potential theory, employed in the Chapter 5 to evaluate the tangential displacement at the contact.

If the contact pressure is known it may be substituted in the following equation to obtain the surface displacements ( $z = 0$ ) normal to the contact:

$$u_z = \frac{1 - \nu^2}{\pi E} \iint_{A_{slip}} \frac{p(r, s)}{R} \cdot dr \cdot ds \quad \text{where} \quad R^2 = (x - r)^2 + (y - s)^2 + z^2$$

To obtain the displacement at the centre of the contact, Eq. A6.1 is evaluated in  $x = 0$  and  $y = 0$ .

$$u_z = \frac{1 - \nu^2}{\pi E} \int_{-b}^b p(r) \cdot 2 \int_0^{L/2} \frac{dr}{\sqrt{r^2 + s^2}} ds$$

By evaluating the second integral in Eq. A6.2 with the assumption that  $L \gg b$ ,

$$u_z = \frac{2(1 - \nu^2)}{\pi E} \int_{-b}^b p(r) \cdot \ln \left| \frac{L}{r} \right| ds$$

That can be rewritten in a more useful form

$$u_z = \frac{2(1 - \nu^2)}{\pi E} \left[ - \int_{-b}^b p(r) \cdot \ln \left| \frac{r}{b} \right| ds + \frac{N}{L} \ln \left| \frac{L}{b} \right| \right]$$

This displacement is relative to one side only. If both sides are desired, then

$$\delta_z = \frac{4(1 - \nu^2)}{\pi E} \frac{N}{L} \left[ - \int_{-b}^b p(r) \frac{Lb}{N} \cdot \ln \left| \frac{r}{b} \right| d \frac{s}{b} + \ln \left| \frac{L}{b} \right| \right]$$

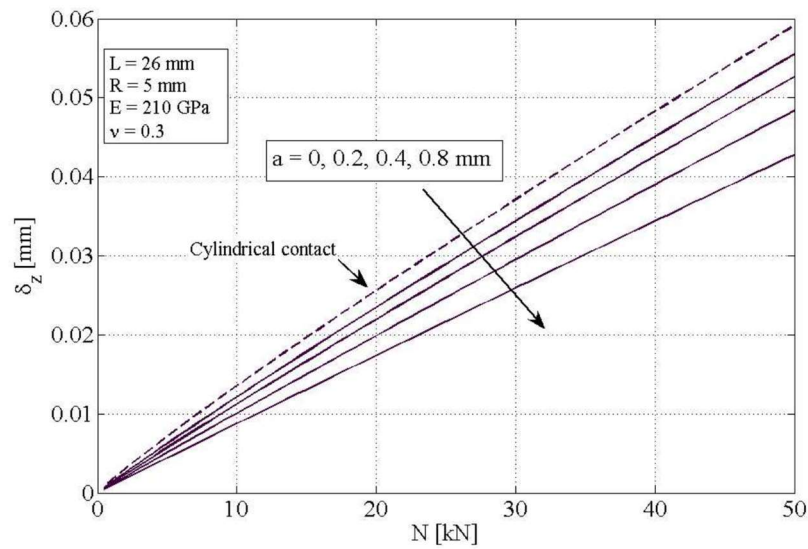


Figure A6.1. Normal contact displacement versus normal load. Different curves for different geometries (the half width of the flat part varies from 0, Hertzian contact, to 0.8 mm). The length of the contact  $L$  and the edge radius,  $R$ , are kept constant.

The normal stiffness can be numerically calculated as

$$\frac{1}{k_n} = \frac{d\delta_z}{dN}$$

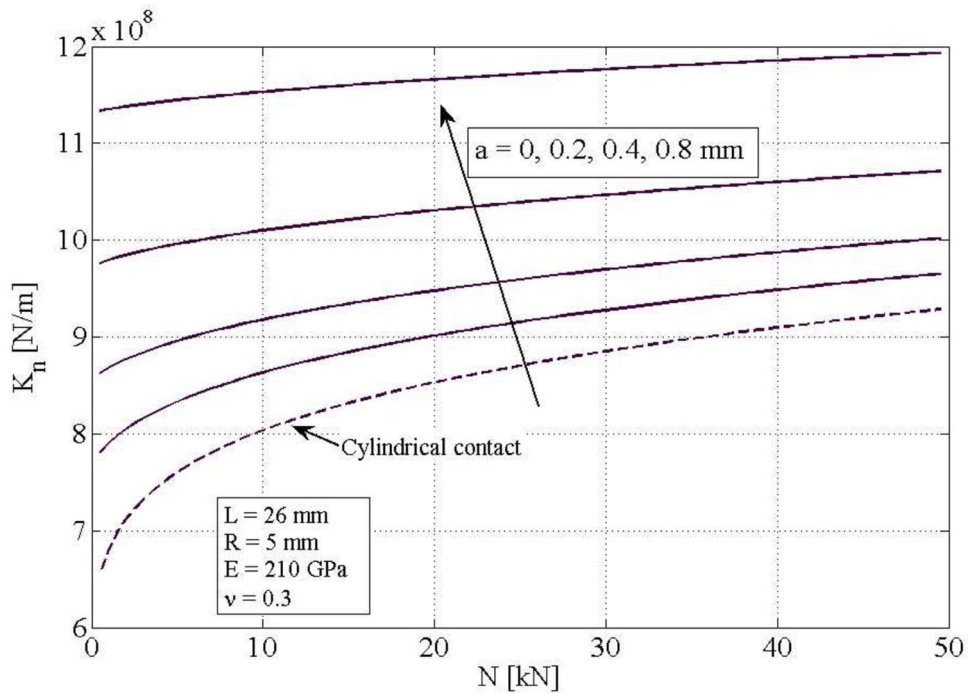


Figure A6.1. Normal contact displacement versus normal load. Different curves for different geometries ( the half width of the flat part varies from 0, Hertzian contact, to 0.8 mm). The length of the contact  $L$  and the edge radius,  $R$ , are kept constant.

The approach adopted is the same proposed by different authors ([59]-[60]-[61]) to evaluate the deformation of cylinders in contact. Here the method is extended to a different geometry, flat punch with rounded edges.

# Appendix F

## Measurement Error Estimates and Propagation

The procedure here proposed is used to calculate the measurement error propagation to the identified frequency and damping. According to the method in use (Chapter 4), the natural frequencies and the damping loss factors are functions of the envelope  $V(t)$  and of the instantaneous phase  $\varphi(t)$  of the analytic signal. Measured values of the phase and envelope can be expressed as function of their actual (or “true”) values as in the following two equations (m subscript is for “measured,” t subscript is for “true”):

$$\varphi_m(t) = \varphi_t(t) + \delta\varphi(t)$$

$$V_m(t) = V_t(t) + \delta V(t)$$

Similarly the error on the sampling time is:

$$\Delta t_m = \Delta t_t (1 \pm \varepsilon_f)$$

Where  $\varepsilon_f$  is the sampling frequency error. The vibrating frequency is calculated using finite differences instead of the differential form:

$$\omega_m(t) \cong \frac{\varphi_m(t + \Delta t) - \varphi_m(t)}{\Delta t_m}$$

Similarly the hysteretic damping is approximated as:

$$\eta_m \cong \frac{2}{\omega_m \Delta t_m} \ln \frac{V_m(t)}{V_m(t + \Delta t)}$$

$$\omega_m(t) \cong \omega_t (1 \pm \varepsilon_f) + \frac{\delta\varphi(t + \Delta t) - \delta\varphi(t)}{\Delta t_m}$$

$$\eta_m \cong \eta_t \left( 1 + \frac{\delta\varphi(t) - \delta\varphi(t + \Delta t)}{\omega_t \Delta t_t} \right) + \frac{2}{\Delta t_m \omega_m} \left( \frac{\delta V(t)}{V_t(t)} - \frac{\delta V(t + \Delta t)}{V_t(t + \Delta t)} \right)$$

Where  $t_m$  is the duration (in time) of the recorded signal used for the identification,  $n_{\text{periods}}$  is the number of periods, hence:

$$\omega_m \cdot \Delta t_m = 2\pi n_{\text{periods}}$$

$$\omega_m = \omega_t \left( 1 \pm \varepsilon_f + \frac{\delta\varphi(t + \Delta t) - \delta\varphi(t)}{2\pi n_{\text{periods}}} \right)$$

$$\eta_m = \eta_t \left( 1 + \frac{\delta\varphi(t) - \delta\varphi(t + \Delta t)}{2\pi n_{\text{periods}}} \right) + \frac{1}{\pi n_{\text{periods}}} \left( \frac{\delta V(t)}{V(t)} - \frac{\delta V(t + \Delta t)}{V(t + \Delta t)} \right)$$

The next step is to express  $V$  as a function of measurement errors. If the measured signal has a bias, this would be filtered and therefore it has no effect on the identification. Also, any eventual calibration error  $\varepsilon_0$  has no effect, in fact:

$$\text{tg}\varphi_m = \frac{\tilde{v}_m}{v_m} = \frac{\tilde{v}_t (1 + \varepsilon_0)}{v_t (1 + \varepsilon_0)} = \text{tg}\varphi_t$$

$$\eta_m = \frac{2}{\omega_0 \Delta t} \ln \frac{V_m(t)}{V_m(t + \Delta t)} = \frac{2}{\omega_0 \Delta t} \ln \frac{V_t(t)(1 + \varepsilon_0)}{V_t(t + \Delta t)(1 + \varepsilon_0)} = \eta_t$$

Therefore the only source of error in the identification process is the measurement noise. The Hilbert transform of a signal corrupted with noise is:

$$v_m = v_t(t) + r(t) \xrightarrow{H} \tilde{v}_m = \tilde{v}_t(t) + \tilde{r}(t)$$

Where  $r(t)$  is random Gaussian noise and  $r(t) = H(r(t))$ . According to the properties of the Hilbert transform of a random Gaussian signal,  $r(t)$  is a signal with the same statistical properties of  $r(t)$  [62]. In Fig. A7.1 the analytic signals of the real and measured signals are reported in a polar coordinate for a given time instant.  $R$  is the module of the difference between  $V_m$  and  $V_t$  due to noise.

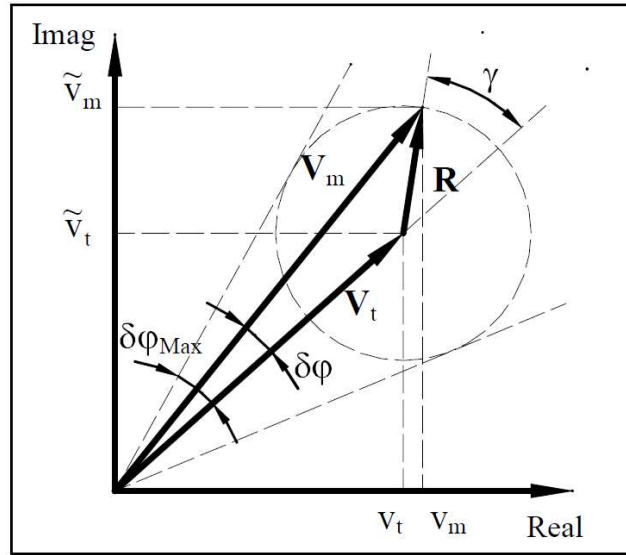


Figure A7.1. True and measured analytic signal in polar representation.

Following the graphic construction of Fig. A7.1, and  $V$  can be estimated as:

$$|\delta\varphi_{\text{Noise}}| \leq \frac{r_{\text{RMS}}}{V_m}$$

$$|\delta V_{\text{Noise}}| \leq r_{\text{RMS}}$$

The last two relations can be substituted in Eqs. (6) and (7), allowing for  $\delta(t)$  to be uncorrelated with  $\delta\varphi(t+\Delta t)$ :

$$|\delta\varphi(t) - \delta\varphi(t + \Delta t)| \leq \sqrt{2} \cdot \delta\varphi_{\text{Noise}} = \sqrt{2} \frac{r_{\text{RMS}}}{V_m}$$

$$\left| \frac{\delta V(t)}{V(t)} - \frac{\delta V(t + \Delta t)}{V(t + \Delta t)} \right| \leq \sqrt{2} \frac{\delta V_{\text{Noise}}}{V_m} = \sqrt{2} \frac{r_{\text{RMS}}}{V_m}$$

Finally the expression for and can be written with the effect of noise:

$$\omega_m = \omega_l \left( 1 \pm \varepsilon_f \pm \frac{1}{\sqrt{2}\pi n_{\text{periods}}} \frac{r_{\text{RMS}}}{V_m} \right)$$

$$\eta_m = \eta_l \left( 1 \pm \frac{1}{\sqrt{2}\pi n_{\text{periods}}} \frac{r_{\text{RMS}}}{V_m} \right) \pm \frac{\sqrt{2}}{\pi n_{\text{periods}}} \frac{r_{\text{RMS}}}{V_m}$$

Where the term  $\varepsilon_f$  is negligible because it is two orders of magnitude smaller than the term due to the noise to signal ratio.

## References

- [1] Allara, M., Filippi, S., Gola, M.M., 2006, An Experimental Method For The Measurement Of Blade-Root Damping, Proceedings of ASME Turbo Expo 2006, GT2006-90774
- [2] Griffin, J.H., 1980, Friction Damping of Resonant Stresses in Gas Turbine Engine Air foils, Journal of Engineering for Power, 102-2, pp.329-333
- [3] Yang, B.D., Chu, M.L., Menq, C.H., 1998, Stick-Slip-Separation Analysis And Non-Linear Stiffness And Damping Characterization Of Friction Contacts Having Variable Normal Load, Journal of Sound and Vibration, 210(4), pp. 461-481
- [4] Schwingshackl C.W., Petrov E.P., Ewins D.J., 2012 Measured and estimated friction interface parameters in a nonlinear dynamic analysis, Mechanical Systems and Signal Processing, 28, pp. 574–584
- [5] Stanbridge A.B., Ewins D.J., Sanliturk K.Y., Ferreira J.V., 2001, Experimental Investigation of Dry Friction Damping and Cubic Stiffness Non-Linearity, Proceedings of the ASME Design Engineering Technical Conference, Pittsburgh, PA, USA
- [6] Menq, C.H., Yang, B.D., 1998, Non-Linear Spring Resistance and Friction Damping of Frictional Constraint having Two-Dimensional Motion, Journal of Sound and Vibration, 217, pp. 127-143
- [7] Yang, B.D., Menq, C.H., 1998, Characterization of 3D Contact Kinematics and Prediction of Resonant Response of Structures having 3D Frictional Constraint, Journal of Sound and Vibration, 217-5, pp.909-925\

- [8] Mindlin, R.D., Mason, W.P., Osmer, T.F., Deresiewicz, H., 1952, Effects of an Oscillating Tangential Force on the Contact Surfaces of Elastic Spheres, Proceedings of the First US National Congress of Applied Mechanics, pp. 203-208
- [9] Lavella, M.; Botto, D.; Gola, M.M., 2011, Test Rig for Wear and Contact Parameters Extraction for Flat-on-Flat Contact Surfaces, In Proceedings of the ASME/STLE 2011 Joint Tribology Conference, Los Angeles, CA,USA,pp. 24–26
- [10] Koh K.H., Griffin J.H., Filippi S., Akay A., 2005, Characterization of turbine blade friction dampers, ASME Journal of Engineering for Gas Turbines and Power, 12
- [11] Koh K.H., Griffin J.H., 2006, Dynamic Behaviour of Spherical Friction Dampers and its Implication to Damper Contact Stiffness, Proceedings of the ASME Turbo Expo GT2006, Barcelona, Spain
- [12] Shtayerman I.Y., 1949, Contact Problem of the Theory of Elasticity, Gostekhteoretizdat, Moscow and Leningrad
- [13] Allara, M., 2009, A model for the Characterization of Friction Contacts in Turbines Blades, Journal of Sound and Vibration, 320, pp. 527-544
- [14] Ciavarella, M., Hills, D.A., Monno, G., 1998, The Influence of Rounded Edges on Indentation by a Flat Punch, Proceedings of the Institution of Mechanical Engineers, 212, pp. 319-328
- [15] Cardona A., Lerusse A., Geradin M., 1998, Fast Fourier Nonlinear Vibration Analysis, Computational Mechanics, 22-2, pp. 128-142
- [16] Petrov, E.P.; Ewins, D.J., 2003, Analytical Formulation of Friction Interface Elements for Analysis of Nonlinear Multi-Harmonic Vibrations of Bladed Disks, ASME Journal of Turbomachinery, 125, pp. 364-371
- [17] Siewert, C., Panning, L., Wallaschek, J., Richter, C., 2010, Multiharmonic Forced Response Analysis of a Turbine Blading Coupled by Nonlinear Contact Forces, ASME Journal of Engineering for Gas Turbines and Power, 132, 082501
- [18] Zucca, S., Fironne, C.M., 2012, Nonlinear Dynamics of Mechanical Systems with Friction Contacts: Harmonic Balance Method and Multiple Solutions, Proceedings of ISMA 2012, pp. 1017-1030
- [19] Zucca S., Fironne C.M., Gola M.M., 2012, Numerical Assessment of friction Damping at Turbine Blade Root Joints by Simultaneous Calculation of the Static and Dynamic Contact Loads, Nonlinear Dynamics, 67, pp. 1943-1955
- [20] Zucca S., Fironne C.M., Gola M.M., 2011, The effect of Under platform Dampers on the Forced Response of Bladed Disks by a Coupled Static/Dynamic Harmonic Balance Method, International Journal of Non-Linear Mechanics, 46-2, pp. 363-375



- [21] Sanliturk, K.Y., Ewins, D.J., 1996, Modelling Two-dimensional Friction Contact and its Application using Harmonic Balance Method, *Journal of Sound and Vibration*, 193-2, pp. 511-523
- [22] Gastaldi, C., Berruti, T.M., 2018, Competitive Time Marching Solution Methods for Systems with Friction-Induced Nonlinearities, *Applied Sciences*, 8(2), 291
- [23] Mindlin, R.D., 1949, Compliance of Elastic Bodies in Contact, *Journal of Applied Mechanics*, 16, pp. 259-268
- [24] Johnson K.L., 1955, Surface Interaction Between Elastically Loaded Bodies Under Tangential Forces, *Proceedings of Royal Society of London, Ser.A*, A230, pp. 531-549
- [25] Goodman L.E., Brown C.B., 1962, Energy Dissipation in Contact Friction: Constant Normal and Cyclic Tangential Loading, *ASME Journal of Applied Mechanics*, 29, pp. 17-22
- [26] Filippi S., Akay, A., Gola, M.M., 2004, Measurement of Tangential Contact Hysteresis During Micro slip, *ASME Journal of Tribology*, 126, pp. 482-489
- [27] Filippi S., Rodrigues E.B., Gola M.M., 2006, Experimental Characterization of Contact Hysteresis at High Temperatures, *Proceedings of the ASME Turbo Expo GT2006*, Barcellona, Spain
- [28] Goodman L.E., Klumpp J.H., 1956, Analysis of Slip Damping with Reference to Turbine-Blade Vibration, *ASME Journal of Applied Mechanics*, 23, pp. 421-429
- [29] Coro A., Marquina F.J., Alonso R., Gutierrez A., Ewins D.J., Girini G., 2008, Friction Damping Modeling in High Stress Contact Areas using Micro slip Friction Model, *Proceedings of ASME Turbo Expo 2008*, June 9-13, Berlin
- [30] Bokaian, A., 1990, Natural Frequencies of Beams under Tensile Axial Loads *Journal of Sounds and Vibration*, 142, pp. 481-498
- [31] Simmons H.R., Iyengar V., 2011, Effect of Non Uniform Blade Root Friction and Sticking on Disk Stresses, *Proceedings of ASME Turbo Expo 2011*, June 6–10, Vancouver, Canada
- [32] Umer M., Botto D., 2019, Measurement of contact parameters on under-platform dampers coupled with blade dynamics, *International Journal of Mechanical Sciences*, 159, pp. 450-458
- [33] Feldman, M., 1994, Non-Linear System Vibration Analysis Using Hilbert Transform -I. Free Vibration Analysis Method FREEVIB“, *Mechanical System and Signal Processing*, 8, pp. 119-127
- [34] Feldman, M., 2011, *Hilbert Transform Applications in Mechanical Vibration*, John Wiley & Sons

- [35] Craig,R.R., Bampton,M.C.C.,1968, Coupling of Substructures for Dynamic Analyses, AIAA Journal, 12, pp. 1313-1319
- [36] Theory Reference for the Mechanical APDL and Mechanical Applications, Ansys® Mechanical Help
- [37] Agneni, A., Balis-Crema, L.,1989, Damping Measurements from Truncated Signal via Hilbert Transform, Mechanical System and Signal Processing,3,pp. 1-13
- [38] Asai K., Sakurai S., Kudo T., Ozawa N., Ikeda T., 2009, Evaluation of Friction Damping in Dovetail Root Joints based on Dissipation Energy on Contact Surfaces, Proceedings of ASME Turbo Expo 2009, June 8–12, Orlando, Florida
- [39] Inaudi, J.A.,Makris,N.,1996, Time-Domain Analysis Of linear Hysteretic Damping, Earthquake Engineering And Structural Dynamics,25,pp.529-545
- [40] Firrone C.M., Bertino I., 2015, Experimental Investigation on the Damping Effectiveness of Blade Root Joints, Experimental Mechanics, 55, pp. 981-988
- [41] Newmark,N.,1959, A Method of Computation for Structural Dynamics, Journal of the Engineering Mechanics Division,85,pp. 67-94
- [42] Menq,C.,Griffin,J.H.,1985, A Comparison of Transient and Steady State Finite Element Analyses of the Forced Response of a Frictionally Damped Beam, ASME Journal of Vibrations, Acoustics, Stress and Reliability in Design,107,pp. 19-25
- [43] Zucca,S.,Firrone,C.M.,2011, Modelling Friction Contacts in Structural Dynamics and its Application to Turbine Bladed Disks, Numerical Analysis - Theory and Application, pp.301-334
- [44] Richter,P.H.,1995, Estimating Errors in Least-Squares Fitting, NASA TDA Progress Report,42-122, pp. 107-124
- [45] Johnson,K.L.,1985, Contact Mechanics, Cambridge University Press, Cambridge
- [46] Lavella, M.; Botto, D.; Gola, M.M. Test Rig for Wear and Contact Parameters Extraction for Flat-on-Flat Contact Surfaces. In Proceedings of the American Society of Mechanical Engineers, Tribology Division, TRIB, Copenhagen, Denmark, 9 February 2011; American Society of Mechanical Engineers Digital Collection, pp. 307–309.